SEARCH FOR RADIATIVE DECAYS OF UPSILON(1S) INTO ETA AND ETA-PRIME

By

VIJAY SINGH POTLIA

A DISSERTATION PRESENTED TO THE GRADUATE SCHOOL
OF THE UNIVERSITY OF FLORIDA IN PARTIAL FULFILLMENT
OF THE REQUIREMENTS FOR THE DEGREE OF
DOCTOR OF PHILOSOPHY

UNIVERSITY OF FLORIDA

2006

To my parents

ACKNOWLEDGMENTS

I would like to thank all those people who helped me at different stages during the course of this dissertation work. I would, first and foremost like to thank my advisor Dr. Yelton for his invaluable guidance and expertise in the conducted research, and for giving me the freedom to develop and put to test my own ideas in many different aspects. Besides being an excellent mentor, he has always been very patient and is a very understanding person which helped immensely during the "ups and downs" phases of the analysis.

I also thank my Physics teachers Dr. Thorn and Dr. Woodard, and Committee members Dr. Avery and Dr. Tanner at the University of Florida, for inculcating the lessons of physics and for being a source of inspiration. I would like to extend my thanks to the entire CLEO collaboration for setting up the playground for this research. I particularly would like to thank my internal analysis committee members David Besson, Helmut Vogel, Jianchun Wang and especially Rich Galik for all their help and suggestions to improve this work. Many thanks to Hanna Mahlke-Krueger and Basit Athar for their help.

I also thank my fellow colleages Luis Breva, Valentin Necula, G. Suhas, and many others for fruitful physics discussions. I also thank the computer staff at the University of Florida, especially David Hansen for his computing help.

Rukhsana Patel, Sanjay Siwach, Sunil Bhardwaj, and Lakhan Gusain have been extremely supportive friends during this long journey. I can not thank them enough.

I owe many thanks to my parents Ranbir and Premlata, and my cousin Fateh. Last but not the least, the most important person without whose support and endurance this dissertation would not have been completed is my wife Nisha. I thank her for

being by my side in all odds and for her love and patience which served as my guiding torch.

TABLE OF CONTENTS

LIST OF TABLES

LIST OF FIGURES

Abstract of Dissertation Presented to the Graduate School
of the University of Florida in Partial Fulfillment of the
Requirements for the Degree of Doctor of Philosophy

SEARCH FOR RADIATIVE DECAYS OF UPSILON(1S)
INTO ETA AND ETA-PRIME

By

Vijay Singh Potlia

May 2006

Chair: John M. Yelton
Major Department: Physics

We conducted a new search for the radiative decay of $\Upsilon(1S)$ to the pseudoscalar mesons η and η' in $(21.2 \pm 0.2) \times 10^6$ $\Upsilon(1S)$ decays collected with the CLEO III detector operation at the Cornell Electron Strorage Ring (CESR). The η meson was reconstructed in the three modes $\eta \to \gamma\gamma$, $\eta \to \pi^+\pi^-\pi^0$ or $\eta \to \pi^0\pi^0\pi^0$. The η' meson was reconstructed in the mode $\eta' \to \pi^+\pi^-\eta$ with η decaying through any of the above three modes; and also $\eta' \to \gamma\rho^0$, where $\rho^0 \to \pi^+\pi^-$. The first six of these decay chains were searched for in the previous CLEO II analysis on this subject, which used a data sample 14.6 times smaller.

Five of the seven submodes were virtually background free. We found no signal events in four of them. The only exception was $\Upsilon(1S) \to \gamma\eta'; \eta \to \pi^+\pi^-\pi^0$ where we observed two good signal candidates. The other two submodes ($\eta \to \gamma\gamma$ and $\eta' \to \gamma\rho$) are background limited, and showed no excess of events in the signal region. We combined the results from different channels and obtained 90% confidence level (C.L.) upper limits $\mathcal{B}(\Upsilon(1S) \to \gamma\eta) < 9.3 \times 10^{-7}$ and $\mathcal{B}(\Upsilon(1S) \to \gamma\eta') < 1.77 \times 10^{-6}$. Our limits challenge theoretical models.

CHAPTER 1
THEORY

1.1 Particle Physics and the Standard Model

Humankind has always been intrigued by questions like "What is matter made of?" and "How do the constituents of matter interact with each other?" In their quest for fundamental building blocks of matter, physicists found even more compositeness. The existence of more than 100 elements showing periodically recurring properties was a clear indication that atoms (once thought indestructible and fundamental building blocks) have an internal structure. At the start of the 20th century, the internal structure of the atom was revealed through a series of experiments. The core of an atom (the nucleus) was found to be made of protons and neutrons (collectively called nucleons), surrounded by an electron cloud. This picture of the atom was right; however, the observation of radioactive β-decay and the stability of the nucleus prompted physicists to take the reductionist approach farther and a new branch of physics was born called as particle physics.

Modern particle physics research represents the most ambitious and most organized effort of humankind to answer the questions of fundamental building blocks and their interactions. Over the last half century, our understanding of particle physics advanced tremendously and we now have a theoretical structure (the Standard Model) firmly grounded in experiment that splendidly describes the fundamental constituents of matter and their interactions.

1.1.1 The Standard Model: Inputs and Interactions

The Standard Model (SM) of elementary particle physics comprises the unified theory of all the known forces except gravity. These forces are the electro-magnetic force (well known to us in everyday life), the weak force, and the strong force. In the

Standard Model, the fundamental constituents of the matter are quarks and leptons. These constituents are spin-$\frac{1}{2}$ particles (fermions) obeying Fermi-Dirac statistics.

The quarks and leptons come in three generations:

- up and down quarks (u, d), and electronic neutrino and electron (ν_e, e)
- charm and strange quarks (c, s), and muonic neutrino and muon (ν_μ, μ)
- top and bottom quarks (t, b), and tauonic neutrino and tauon (ν_τ, τ)

Each generation has a doublet of particles arranged according to the electric charge. The leptons fall into two classes, the neutral neutrinos ν_e, ν_μ, ν_τ, and negatively charged e^-, μ^-, and τ^-. The quarks u, c, and t have electric charge +2e/3 and the d, s, and b quarks have electric charge −e/3. Each quark is said to constitute a separate flavor (six quark flavors exist in nature). The generations are arranged in the mass hierarchy and the masses fit no evident pattern. The neutrinos are considered as massless. The Standard Model does not attempt to explain the variety and the number of quarks and leptons or to compute any of their properties; the fundamental fermions are taken as truly elementary at the SM level. Each of the fundamental fermions has an anti-fermion of equal mass and spin, and opposite charge. Other than the electric charge, the basic fermions have two more charges — "color charge" coupling to strong force, an attribute of quarks only (but not leptons), and "weak charge" or "weak isospin" coupling to weak force, carried by all fundamental fermions. The properties of these fermions (Table 1–1) recur in each generation.

In the paradigm of Standard Model, the three different types of interactions existing among the elementary particles arise as a natural and automatic consequence of enforcing local gauge symmetry. Each force is mediated by a force carrier, a gauge boson which couples to the charge on the particle. The bosons are spin-1 particles. The guage bosons of SM are shown in Table 1–2.

Table 1–1. Basic fermions and some of their properties

Quarks				Leptons			
Flavor	Mass (MeV/c^2)	Electric charge	Weak charge	Flavor	Mass (MeV/c^2)	Electric charge	Weak charge
u	2-8	+2e/3	+1/2	ν_e	< 0.000015	0	+1/2
d	5-15	-e/3	-1/2	e	0.511	-e	-1/2
c	1000-1600	+2e/3	+1/2	ν_μ	< 0.19	0	+1/2
s	100-300	-e/3	-1/2	μ	105.7	-e	-1/2
t	≈ 175000	+2e/3	+1/2	ν_τ	< 18.2	0	+1/2
b	4100-4500	-e/3	-1/2	τ	1777.0	-e	-1/2

The familiar electro-magnetic force (also called as Quantum Electrodynamics, or QED) is mediated by the exchange of a photon. Only particles with electric charge can interact electro-magnetically. The strong force is mediated by gluons and couples to particles that have color charge. This force is responsible for holding quarks together inside the hadrons (neutron and proton are two example of hadrons). Leptons have no color and thus do not experience strong force. This is one of the primary differences between leptons and quarks. The weak force is mediated by the $W^\pm$ and Z^0 bosons. Particles with weak charge, or weak isospin, can interact via the weak force. The mediators of weak force are different from the photons and gluons in the sense that these mediating particles ($W^\pm$ and Z^0) are massive. The weak force thus is a short range force as opposed to electro-magnetic and strong forces which are long-range in nature due to masslessness of photon and gluons.

Table 1–2. Gauge bosons and some of their properties

Particle	Symbol	Force Mediated	Charge	Mass (GeV/c^2)	J^P
Photon	γ	Electromagnetic	0	0	1^-
Gluon	g	Strong	8 colors	0	1^-
Z^0	Z^0	Weak	0	91.187	1
$W^\pm$	$W^\pm$	Weak	$\pm$e	80.40	1

1.1.2 Quantum Chromodynamics

Strong interactions in the Standard Model are described by the theory of Quantum Chromodynamics (QCD). The quarks come in three primary colors:[1] r (red), g (green), and b (blue) and the anti-quarks have complementary colors (or anti-colors) $\bar{r}$ (cyan), $\bar{g}$ (magenta), and $\bar{b}$ (yellow). The quarks interact strongly by exchanging color which is mediated by gluon exchange (Figure 1–1). Gluon exchange is possible only if the gluons themselves are colored (carry color charge), and in fact, the gluons carry the color and anti-color simultaneously. The strength of strong interaction is flavor independent.

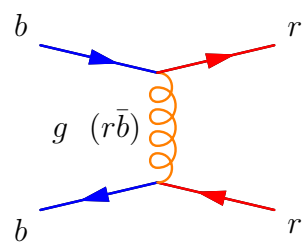

Figure 1–1. Simple gluon-exchange diagram

Since there are three possible colors and three possible anti-colors for gluons, one might guess that the gluons come in as many as nine different color combinations. However, one linear combination of color anti-color states has no net color and therefore can not mediate among color charges. Thus only eight linearly independent color combinations are possible. The way in which these eight states are constructed from colors and anti-colors is a matter of convention. One possible choice is shown in Equation 1–1 for the octet, and the color singlet is represented in Equation 1–2,

$$r\bar{g},\quad r\bar{b},\quad g\bar{b},\quad g\bar{r},\quad b\bar{r},\quad b\bar{g},\quad \sqrt{1/2}(r\bar{r}-g\bar{g}),\quad \sqrt{1/6}(r\bar{r}+g\bar{g}-2b\bar{b}) \tag{1–1}$$

$$\sqrt{1/3}(r\bar{r}+g\bar{g}+b\bar{b}) \tag{1–2}$$

[1] The "color" in QCD is a degree of freedom describing the underlying physics, and should not be misinterpreted with ordinary colors we see in life.

This situation is analogous to the perhaps more familiar example of two spin 1/2 particles. Each particle can have its spin up ($\uparrow$) or down ($\downarrow$) along the z axis corresponding to four possible combinations represented by each giving a total spin $S = 0$ or 1 represented by $|S\ S_z>$. The S = 1 states form a triplet,

$$\begin{aligned} |1\ +1> &= |\uparrow\uparrow> \\ |1\ 0> &= \frac{1}{\sqrt{2}}(|\uparrow\downarrow> + |\downarrow\uparrow>) \\ |1\ -1> &= |\downarrow\downarrow> \end{aligned} \tag{1–3}$$

and there is a singlet state with S = 0,

$$|0\ 0> = \frac{1}{\sqrt{2}}(|\uparrow\downarrow> - |\downarrow\uparrow>). \tag{1–4}$$

The proliferation of gluons in QCD contrasts with QED where there is only a single photon. Another striking difference between QED and QCD is that the force carriers in QED, the photons, do not carry any charge. The photons therefore, do not have self-interactions. On the other hand, the gluons in QCD have color charge and thus they undergo self-interactions. In field-theoretic language, theories in which field quanta may interact directly are called "non-Abelian." The gluon self-interaction leads to two very important characteristics of QCD: "color confinement" and "asymptotic freedom." Color confinement means that the observed states in nature have no net color charge: i.e., the observed states are color singlets. An implication of color confinement is that free quarks and free gluons can not be observed in nature. Bound states of two or more gluons having overall zero color charge can be found in principle. Such bound states are referred to as "glueballs." Many experimental searches for such states have been made, without conclusive results, for example [1]. Asymptotic freedom means that the interaction gets weaker at shorter inter-quark distances and the quarks are relatively free in that limit.

The phenomenon of color confinement constrains the way quarks combine to form observed particle states. The only combinations allowed (and observed for that matter) are $q\bar{q}$ forming mesons, and qqq forming baryons. Group-theoretically, it is possible to decompose $3 \times \bar{3}$ ($q\bar{q}$) to obtain an octet and a singlet. The color singlet for $q\bar{q}$ is simply the state shown in Equation 1–2. The color singlet for qqq can be obtained from decomposition $3 \otimes 3 \otimes 3 = 10 \oplus 8 \oplus 8 \oplus 1$ and is shown in Equation 1–5,

$$|qqq>_{color\ singlet} = \frac{1}{\sqrt{6}}(rgb - grb + brg - bgr + gbr - rbg). \tag{1–5}$$

The existence of particles with fractional charges, as for example made from bound state qq, is ruled out as it is not possible to obtain a color singlet qq configuration. Group theory quickly tells us that $3 \otimes 3$ decomposition is $6 \oplus 3$ (a sextet and a triplet, but no singlet).

1.1.3 Symmetries

Symmetries are of great importance in physics. A symmetry arises in nature whenever some change in the variables of the system leaves the essential physics unchanged. The symmetry thus leads to conservation laws — universal laws of nature valid for all interactions, for example, the conservation of linear momentum and angular momentum arise from translational invariance and rotational invariance, respectively. Enforcing local gauge symmetry gives rise to interactions in field theory. Isospin symmetry is responsible for attractive force between nucleons on an equal footing. In particle physics, the discrete symmetry operations parity and charge conjugation play a special role in particle production and decay. Certain reactions are forbidden due to the constraints imposed by these symmetries — the symmetries thus become dynamics. In the next few sections we review some of these symmetry operations, the details of which can be found in Griffiths [2], Perkins [3], and Halzen and Martin [4].

1.1.3.1 Isospin

The nuclear force between nucleons is the same irrespective of the charge on the nucleon. The proton and neutron are thus treated as two states of a nucleon which form an "isospin" doublet (I = 1/2),

$$\psi = \begin{pmatrix} p \\ n \end{pmatrix} \tag{1–6}$$

with I_3, the third component of I, being $+1/2$ for proton and $-1/2$ for neutron. The origin of isospin lies in the near equality of the u and d quark masses, so, the idea of isospin can be taken to a more fundamental level where u and d quarks form a doublet which can be transformed into each other in the isospin space. The I_3 for an u quark is $+1/2$ and that for a d quark is $-1/2$ and based upon this assignment, I_3 speaks for the quark flavor. The I_3 for anti-quarks is the negative of that of quarks. The treatment of isospin goes very much like quantum mechanical angular momentum.

Since strong and electro-magnetic interactions conserve the quark flavor, the third component of isospin is a good quantum number for these interactions. However, total isospin I is not conserved under electro-magnetic interactions as the isotropy of isospin is broken due to different electric charge on the u and d quarks. Only strong interactions conserve both I and I_3.

1.1.3.2 Parity

The parity operator, $\hat{P}$, reverses the sign of an object's spatial coordinates. Consider a particle $|a>$ with a wave function $\Psi_a(\vec{x}, t)$. By the definition of the parity operator,

$$\hat{P}\Psi(\vec{x}, t) = P_a \Psi_a(-\vec{x}, t) \tag{1–7}$$

where P_a is a constant phase factor. If we consider an eigenfunction of momentum

$$\Psi_{\vec{p}}(\vec{x}, t) = e^{i(\vec{p}\cdot\vec{x} - Et)} \tag{1–8}$$

then

$$\hat{P}\Psi_{\vec{p}}(\vec{x},t) = P_a\Psi_{\vec{p}}(-\vec{x},t) = P_a\Psi_{-\vec{p}}(\vec{x},t), \tag{1–9}$$

so that any particle at rest, with $\vec{p} = 0$, remains unchanged up to a multiplicative number, P_a, under the parity operator. States with this property are called eigenstates with eigenvalue P_a. The quantity P_a is also called the intrinsic parity of particle a, or more usually just the parity of particle a. Since two successive parity transformations leave the system unchanged, $P_a^2 = 1$, implying that the possible values for the parity eigenvalue are $P_a = \pm 1$.

In addition to a particle at rest, a particle with definite orbital angular momentum is also an eigenstate of parity. The wave function for such a particle in spherical coordinates is

$$\Psi_{nlm}(\vec{x},t) = R_{nl}(r)Y_l^m(\theta,\phi), \tag{1–10}$$

where (r,θ,ϕ) are spherical polar coordinates, $R_{nl}(r)$ is a function of the radial variable r only, and the $Y_l^m(\theta,\phi)$ is a spherical harmonic. The spherical harmonics are well known functions which have the following property,

$$Y_l^m(\theta,\phi) = (-1)^l Y_l^m(\pi-\theta,\pi+\phi). \tag{1–11}$$

Hence

$$\hat{P}\Psi_{nlm}(\vec{x},t) = P_a\Psi_{nlm}(-\vec{x},t) = P_a(-1)^l\Psi_{nlm}(\vec{x},t) \tag{1–12}$$

proving that a particle with a definite orbital angular momentum l is indeed an eigenstate of the parity operator with eigenvalue $P_a(-1)^l$.

The parity of the fundamental fermions cannot be measured or derived. All that Nature requires is that the parity of a fermion be opposite to that of an anti-fermion. As a matter of convention fermions are assigned $P = +1$ and anti-fermions are assigned $P = -1$. In contrast, the parities of the photon and gluon can be derived by applying $\hat{P}$ to the field equations resulting in $P_\gamma = -1$ and $P_g = -1$.

The parity of Υ(1S), a spin 1 $b\bar{b}$ bound state (described in Section 1.2) with L = 0 is $P = P_b P_{\bar{b}}(-1)^L = -1$.

Parity is a good quantum number because it is a symmetry of the strong and electro-magnetic force. This means that in any reaction involving these forces, parity must be conserved.

1.1.3.3 Charge conjugation

The operation that replaces all particles by their anti-particles is known as charge conjugation. In quantum mechanics the charge conjugation operator is represented by $\hat{C}$. For any particle $|a>$ we can write

$$\hat{C}|a>= c_a|\bar{a}> \tag{1–13}$$

where c_a is a phase factor. If we let the $\hat{C}$ operator act twice to recover the original state $|a>$,

$$|a>= \hat{C}^2|a>= \hat{C}(c_a|\bar{a}>) = c_a\hat{C}|\bar{a}>= c_a c_{\bar{a}}|a> \tag{1–14}$$

which shows that $c_a c_{\bar{a}} = 1$. If (and only if) a is its own anti-particle, it is an eigenstate of $\hat{C}$. The possible eigenvalues are limited to $C = c_a = c_{\bar{a}} = \pm 1$.

All systems composed of the same fermion and an anti-fermion pair are eigenstates of $\hat{C}$ with eigenvalue $C = (-1)^{(L+S)}$. This factor can be understood because of the need to exchange both particles' position and spin to recover the original state after the charge conjugation operator is applied. Exchanging the particles' position gives a factor of $(-1)^L$ as shown in the previous section. Exchanging the particles' spin gives a factor of $(-1)^{S+1}$ as can be verified by inspecting Equations 1–3 and 1–4, and a factor of (-1) which arises in quantum field theory whenever fermions and anti-fermions are interchanged. With this result we can calculate the charge conjugation eigenvalue for the Υ(1S) and obtain $C = -1$ since $L + S = 1$.

The photon is an eigenstate of $\hat{C}$ since it is its own anti-particle. The C eigenvalue for the photon can be derived by inserting $\hat{C}$ into the field equations and is $C_\gamma = -1$.

1.1.3.4 G-Parity

We just learned from the charge conjugation operation that only neutral particles can be eigenstates of charge conjugation operator. A useful conservation law for the strong interactions can be set up by combining the charge conjugation operation with a 180° rotation about a chosen axis in the isospin space. This combined operation of rotation in the isospin space, followed by charge conjugation, is called as G-parity

$$G = \hat{C}\exp(-i\tau_2\pi) \tag{1–15}$$

As noted earlier, the isospin has the same algebraic properties that of quantum mechanical angular momentum operator, the rotation of an isospin state $|\mathrm{I}, \mathrm{I}_3>$ in isospin space about y-axis by an angle π can be carried out as:

$$R_2(\pi)|\mathrm{I}, \mathrm{I}_3>= \exp(-i\tau_2\pi)|\mathrm{I}, \mathrm{I}_3>= (-1)^{\mathrm{I}-\mathrm{I}_3}|\mathrm{I}, -\mathrm{I}_3> \tag{1–16}$$

Thus, for a rotation π about the 2 axis (y axis) in isospin space we have

$$\begin{aligned} R_2(\pi)|\pi^+> &= |\pi^->\\ R_2(\pi)|\pi^->&= |\pi^+>\\ R_2(\pi)|\pi^0>&= (-1)|\pi^0> \end{aligned} \tag{1–17}$$

In this way, we find that the G-parity for neutral pion is unambiguously fixed to -1. Since the strong interactions conserve isospin and are invariant under charge conjugation, one might expect that the G-parity of $\pi^\pm$ is same as that of π^0. Thus, under G-parity transformation, we have

$$G|\pi^{\pm,0}>= (-1)|\pi^{\pm,0}> \tag{1–18}$$

G-parity is a multiplicative quantum number, therefore, the G-parity of a system of n pions is $(-1)^n$. G-parity is a good quantum number of non-strange mesons and is conserved in strong interactions.

1.1.4 Mesons

At this point, we can introduce the lowest lying mesonic states. From the light[2] quarks u, d, and s we expect nine possible $q\bar{q}$ combinations, thus nine mesons, which break into an octet and a singlet as per $3 \otimes \bar{3} = 8 \oplus 1$. For lowest lying states, it is safe to assume that the relative angular momentum quantum number L is 0. The parity for such states then is $\mathrm{P} = (-1)^{\mathrm{L}+1} = -1$. Since the relative angular momentum is 0, the total angular momentum is same as the spin of the $q\bar{q}$ combination. The two spin-1/2 quarks can be combined either to get total spin 1 (leading to $\mathrm{J}^{\mathrm{P}} = 1^{-}$) or spin 0. States with $\mathrm{S} = 0$ (and therefore $\mathrm{J} = 0$) are pseudoscalar mesons ($\mathrm{J}^{\mathrm{P}} = 0^{-}$), some of which are the subject of interest of this study. The normalized, orthogonal set of octet is

$$
\begin{aligned}
|\pi^{+}> &= u\bar{d} \\
|\pi^{-}> &= d\bar{u} \\
|\pi^{0}> &= \frac{1}{\sqrt{2}}(d\bar{d} - u\bar{u}) \\
|K^{+}> &= u\bar{s} \\
|K^{-}> &= s\bar{u} \\
|K^{0}> &= d\bar{s} \\
|\bar{K^{0}}> &= s\bar{d} \\
|\eta> \approx |\eta_8> &= \frac{1}{\sqrt{6}}(d\bar{d} + u\bar{u} - 2s\bar{s})
\end{aligned}
\tag{1–19}
$$

and the flavor symmetric singlet is

$$
|\eta'> \approx |\eta_0> = \frac{1}{\sqrt{3}}(d\bar{d} + u\bar{u} + s\bar{s}) \tag{1–20}
$$

[2] The quarks u, d, and s are considered as light on the scale of QCD parameter Λ. The quarks c, b, and t are considered as heavy quarks.

Table 1–3. Symbol, name, quark composition, mass in units of MeV/c^2, angular momentum (L), internal spin (S), parity (P), and charge conjugation eigenvalues (C) for a few of the particles used in this analysis.

Symbol	Name	Quark Composition	Mass	I	G	L	S	P	C
$\Upsilon(1S)$	Upsilon(1S)	$b\bar{b}$	9460.30	0	-1	0	1	-1	-1
π^+	Pion	$u\bar{d}$	139.57	1	-1	0	0	-1	x
π^-	Pion	$d\bar{u}$	139.57	1	-1	0	0	-1	x
π^0	Pi0	$\frac{1}{\sqrt{2}}(d\bar{d}-u\bar{u})$	134.98	1	-1	0	0	-1	$+1$
η	Eta	$\frac{1}{\sqrt{6}}(d\bar{d}+u\bar{u}-2s\bar{s})$	547.75	0	$+1$	0	0	-1	$+1$
η'	Eta-prime	$\frac{1}{\sqrt{3}}(d\bar{d}+u\bar{u}+s\bar{s})$	957.78	0	$+1$	0	0	-1	$+1$
ρ^0	Rho0	$\frac{1}{\sqrt{2}}(u\bar{u}-d\bar{d})$	775.8	1	$+1$	0	1	-1	-1
γ	Photon	x	0	0,1	x	x	1	-1	-1

In the real world, the η and η' states are a mixture of η_8 and η_0, with η being "mostly octet" η_8 and η' being "mostly singlet" η_0. The mixing angle between $\eta_8 - \eta_0$ is $\approx -20°$, the consequence of which is that $s\bar{s}$ content is decreased for η and increased for η' [5]. Various properties of pseudoscalar mesons η, η' along with pion triplet are shown in Table 1–3.

If we assume that the masses of quarks u, d, and s is zero, then these particles exhibit $\mathrm{SU(3)_L} \times \mathrm{SU(3)_R}$ chiral[3] symmetry. The Goldstone theorem [6] says that a massless particle (called Goldstone boson) is generated for each generator of the broken symmetry. The SU(3) chiral symmetry is spontaneously broken to vector SU(3), giving rise to eight massless Goldstone bosons which are identified with the octet part of the lowest lying meson nonet. These Goldstone bosons acquire mass due to explicit breaking of the symmetry where quarks have unequal masses.

The singlet η' is very massive compared to the members of octet. This happens because the η' is not a Goldstone boson and acquires mass due to a different mechanism [5].

[3] When the particle mass is zero, the left-handed and right-handed particles are treated differently. This is what we understand by chiral symmetry.

1.2 Quarkonia

Quarkonia are flavor-less mesons made up from a heavy[4] quark and its own anti-quark. Charmonium ($c\bar{c}$) and bottomonium ($b\bar{b}$) are the only examples of quarkonia which can be produced. The bound state $t\bar{t}$ is not expected to be formed as the top quark has a fleeting lifetime owing to its large mass.

In spectroscopic notation, the quantum numbers of quarkonia are expressed as $n^{2\mathrm{S}+1}\mathrm{L_J}$ where n, L, S and J represent the principal quantum number, orbital angular momentum, spin, and total angular momentum respectively. In literature, the $n^3\mathrm{S}_1$ charmonium and bottomonium states are called as $\Psi(n\mathrm{S})$ and $\Upsilon(n\mathrm{S})$ respectively. The combined spin of $q\bar{q}$ in the above mentioned systems is 1. The $q\bar{q}$ relative angular momentum in these mesons is $\mathrm{L} = 0$, i.e., an "S" wave and hence the symbol "S" in the notation. The $n^3\mathrm{S}_1$ quarkonia have $\mathrm{J^{PC}} = 1^{--}$ which is same as that of photon, therefore these mesons can be produced in the decay of virtual photon[5] generated in e^+e^- annihilation carried out at the right center-of-mass energy. The lowest such state is $\psi(1\mathrm{S})$ (commonly called J/ψ), a $c\bar{c}$ state produced at center-of-mass energy 3.09 GeV. The corresponding state for $b\bar{b}$ is $\Upsilon(1\mathrm{S})$, produced at 9.46 GeV.

1.2.1 Decay Mechanisms of $\Upsilon(1\mathrm{S})$

Armed with all the basic information, we are now ready to understand the possible ways in which $\Upsilon(1\mathrm{S})$ can decay. Strong and electro-magnetic interactions conserve color, parity and charge conjugation. These constraints leave very few

---

[4] $q\bar{q}$ states from light quarks u, d, s are rather mixtures of the light quarks than well defined states in terms of quark-antiquark of the same flavor. Even ϕ is also not a pure $s\bar{s}$ state.

[5] Such a photon is called virtual because it cannot conserve the 4-momentum of the initial system (e^+e^- here) and is unstable, existing only for a brief period of time, as allowed by the uncertainty principle, after which it decays to a pair of charged fermion-antifermion.

decay routes open, for example $\Upsilon(1S)$ decay to an even number of photons or an even number of gluons is forbidden by charge conjugation.

The easiest route would have been $\Upsilon(1S)$ decaying into a pair of B mesons, but this is not allowed kinematically. A possible simple decay mechanism is that $b\bar{b}$ pair first interact electro-magnetically and annihilate into a virtual photon. This process is allowed as it does not violate any of the fundamental principals. The virtual photon then readily decays either into a pair of leptons or it decays into a pair of quark-antiquark which further hadronize. On the other hand, the decay of $\Upsilon(1S)$ into a single gluon is forbidden because it violates color conservation. When $\Upsilon(1S)$ decays via intermediate gluons, the minimum number of gluons it should decay to is three so that all the constraints including color conservation are satisfied. In principle, $\Upsilon(1S)$ decay proceeding via three photons is also possible, but this mechanism is highly suppressed as compared to the one proceeding through a virtual photon, just because three successive electro-magnetic interactions are much less likely to occur than a single one.

A very important decay mechanism which has not been introduced so far is the "radiative decay." The decay in this case proceeds through a photon and two gluons. The two gluons can form a color singlet state and the presence of a photon in team with two gluons ensures that parity and charge conjugation are not violated. Naively, the penalty for this replacement of one of the gluons with a photon is of the order of the ratio of coupling constants, $\alpha : \alpha_s$. Despite this suppression, the radiative decays of $\Upsilon(1S)$ are important because emission of a high energy photon leaves behind a glue-rich environment from which we can learn about the formation of resonances from gluons or potentially discover fundamental new forms of matter allowed by QCD like "glueballs" and $qg\bar{q}$ "hybrids." This dissertation concentrates on one class of radiative decays.

The three different possible $\Upsilon(1S)$ decays with least amount of interactions (also called lowest order decays) are shown in Figure 1–2.

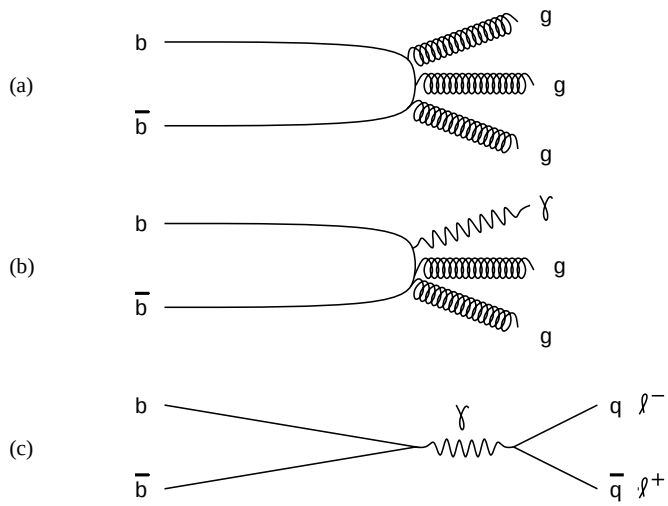

Figure 1–2. Lowest order decays of the $\Upsilon(1S)$ allowed by color conservation, charge conjugation symmetry, and parity. (a) Shows the decay into three gluons, (b) shows a radiative decay, and (c) shows the electro-magnetic decay through a virtual photon that in turn decays electro-magnetically into a pair of charged fundamental particles, such as quarks or charged leptons (the charged leptons are represented by the symbol l).

1.2.2 Radiative Decays of $\Upsilon(1S)$ into η and η'

The radiative decays of heavy quarkonia into a single hadron provide a particularly clean environment to study the conversion of gluons into hadrons, and thus their study is a direct test of QCD. $\Upsilon(1S) \to \gamma\eta'$ is one such channel, involving only single light hadron. This decay channel has been observed in the J/ψ system, as have the decays into other pseudoscalar states, for example the η and $\eta_c(1S)$. Naive scaling predicts a ratio of partial decay widths $\Gamma(\Upsilon(1S) \to \gamma\eta')/\Gamma(J/\psi \to \gamma\eta')$ of $(q_b m_c/q_c m_b)^2 \approx 1/40$. This naive factor of 1/40 is in the decay rates; to find the expected ratio of branching fractions, we have to multiply by the ratio of the total widths, 1.71, which gives a suppression factor of ≈ 0.04. However, the search for the decay $\Upsilon(1S) \to \gamma\eta'$ by CLEO in $61.3\,\mathrm{pb}^{-1}$ of data taken with the CLEO II detector [7] found no signal

in this mode, and resulted in an upper limit of 1.6 $\times 10^{-5}$ for the branching fraction $\Upsilon(1S) \to \gamma\eta'$, which is an order of magnitude less than the naive expectation.

Furthermore, the two-body decay $\Upsilon(1S) \to \gamma f_2(1270)$ has been observed in the old CLEO II $\Upsilon(1S)$ data [8], and this observation has been confirmed with much greater statistics in the CLEO III data [1]. In radiative J/ψ decays the ratio of η' to $f_2(1270)$ production is 3.1±0.4. If the same ratio held in $\Upsilon(1S)$, and as the decay diagram is identical, this would be expected, then the η' channel would be clearly visible. Another interesting channel we study in this analysis is $\Upsilon(1S) \to \gamma\eta$. This channel has been observed in J/ψ decays, albeit with the modest branching fraction of $(8.6 \pm 0.8) \times 10^{-4}$. The previous analysis [9] of $\Upsilon(1S)$ decays produced an upper limit for this mode of 2.1×10^{-5}.

Several authors have tried to explain the lack of signals in radiative $\Upsilon(1S)$ decays into pseudoscalar mesons using a variety of models which produce branching ratio predictions of the order 10^{-6} to 10^{-4}. Körner and colleagues' [10] approach suggests M_V^{-6} dependence for η' and $f_2(1270)$ production in the radiative decays of heavy vector mesons of mass M_V. Using the mixing mechanism of η, η' with the as yet unobserved pseudoscalar resonance η_b, Chao [11] calculates the $\mathcal{B}(\Upsilon(1S) \to \gamma\eta') \approx 6 \times 10^{-5}$, $\mathcal{B}(\Upsilon(1S) \to \gamma\eta) \approx 1 \times 10^{-5}$.

The process V $\to \gamma$ P, where V is the heavy vector meson $\Upsilon(1S), \Upsilon(2S)$ and P is a light pseudoscalar meson (π^0, η, η') was also studied by Intemann [12] using the Vector Meson Dominance Model (VDM). In the VDM paradigm, the decay is assumed to proceed via an intermediate vector meson state, that is V $\to$ V$'$ P $\to \gamma$ P where the virtual V$'$ is a $\Upsilon(1S)$ or $\Upsilon(2S)$. The predicted branching ratios for $\Upsilon(1S) \to \gamma\eta$, $\Upsilon(1S) \to \gamma\eta'$ are $\sim 10^{-7}$ to 10^{-6}. There is an ambiguity regarding the signs of various amplitudes (and thus whether the amplitudes add constructively or destructively to the intermediate virtual vector meson V$'$) that contribute to the partial decay width Γ(V$\to \gamma$ P). The author notes that the amplitudes, if added

constructively, give answers which are in agreement with the experiment for the J/ψ system. Making a note that VDM has no direct relation to QCD as the fundamental theory of strong interactions, and referring to [7], Ma tries to address the problem in Non-Relativistic QCD (NRQCD) [13] paradigm along with twist-2 operators and predicts $\mathcal{B}(\Upsilon(1S) \to \gamma\eta') \approx 1.7\times\ 10^{-6}$, and $\mathcal{B}(\Upsilon(1S) \to \gamma\eta) \approx 3.3\times\ 10^{-7}$, which are almost half the respective ratios predicted using constructive interference VDM approach (Table 1–4).

Table 1–4. Theoretical branching fractions as predicted by various authors for radiative decays of $\Upsilon(1S)$ into η and η'

Author/Model/Approach	Chronology	$\mathcal{B}(\Upsilon(1S) \to \gamma\eta')$	$\mathcal{B}(\Upsilon(1S) \to \gamma\eta)$
QCD inspired models:			
Körner *et al.* [10]	1982	20×10^{-5}	3.6×10^{-5} [6]
Vector Meson Dominance:			
Intemann [12]	1983	5.3×10^{-7} to 2.5×10^{-6}	1.3×10^{-7} to 6.3×10^{-7}
Mixing of η, η' with η_b:			
Chao [11]	1990	6×10^{-5}	1×10^{-5}
NRQCD with twist-2 operators:			
Ma [13]	2002	$\approx 1.7 \times 10^{-6}$	$\approx 3.3 \times 10^{-7}$

In this study, we search for the processes $\Upsilon(1S) \to \gamma\eta'$ and $\Upsilon(1S) \to \gamma\eta$. We reconstruct η mesons in the three modes $\eta \to \gamma\gamma$, $\eta \to \pi^+\pi^-\pi^0$, and $\eta \to \pi^0\pi^0\pi^0$. The η' mesons are reconstructed in the modes $\eta\pi^+\pi^-$ with η decaying through any of the above decay modes. These six decay chains were investigated in the previous

[6] Constructed from table 4 of Ref. [10] as:
$\mathcal{B}(\Upsilon(1S) \to \gamma\eta) = \frac{0.10}{0.24} \times \frac{\mathcal{B}(\psi\to\gamma\eta)}{\mathcal{B}(\psi\to\gamma f_2)} \times \mathcal{B}(\Upsilon \to \gamma f_2)$.

CLEO analysis on this subject. In addition, we have also added the decay mode $\eta' \to \gamma\rho^0$, where $\rho^0 \to \pi^+\pi^-$.

We should also note that we know that five of the seven submodes under investigation are going to be largely background free, and so to get the most sensitivity we must carefully choose our cuts[7] in these submodes to retain the most possible efficiency. The two exceptions are $\eta \to \gamma\gamma$ and $\eta' \to \gamma\rho$. These two have high branching fractions, but large backgrounds, and so our analysis strategy will aim to decrease these backgrounds even if this necessitates a decrease in the efficiency.

For later reference and final calculations, the product branching fractions for the decays modes of η and η' are listed in Table 1–5 where the values have been compiled from PDG[14].

Table 1–5. Product branching ratios for decay modes of η and η'

Decay Mode	Product branching fraction
$\mathcal{B}(\eta \to \gamma\gamma)$	39.43 ± 0.26
$\mathcal{B}(\eta \to \pi^+\pi^-\pi^0)$	22.6 ± 0.4
$\mathcal{B}(\eta \to \pi^0\pi^0\pi^0)$	32.51 ± 0.29
$\mathcal{B}(\eta' \to \pi^+\pi^-\eta)$	44.3 ± 1.5
$\mathcal{B}(\eta' \to \pi^+\pi^-\eta\ ;\ \eta \to \gamma\gamma)$	17.5 ± 0.6
$\mathcal{B}(\eta' \to \pi^+\pi^-\eta\ ;\ \eta \to \pi^+\pi^-\pi^0)$	10.0 ± 0.4
$\mathcal{B}(\eta' \to \pi^+\pi^-\eta; \eta \to \pi^0\pi^0\pi^0)$	14.4 ± 0.5
$\mathcal{B}(\eta' \to \gamma\rho)$	29.5 ± 1.0

[7] In parlance of High Energy Experimental studies, "cut" is a synonym for selection criterion. An event must satisfy a set of cuts to be considered as an event of interest. Cuts are carefully chosen to reject the background events.

CHAPTER 2
EXPERIMENTAL APPARATUS

The first steps towards the study of radiative decays of $\Upsilon(1S)$ resonance is to be able to produce the $\Upsilon(1S)$ resonance, and then to be able to observe the decay daughters of this readily decaying resonance. The Υ resonances are produced only in a high energy collision, the decay daughters of which fly off at relativistic speeds. To detect these daughter particles, a detector is required to be set up around the production point (of the $\Upsilon(1S)$ resonance) which covers as much as possible of the total 4π solid angle. For this analysis, we need a multipurpose detector permitting us to trace the charged tracks back to the production point, identify the particles and detect neutral particles as well. CLEO III detector has been designed to perform the studies of Υ resonances produced by the Cornell Electron Storage Ring.

2.1 Cornell Electron Storage Ring

Located at the Wilson Laboratory's accelerator facility in Cornell University, Ithaca, NY, the Cornell Electron Storage Ring (CESR) is a circular electron-positron collider with a circumference of 768 meters. Since its inception in 1979, it has provided e^+e^- collisions and synchrotron radiation to several experiments.

Various components of CESR as shown in the schematic picture (Figure 2–1) are discussed in the next few sections. The components are discussed in the order in which they are employed to create e^+e^- collisions.

2.1.1 Linear Accelerator

The electrons and positrons used in the collision to produce Υ resonance are produced in a 30 meter long vacuum pipe called the Linear Accelerator (LINAC). The electrons are first created by evaporating them off a hot filament wire at the back of LINAC. In technical parlance, it is the electron gun which produces the electrons,

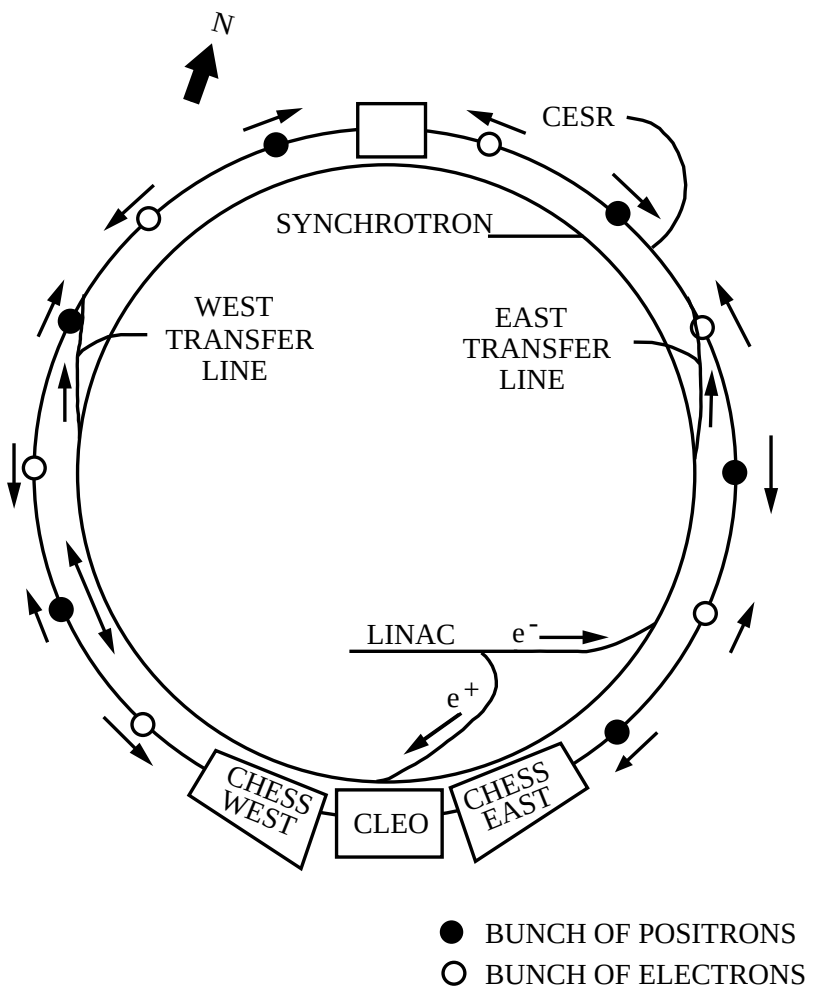

Figure 2–1. Wilson Laboratory accelerator facility located about 40 feet beneath Cornell University's Alumni Fields. Both the CESR and the synchrotron are engineered in the same tunnel.

which is very similar to the procedure inside the picture tube of a television. The electrons thus created are accelerated by a series of Radio Frequency Acceleration Cavities (RF Cavities) to bombard a tungsten target located at about the center of LINAC. The result of the impact of high speed electrons with energy about 140 MeV on the tungsten target is a spray of electrons, positrons and photons. The electrons are cleared away with magnetic field leaving us with a sample of positrons which are further accelerated down the remaining length of LINAC. In case of electrons, the electrons as obtained from the electron gun are simply accelerated down the length

of LINAC without having to bombard the tungsten wire. These accelerated bunch of electrons and positrons are introduced into the synchrotron. This is the process of "filling" a run which normally takes ten minutes.

2.1.2 Synchrotron

The electrons and positrons as filled in the synchrotron are accelerated to the operating energy which is 9.46 GeV in our case, the mass of $\Upsilon(1S)$. The synchrotron is a circular accelerator where the electrons and positrons are made to travel in opposite directions in circular orbits inside a vacuum pipe. The guiding of traveling particles is accomplished via magnetic field, and the acceleration is carried out by radio frequency electro-magnetic field.

In principle, the charged particles can stay in an orbit of a particular radius for a particular velocity for a particular strength of magnetic field. As the particles are accelerated, the value of the magnetic field must be adjusted in synchronism with the velocity to keep the particles in the orbit of constant radius.

2.1.3 Storage Ring

After the electron and positron bunches have reached the operating energy the highly energetic particles are injected into the storage ring. The process of transferring the electron and positron beams into the storage ring (CESR) is called "injection." The beam is guided along a circular path inside the ring by magnetic field and coasts there for roughly an hour, a typical duration of a run. To prevent the electrons and positrons scattering off the gas molecules in the beam pipe, a high quality of vacuum has to be maintained inside the beam pipe.

While the particles coast in the storage ring, they radiate a beam of X-rays thus leading to energy loss. This radiation is called "synchrotron radiation" and is a used for experiments in the CHESS area. The synchrotron radiation is rather a useful by-product used as a research instrument in surface physics, chemistry, biology,

and medicine. The energy lost by the beam in the form of synchrotron radiation is replenished by RF cavities similar to those in the synchrotron.

To avoid the beam collisions anywhere besides the interaction region, the electrostatic separators hold the electron and positron beams slightly apart from each other. The orbit thus is not a perfect circle, it rather assumes the shape of a pretzel.

2.1.4 Interaction Region

The interaction region (IR) is a small region of space located at the very center of the CLEO III detector where the electron and positron beams are made to collide. The rate at which collisions happen directly point to the performance of the accelerator. The ability to obtain a high collision rate is crucial for the success of the accelerator and the experiment it serves. The figure of merit then is the number of possible collisions per second per unit area; this is called the luminosity, which is given as

$$\mathcal{L} = fn\frac{N_{e^+}N_{e^-}}{A} \tag{2–1}$$

where f is the frequency of revolution for each train. n is the number of populated cars in each train for each particle species, A is the cross-sectional area of the cars, and N_{e^+} and N_{e^-} are the numbers of positrons and electrons per car, respectively. In order to maximize the luminosity, the beams are focussed as narrow as possible in the IR. To this end, several magnetic quadrupole magnets were added to CESR during CLEO III installation.

A standard practice of measuring the integrated luminosity over a period of time in high energy experiments is to count how many times a well understood reference process occurs during a certain time interval at the IR. The two reference processes that are used at CLEO III detector are, one e^+e^- interacting to produce a new e^+e^- pair, and second e^+e^- annihilating to produce a pair of photons. Using the well known cross-section for each process, the number of events is converted to a

luminosity called the Bhabha integrated luminosity for the first process, and the $\gamma\gamma$ (GamGam) integrated luminosity for the second one.

2.2 Υ Resonances

The family of Υ resonances was discovered in 1977 in Fermilab. The experiment conducted at Fermilab was unable to resolve the members of this family, however, it was certain that a bound state of a new flavor, bottom, was discovered. Soon, CLEO detector operating at CESR was able to resolve the states Υ(1S), Υ(2S), and Υ(3S). These resonances are shown in Figure 2–2 on top of hadronic "background." The fourth state discovered in 1980, namely Υ(4S) is much wider compared to low-lying Υ states as Υ(4S) has more decay channels open to it.

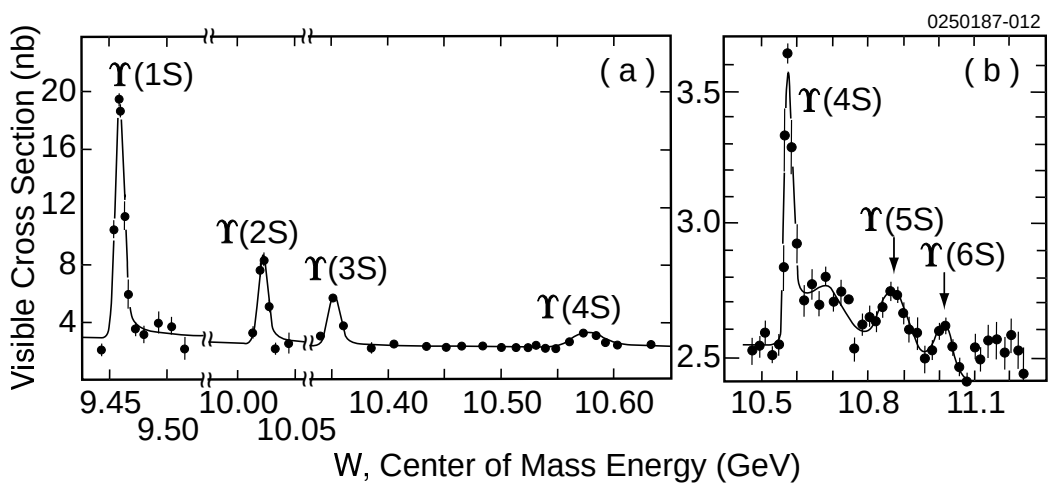

Figure 2–2. Visible cross section in e^+e^- collisions as a function of center of mass energy. Plot (a) on the left shows peaks for $\Upsilon(n\mathrm{S})$ for n = 1,2,3, and 4. Plot (b) on the left shows Υ(5S) and Υ(6S) as well as a blow up for Υ(4S) resonance.

The composition of hadronic background is primarily from the "continuum" process $e^+e^- \to q\bar{q}$, where q is a light quark (u, d, s, as well as c at this energy). The process is referred to continuum as this process happens for a range of operating energy high enough to produce the light quarks. Some contribution to the hadronic continuum also comes from the process $e^+e^- \to \tau^+\tau^-$, where one or both τ leptons

decay to hadronic daughters. To study the decay processes of Υ resonances, we not only need the data collected at the operating energy equal to the mass of resonance under study, but we also need a sample of pure continuum at operating energy just below[1] the resonance to understand the background.

2.3 CLEO III Detector

The colliding e^+e^- annihilate electro-magnetically into a virtual photon γ^*, a highly unstable "off mass shell" particle decaying readily into "on shell" daughters. Even at the operating energy equal to the mass of $\Upsilon(1S)$ resonance, the virtual photon may either produce the resonance $\Upsilon(1S)$, or produce the continuum background. We really do not have any means of directly knowing what happens at the interaction point. But the long lived on-shell daughters flying off at relativistic speeds possess the information post-collision process as to what Nature decided to do with the energy. It is at this point we enter the world of particle detectors.

Like any other probe, to measure a certain quantity, the probe should be able to interact with the quantity. The underlying principles of particle detectors are based upon the electro-magnetic interactions of particle with matter (the detector here). The particle detectors are sensitive to such interactions and are equipped with instruments to record the information about interaction, which is used by experimenter to infer the properties of the interacting particle, such as its energy, momentum, mass and charge.

In this analysis, we are interested in the process where a γ^* first decays into $\Upsilon(1S)$ resonance which further decays radiatively into a η and η' mesons. The light, pseudoscalar mesons η and η' themselves are highly unstable and readily decay into

[1] The reason for collecting the continuum sample at an energy below and not above the resonance energy is that at an energy above the resonance, the colliding particles may radiate photon(s), thereby losing energy and possibly forming the resonance.

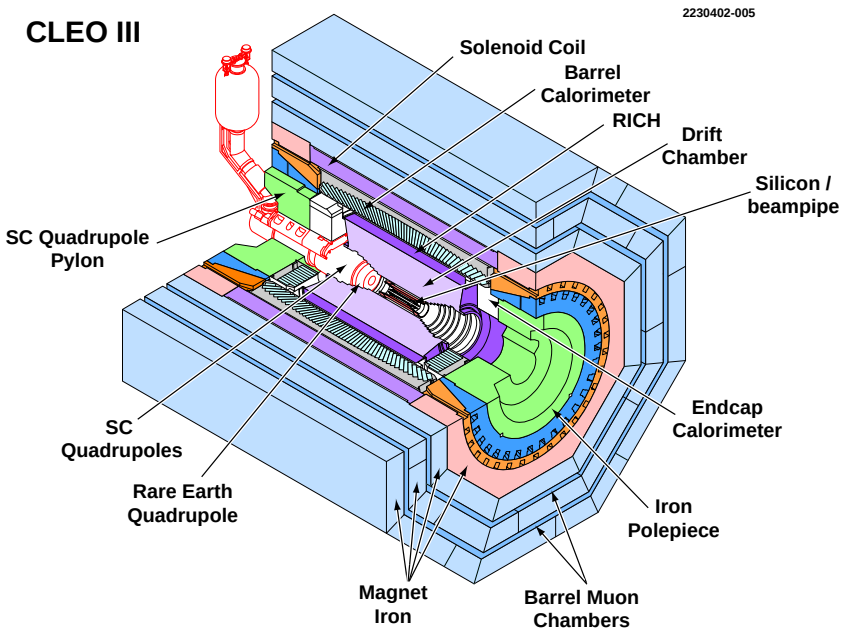

Figure 2–3. The CLEO III detector.

lighter particles long lived enough to survive the volume of detector. It is these particles that we detect using the CLEO III detector [15], a major upgrade to CLEO II.V [16] having an improved particle identification capability along with a new drift chamber and a new silicon vertex detector. As the suffix III to the name CLEO suggests, there have been many generations of CLEO detectors evolved from the original CLEO detector. As can be seen in Figure 2–3, the CLEO III detector is a composite of many sub-detector elements. Typically arranged as concentric cylinders around the beam pipe, the sub-detectors are generally specialized for one particular task. The entire detector is approximately cube shaped, with one side measuring about 6 meters, and weighs over 1000 tons. CLEO III operated in this configuration from 2000 to 2003.

The CLEO III detector is a versatile, multi-purpose detector with excellent charged particle and photon detection capabilities. In the following sections, we discuss some of the particle detection schemes and techniques implemented in the

CLEO detectors, and how raw detector data is transformed into measurements of particle energy, momenta, trajectories. A thorough description of the detector can be found elsewhere [17].

2.3.1 Superconducting Coil

All the CLEO III detector subsystems except the muon chambers are located inside a superconducting coil. The superconducting coil is a key element, providing a uniform magnetic field of 1.5 Tesla to bend the paths of charged particles in the detector, thus allowing the experimenter to measure the momentum of the passing particle. The magnetic field due to the coil points in $-z$ direction (east) and is uniform up to 0.2%.

The 3.5 meter long coil has an inner diameter of 2.90 meter with a radial thickness of 0.10 meter. The winding around the coil is carried from a 5 mm $\times$ 16 mm superconducting cable made from aluminum stabilized Cu-NbTi alloy kept in superconducting state by the liquid helium reservoir as shown in Figure 2–3. The coil is wound in 2 layers, each having 650 turns, on an aluminum shell. When in operation, a current of 3300 amps flows through the coil.

2.3.2 Charged Particle Tracking System

The particles created at the interaction point pass the low-mass beam pipe before they begin to encounter the active elements of detector tracking system. The CLEO III tracking system is responsible for tracking a charged particle's trajectory and thus giving the experimenter a measure of the particle momentum. The tracking system of CLEO III detector is composed of two sub-detectors to accomplish the tracking of curved path of charged particles. The first sub-detector is silicon vertex detector measuring z and the cotangent of polar angle θ, surrounded by the central drift chamber measuring the curvature. Both devices measure the azimuthal angle ϕ and the impact parameter.

The typical momentum resolution is 0.35% (1%) for 1 GeV (5 GeV) tracks. The tracking system also measures the ionization energy loss due to charged particles — a measurement useful in distinguishing between various mass hypotheses of charged particles. The energy loss due to ionization is measured with an accuracy of about 6% for hadrons (pion, kaon, and proton), and 5% for electrons. The tracking system is not sensitive to neutral particles.

2.3.2.1 Silicon Vertex Detector

The silicon vertex detector in CLEO III [18], also called SVD III is a silicon strip detector "barrel-only" design without endcaps or tapers, consisting of four silicon layers concentric with the IR beam pipe. The silicon tracker provides four ϕ and four z measurements covering 93% of the solid angle. The average radius of inner surface of the four layers is 25 mm, 37.5 mm, 72 mm and 102 mm. Each of the four barrels is constructed from independent chains (called ladders) which are made by connecting individual silicon wafers (sensors) together. There are a total of 447 identical double-sided silicon wafers, each 27.0 mm in ϕ, 52.6 mm in z and 0.3 mm thick used in constructing the four barrels. The four layers have respectively 7, 10, 18, and 26 ladders, and the four ladder design consists of respectively 3, 4, 7, and 10 silicon wafers daisy chained longitudinally (Figure 2–4).

The bottom side of each silicon wafer has n-type strips implanted perpendicular to the beam line. The top side of the wafer has p-type implants parallel to the beam line. The wafers are instrumented and read out on both sides. Each wafer has 512 strips on either side. The instrumentation on each side consists of aluminized traces atop the doped strips. The so formed aluminum strips are connected to preamplifiers stationed at the end of the detector and move the collected charge from the wafers. The entire wafer forms a p-n junction. When reverse bias is applied across the wafer, a sensitive region depleted of mobile charge is formed.

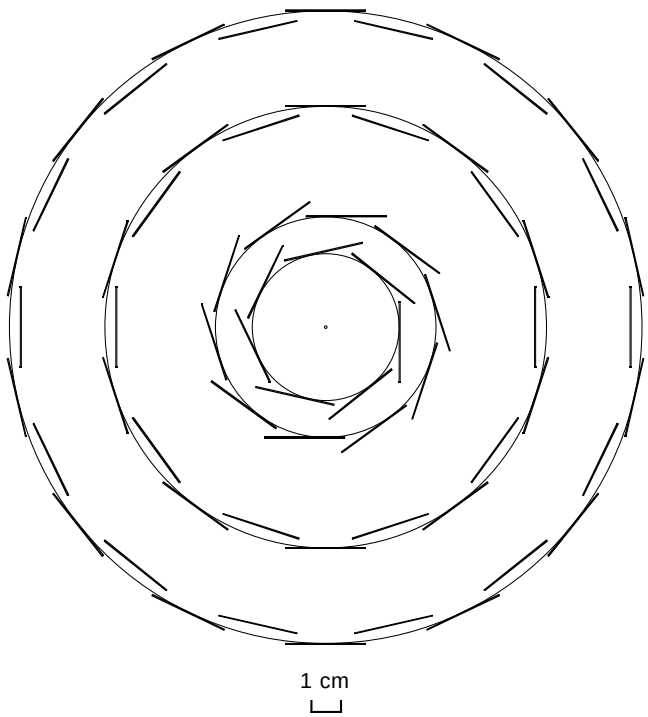

Figure 2–4. View of the SVD III along the beampipe.

As in any other material, charged particles traversing the wafer lose energy. In the sensitive region of the wafer, this lost energy is used to create electron-hole pairs. Approximately 3.6 eV is required to create a single electron-hole pair. The liberated electrons and holes then travel (in opposite directions) in the electric field applied by the bias to the surfaces of the wafers until they end up on the aluminum strips, and then the detector registers a "hit." When combined together, the hit on the inner side of a wafer and the hit on the outer side give a measurement of (z, ϕ). The wafer position itself determines r.

2.3.2.2 The Central Drift Chamber

The CLEO III central drift chamber (DR III) is full of drift gas with 60:40 helium-propane mixture held at about 270 K and at a pressure slightly above one atmosphere. The drift chamber is strung with an array of anode (sense) wires of gold-plated tungsten of 20 μm diameter and cathode (field) wires of gold-plated

aluminum tubes of 110 μm diameter. All wires are held at sufficient tension to have only a 50 μm gravitational sag at the center ($z = 0$). The anodes are kept at a positive potential (about 2000 V), which provides an electric field throughout the volume of the drift chamber. The cathodes are kept grounded, and shape the electric field so that the fields from neighbouring anode wires do not interfere with each other.

During its passage through the DR III, the charged particle interacts electro-magnetically with the gas molecules inside the chamber. The energy is transferred from the high energy particle to the gas molecule thereby ionizing the gas by liberating the outer shell electrons. The liberated electrons "drift" in the electric field towards the closest sense wire. The thin sense wire maintained at a high potential produces a very strong electric field in its vicinity. As the electron approaches the sense wire, it gains energy enough to become an ionizing electron itself thereby kicking more electrons out of the surrounding gas molecules. An avalanche of electrons is created this way which collapses on the sense wire in a very short amount of time (less than a nanosecond) and the sense wire registers a "hit."

The current on the anode wire from the avalanche is amplified and collected at the end of the anode wire. Both the amount of charge and the time it takes it to move to the end of the detector are measured. A calibration of the drift chamber is used to convert the amount of charge to a specific ionization measurement of the incident particle. A calibrated drift chamber can also convert the time to roughly measure the position along the sense wire where the charge was deposited.

The CLEO III DR has 47 layers of wires, the first 16 of which form the inner stepped section ("wedding cake" end-plates) where in the wires are strung along the z-direction. These wires are called axial wires. The remaining outer 31 layers are small angle stereo layers. The stereo wires are strung in with a slight angle (about 25 milliradians) with respect to the z-direction to help with the z measurement. There are 1696 axial sense wires and 8100 stereo sense wires, 9796 total. For stereo tracking,

the tracker divides the 31 stereo layers into eight super layers, the first seven of which have four layers of stereo wires each, and the last super layer has only three layers of wires. The odd and even numbered super layers have a positive and negative phi tilt with respect to the z, respectively. The odd(even) super layers are called as U(V) super layers in short.

There are 3 field wires per sense wire and the 9796 drift cells thus formed are approximately 1.4 cm side square. The drift position resolution is around 150 μm in $r - \phi$ and about 6 mm in z.

2.3.3 Ring Imaging Cherenkov Detector

Cherenkov radiation detectors belong to the set of tools to discriminate between two particles of same momentum and different masses. This goal is accomplished by measuring the velocity of the charged particle and match it against the momentum measured by the tracking chamber. This goal is termed as "particle identification."

The CLEO III detector received its major upgrade for the purpose of particle identification by replacing the existing time of flight system of CLEO II.V detector by Ring Imaging Cherenkov Detector (RICH). Both systems, the old time of flight detector and the new RICH sub-detector provide the measurement of particle velocity.

The underlying principle behind the RICH is the phenomenon of Cherenkov radiation. The Cherenkov radiation occurs when a particle travels faster than the speed of light in a certain medium,

$$v > c/n. \tag{2–2}$$

where v is the velocity of the particle, c is the speed of light in free space and n is the index of refraction of the medium the particle is traveling in. The charged particle, as it travels through medium, polarizes the molecules of the medium. The polarized molecules relax to their ground state in no time, emitting photons. Because the charged particle is traveling faster than the speed of light in the medium, it triggers a

cascade of photons which are in phase with each other and can constructively interfere to form a coherent wavefront. The Cherenkov light wavefront forms the surface of a cone about the axis of charged particle trajectory, where the half-angle θ of the cone is given by

$$\cos(\theta) = \frac{c}{vn} = \frac{1}{\beta n}, \qquad \beta > \frac{1}{n} \tag{2–3}$$

The measurement of θ is thus a measurement of particle's speed which when related to the measured momentum of the particle gives a measurement of the particle mass, and is useful in particle identification.

As can be noted from the conditions under which Cherenkov radiation is emitted, the charged particle has to have a threshold velocity $v_{min} = c/n$ before the radiation can be emitted. At threshold, the cone has a very small half-angle $\theta \approx 0$. The maximum emission angle occurs when $v_{max} = c$ and is given by

$$\cos(\theta_{max}) = \frac{1}{n}. \tag{2–4}$$

The RICH (see Figure 2–5) starts at a radius of 0.80 m and extends to 0.90 m has a 30-fold azimuthal symmetry geometry formed from 30 modules, each of which is 0.192 m wide and 2.5 m long. Each module has 14 tiles of solid crystal LiF radiator at approximately 0.82 m radius. Each tile measures 19.2 cm in width, 17 cm in length and a mean thickness of 10 mm. Inner separation between radiators is typically 50 μm. The LiF index of refraction is $n = 1.5$. The radiators closest to $z = 0$ in each module have a 45 degree sawtooth outer face to reduce total internal reflection of the Cherenkov light for normal incident particles (see Figure 2–6). The radiators are followed by a 15.7 cm radial drift space filled with pure N_2, an un-instrumented volume allowing the expansion of Cherenkov cone. The drift space is followed by the photo-detector, a thin-gap multi-wire photosensitive proportional chamber filled with a photon conversion gas of triethylamine and methane where the Cherenkov cone is intercepted.

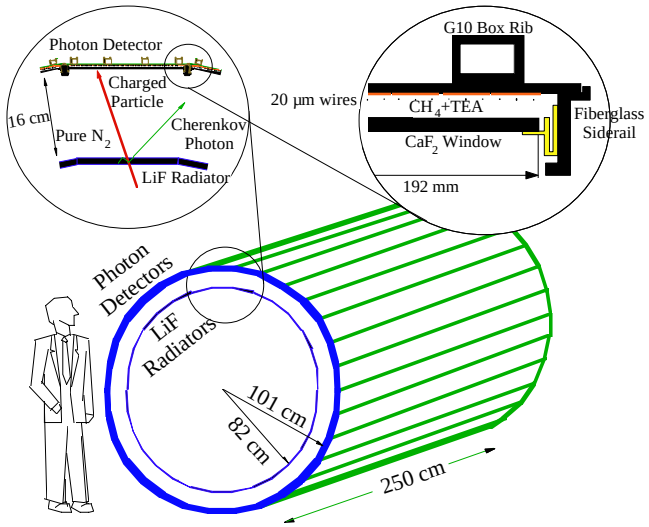

Figure 2–5. The RICH detector subsystem.

With this index, particles in the LiF radiator with $\beta = 1$ produce Cherenkov cones of half-angle $\cos^{-1}(1/n) = 0.84$ radians. With a drift space $\simeq$ 16 cm in length, this produces a circle of radius 13 cm. The RICH is capable of measuring the Cherenkov angle with a resolution of a few milliradians. This great resolution allows for good separation between pions and kaons up to about 3 GeV.

2.3.4 Crystal Calorimeter

Calorimeters perform energy measurements based upon total absorption methods. The absorption process is characterized by the interaction of the incident particle in a detector mass, generating a cascade of secondary, tertiary particles and so on, so that all (or most) of the incident energy appears as ionization or excitation in the medium. A calorimeter, is thus an instrument measuring the deposited energy. The calorimeter can detect neutral as well as charged particles. The fractional energy resolution of calorimeters is generally proportional to $E^{-1/2}$, which makes them even more indispensible in yet higher energy experiments.

The CLEO III Crystal Calorimeter (CC) is an electro-magnetic-shower calorimeter which absorb incoming electrons or photons which cascade into a series of electro-magnetic

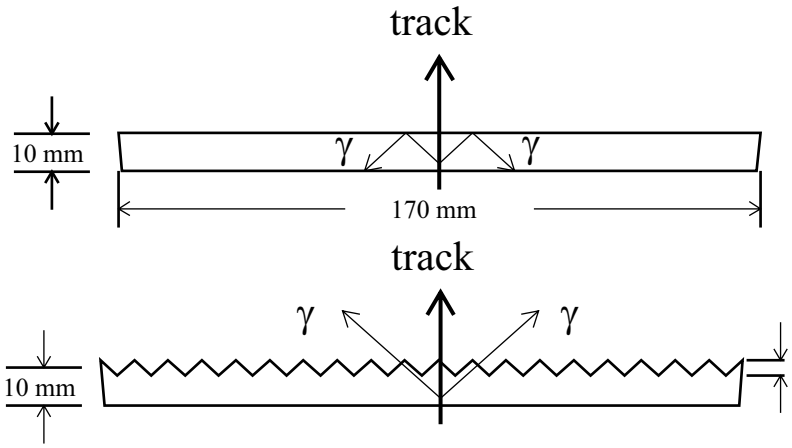

Figure 2–6. Two kinds of RICH LiF radiators. For normal incidence particles ($z \approx 0$) a sawtooth radiator is necessary to avoid internal reflection.

showers. It is vital sub-detector for the analysis presented in this dissertation, as all our events contain at least two, mostly three, and often more, photons. The calorimeter is constructed from 7784 thallium-doped CsI crystals with 6144 of them arranged to form the barrel portion and the remaining 1640 are evenly used to construct two endcaps, together covering 95% of the solid angle. The crystals in the endcap are rectangular in shape and are aligned parallel to the z axis whereas the crystals in the barrel are tapered towards the front face and aligned to point towards the interaction point so that the photons originating from the interaction point strike the barrel crystals at near normal incidence. The CC barrel inner radius is 1.02 m, outer radius is 1.32 m, and length in z at the inner radius is 3.26 m. It covers the polar angle range from 32 to 148 degrees. The endcap extends from 0.434 m to 0.958 m in radius. The front faces are $z = \pm 1.308$ m from the interaction point (IP); the back faces are $z = \pm 1.748$ m from the IP. It covers the polar angle region from 18 to 34 degrees in $+z$, and 146 to 162 in $-z$.

The electronic system composed of 4 photodiodes present at the back of each of the crystals are calibrated to measure the energy deposited by the incoming particles. Incoming particles other than photons and electrons are partially, and sometimes fully,

absorbed by the crystals giving an energy reading. Each of the crystals is 30 cm long which is equivalent to 16.2 radiation lengths. On the front face, the crystals measure 5 cm $\times$ 5 cm, providing an angular resolution of 2 milliradians. The photon energy resolution in the barrel (endcap) is 1.5% (2.5%) for 5 GeV photons, and deteriorates to 3.8% (5.0%) for 100 MeV photons.

2.3.5 Muon Chambers

Muons are highly penetrating charged particles which compared to other charged particles, can travel large distances through matter without interacting. For this reason, the sub-detector component Muon Detector used in identifying muons is placed outside the main body of CLEO III detector.

The muon detectors are composed of plastic stream counters embedded in several layers of iron. Particles other than muons emanating from the detector are blocked by the iron layers. Like the CC, the muon detector is arranged as a barrel and two endcaps, covering 85% of the 4π solid angle (roughly 30–150 degrees in polar angle). The barrel region is divided in 8 octants in ϕ, with three planes of chambers in each octant. The plastic barrel planes lie at depths of 36, 72, and 108 cm of iron (at normal incidence), corresponding to roughly 3, 5, and 7 hadronic interaction lengths (16.8 cm in iron) referred to as DPTHMU. There is one plane of chambers in each of the two endcap regions, arranged in 4 rough quadrants in ϕ. They lie at $z = \pm 2.7$ m, roughly covering the region $0.80 < |\cos(\theta)| < 0.85$. The planar tracking chambers use plastic proportional counters at about 2500 V with drift gas of 60% He, 40% propane, identical to (and supplied by the same system as) the drift chamber gas. Individual counters are 5 m long and 8.3 m wide, with a space resolution (along the wire, using charge division) of 2.4 cm. The tracking chambers are made of extruded plastic, 8 cm wide by 1 cm thick by 5 m long, containing eight tubes, coated on 3 sides with graphite to form a cathode, with 50 μm silver-plated Cu-Be anode wires held at 2500 V. The orthogonal coordinate is provided by 8 cm copper strips running perpendicular to the

tubes on the side not covered by graphite. When a hit is recorded, the anode wire position provides the ϕ coordinate of the hit, and charge division is used to extract the z coordinate.

Besides detecting muons, the heavy iron layers also act as magnetic flux return yoke for the superconducting coil. The other important purpose served by iron layers is to protect the inner sub-systems of CLEO III detector from cosmic ray background (except for cosmic ray muons of course).

2.3.6 CLEO III Trigger

The CLEO III trigger described fully in [19] is both a tracking and calorimeter based system designed to be highly efficient in collecting events of interest. The tracking based trigger relies on "axial" and "stereo" triggers derived from the hit patterns (pattern recognition performed every 42 ns) on the 16 axial layers and 31 stereo layers of the drift chamber. As there are only 1696 axial wires in the CLEO III drift chamber, the tracker is able to examine all possible valid hit patterns due to tracks having transverse momentum $P_\perp$ greater than 200 MeV/c. To maintain high track finding efficiency, the hit patterns due to tracks as far as 5 mm away from the axis of beam pipe are included, and upto two hits (one each from the inner and outer set of eight wires) are allowed to be missing. The output from axial trigger is the number of tracks, the event time and a 48-bit array representing event topology. Since the number (8100) of stereo wires is relatively large, not all wires are examined for hit pattern, rather the wires are grouped in 4x4 arrays (for super layer 8, it uses 4x3 array). The U and V super layers (defined in Section 2.3.2.2) are examined separately (as they tilt in opposite directions) and to satisfy a block pattern, at least 3 out of the 4 layers in a super layer must record hits from tracks satisfying the momentum cut $P_\perp > 250$ MeV/c. This is designed to maintain high efficiency; however, missing blocks are not allowed. The stereo track output is projected in azimuth on to the axial layer 9 (to match with the axial tracks) and the CC on the other end. A more

detailed discussion is beyond the scope of this dissertation; suffice it is to say that the information from axial and stereo parts of tracker is combined to deduce tracking correlation. The tracks matched in both regions are tagged as "long," carrying more weight in trigger decision compare to the axial only "short" tracks.

The calorimeter-based trigger is designed to be more efficient in CLEO III than its predecessors. The energy deposited in overlapping 2x2 array of 4x4 crystal tiles (altogether 64 crystals) is summed and compared against three thresholds, low (150 MeV), medium (750 MeV), and high (1.5 GeV). The scheme of overlapping tiles (also called tile sharing) did not exist in CLEO II.V and CLEO II detectors, so the calorimeter-based trigger was not as efficient, because a shower shared by crystals spanning a boundary of tiles could be below threshold in both regions, thus failing the trigger condition. Some decay modes studied in this dissertation rely purely on the calorimeter-based trigger decision, and the redesigned CLEO III calorimeter trigger is an added advantage.

Based upon tracking and calorimetry trigger bits, many different trigger lines (or conditions) are checked and an event is recorded if at least one line is set. The calorimeter based trigger lines are important for the "all neutral" modes $\Upsilon(1S) \to \gamma\eta; \eta \to \gamma\gamma$ and $\Upsilon(1S) \to \gamma\eta; \eta \to \pi^0\pi^0\pi^0$ studied in this dissertation. The two trigger lines which help collect events for the above modes are

- BARRELBHABHA, demanding there are two, back-to-back high energy shower clusters in the barrel region. For being classified as back-to-back, the showers should be in opposite halves of the barrel and the ϕ angle should be such that if one shower is in octant 1 (0 to 45 degrees in ϕ), then the other shower should be in octants 4,5, or 6 (135 to 270 degrees in ϕ), for example.

- ENDCAPBHABHA, requiring there are two high energy shower clusters, one in each of the two endcaps.

For the modes with charged tracks, the trigger lines have again very relaxed criteria ensuring high efficiency. The important trigger lines are

- ELTRACK, demanding a medium energy shower cluster in the barrel region accompanied by at least one axial track. It is very easy to see that this line would be highly efficient if the radiative photon hits the barrel region.

- RADTAU, demanding two stereo tracks accompanied with either a medium energy shower cluster in the barrel region, or two low energy shower clusters in the barrel region.

- 2TRACK, demanding two axial tracks. This trigger line is pre-scaled by a factor of 20.

CHAPTER 3
DATA ANALYSIS

3.1 Data

This study is based upon the data sets 18 and 19 collected with CLEO III detector during the running period January 2002 through April 2002 at center-of-mass energy 9.46 GeV. The acquired luminosity was $1.13 \pm 0.03\,\mathrm{fb}^{-1}$ with the beam energy range 4.727–4.734 GeV. This $\Upsilon(1S)$ on-resonance data contains both resonant $e^+e^- \to \Upsilon(1S)$ and continuum events. The number of resonant events available to us, $N_{\Upsilon(1S)} = 21.2 \pm 0.2 \times 10^6$ [20], is roughly 14 times the 1.45×10^6 $\Upsilon(1S)$ mesons used in the previous search [7, 9] using data collected with CLEO II detector. In order to understand the continuum background present in the $\Upsilon(1S)$ on-resonance data, a pure continuum data sample is available to us collected at the center-of-mass energy below the $\Upsilon(1S)$ energy ($E_{beam} = 4.717$–4.724 GeV) with an integrated luminosity of $0.192 \pm 0.005\,\mathrm{fb}^{-1}$. Unfortunately, if we use this data to represent our background, we first have to scale it by the large factor of 5.84, which leads to large statistical uncertainties. However, in this analysis, we can also use the large data sample taken on and near the $\Upsilon(4S)$ as a good source of pure continuum events. Many of these events are of the form $\Upsilon(4S) \to B\bar{B}$ decays, but these will not satisfy our selection criteria leaving only continuum events. Thus, we use $\Upsilon(4S)$ datasets 9, 10, 12, 13, and 14 as a model of our continuum background, with integrated $\mathcal{L} = 3.49 \pm 0.09\,\mathrm{fb}^{-1}$ in the beam energy range 5.270–5.300 GeV.

We note that in this analysis, we use the "GamGam" luminosity, rather than using the more commonly used (and more statistically precise) "BhaBha" measure of the luminosity. This is because the measured Bhabha luminosity at $\Upsilon(1S)$ energy is increased by $\sim 3\%$ owing to the resonant process $\Upsilon(1S) \to e^+e^-$, and this must be

accounted for while doing the continuum subtraction. By using GamGam luminosity, we avoid this complication and its associated uncertainty. Statistical details of the data used are listed in Table 3–1.

Table 3–1. Luminosity numbers for various data sets used in the analysis

	Υ(1S)	Υ(4S)	Υ(1S)-off
Dataset	18, 19	9, 10, 12, 13, 14	18, 19
Average E_{beam}(GeV)	4.730	5.286	4.717
Range of E_{beam}(GeV)	$4.727 - 4.734$	$5.270 - 5.300$	$4.714 - 4.724$
$\mathcal{L}(e^+e^-)$(fb^{-1})	1.20 ± 0.02	3.56 ± 0.07	0.200 ± 0.004
$\mathcal{L}(\gamma\gamma)$(fb^{-1})	1.13 ± 0.03	3.49 ± 0.09	0.192 ± 0.005
Υ(1S) continuum scale factor	1	0.404	5.84

3.2 Skim and Trigger Efficiency

After the e^+e^- collision happens, the triggered events are collected by the CLEO III detector. In CLEO terminology this procedure is called as "pass1." The raw data as collected by the detector is processed and stored in convenient data structures so that an average collaborator can use the data seamlessly in her analysis. This data processing phase is called "pass2." At this stage, the events are classified into various event-types and stored into different groups called sub-collections, depending upon the characteristics of the event. In a typical analysis, not all collected events are useful, so the first step is to make skim of the events of interest.

As our signal events are low multiplicity, we need to ensure that we have triggered on the events reasonably efficiently, and furthermore, having collected the events online, we need to know which pass2 sub-collection the events are to be found so that we can skim the events off at Cornell. Using the event generator QQ [21], we generated signal Monte Carlo (MC) events for the processes $e^+e^- \to \gamma^* \to \gamma\eta'$ and $e^+e^- \to \gamma^* \to \gamma\eta$ using "model 1" with the $(1+\cos^2\theta)$ angular distribution expected

for decays $\Upsilon(1S) \rightarrow \gamma +$ pseudoscalar for each mode, at a center-of-mass energy 9.46 GeV.

The MC predicted that ELTRACK (trigger lines described in Section 2.3.6) was the most significant trigger line for our events that have charged tracks. On the other hand, for "all neutral" modes $\Upsilon(1S) \rightarrow \gamma\eta; \eta \rightarrow \gamma\gamma$ and $\Upsilon(1S) \rightarrow \gamma\eta; \eta \rightarrow \pi^0\pi^0\pi^0$, the trigger lines BARRELBHABHA or ENDCAPBHABHA were satisfied efficiently. For modes with charged tracks, hardGam event-type was by far the most important. For an event to be classified as hardGam, all the criteria listed below must be satisfied:

- eGam1 > 0.5, the highest isolated shower energy relative to the beam energy.
- eSh2 < 0.7, second most energetic shower energy relative to the beam energy.
- eOverP1 < 0.85, the matched calorimeter energy for the most energetic track divided by the measured track momentum. If the event has no reconstructed tracks, the eOverP1 quantity is assigned a default value of zero.
- eVis > 0.4, assuming pion hypothesis, the total measured energy relative to the center-of-mass energy. The energy matched to the charged tracks is excluded while summing up total energy.
- aCosTh < 0.95, absolute value of z-component of unit net momentum vector.

For all-neutral modes, the significant event-types are gamGam, radGam and hardGam, the significance not necessarily in this order. The gamGam event-type has to pass the fairly simple tests - nTk , the number of reconstructed charged tracks < 2, and eSh2 > 0.4 (see hardGam). A radGam event-type is necessarily gamGam event-type with the additional requirement that eSh3, the energy of third most energetic shower relative to the beam energy should be > 0.08 and eCC, the total energy deposited in the calorimeter be less than 75% of the center-of-massenergy. Due to the softer eSh2 criterion for hardGam, events for the all neutral mode $\eta \rightarrow \pi^0\pi^0\pi^0$ are classified as hardGam more frequently than gamGam or radGam.

For the mode $\Upsilon(1S) \rightarrow \gamma\eta; \eta \rightarrow \gamma\gamma$, however, the decay of high energy η into two photons always satisfied eSh2 > 0.4 , thus gamGam is the most efficient followed

by radGam. However, during the course of analysis, it was learnt that a cut on the energy asymmetry (defined later in Section 3.3.3) of the two photons helps us reduce the background by a large proportion. This cut was conveniently chosen to be < 0.8, which throws away all the events of type gamGam which have not been classified as radGam as well. We thus can select only radGam event-types for $\eta \to \gamma\gamma$ skim.

In addition to the sub-collection/event-type cuts, the following topological cuts were required during the skimming process:

- The topology of radiative $\Upsilon(1S)$ decays is very distinctive. They have a high momentum photon, of energy similar to the beam energy, and a series of particles on the away side of the event. Thus, we require the existence of a shower with measured energy $> 4.0\,\mathrm{GeV}$ having the shower profile consistent with a photon. To such a shower, we refer as hard photon.

- We require the NTracks cut to be satisfied. This term means differently for different modes. For modes with no charged tracks in them, we require NTracks, the number of reconstructed tracks (good or bad) be 0 . For modes with charged tracks, we require NTracks to have at least 1 or 2 pairs of oppositely charged, "good tracks" for 2, 4 tracks modes respectively. A "good track" should have:

1. $|d0|$, the distance of closest approach of the charged track to the origin of CLEO coordinate system should be less than 5 mm.

2. $|z0|$, the z measurement of the track position at the point of closest approach to the CLEO coordinate system should be less than 10 cm.

3. The momentum $|\vec{p}|$ of charged track should be such that $200\,\mathrm{MeV} < |\vec{p}| < 5.3\,\mathrm{GeV}$.

Selection criteria used in the skimming process are referred to as "basic cuts." Tables 3–2 and 3–3 quantify the basic cuts' efficiencies for decay modes of η and η' respectively. Please note that most of the tables from now on have columns bearing two labels, "ind" and "cmb" whenever we talk about the efficiency of a selection criterion listed in a particular row. The column labeled with "ind" stands for the efficiency of the individual cut under consideration and "cmb" stands for the combined efficiency of all the selection criteria which have been used so far, including the current

cut under consideration. With this legend, we would read the $\eta \to \gamma\gamma$ column in Table 3–2 as 73.5% efficiency for trigger alone (and also 73.5% in the "cmb" column as this is the first cut). Next level4 cut is applied which has individual efficiency as 93.2%, but the efficiency is 73.5% after applying both the trigger and level4 cuts, and so on.

Table 3–2. Efficiency (in %) of basic cuts for η modes

Mode →	$\eta \to \gamma\gamma$		$\eta \to \pi^+\pi^-\pi^0$		$\eta \to \pi^0\pi^0\pi^0$	
Events Generated	25000		25000		25000	
Cut	ind	cmb	ind	cmb	ind	cmb
Trigger	73.5	73.5	85.1	85.1	70.6	70.6
Level4	93.2	73.5	93.5	84.7	93.0	70.6
Event Type	68.4	56.0	76.3	71.1	71.2	54.6
Hard Photon	85.2	54.3	83.3	68.6	83.2	52.5
NTracks	89.1	53.4	92.9	68.1	78.2	44.6

Table 3–3. Efficiency (in %) of basic cuts for η' modes

Mode →	η' ; $\eta \to \gamma\gamma$		η' ; $\eta \to \pi^+\pi^-\pi^0$		η' ; $\eta \to \pi^0\pi^0\pi^0$		$\eta' \to \gamma\rho$	
Events Generated	24967		25000		25000		25000	
Cut	ind	cmb	ind	cmb	ind	cmb	ind	cmb
Trigger	87.6	87.6	89.4	89.4	85.9	85.9	85.5	85.5
Level4	94.0	87.3	94.5	88.8	93.7	85.6	93.8	84.8
Event Type	67.5	64.5	74.1	71.9	73.0	69.1	75.2	70.8
Hard Photon	83.2	61.6	83.3	69.2	82.5	66.2	82.9	67.9
NTracks	92.0	61.0	80.5	60.9	92.0	65.6	90.6	66.7

To further reduce the skim size, we carried the skimming procedure through another iteration. For each of the modes, complete decay chain was reconstructed with very loose cuts. The $\pi^0 \to \gamma\gamma$ and $\eta \to \gamma\gamma$ candidates were constrained to their nominal masses, and restricted in the invariant mass window 50–230 MeV/c^2 and 350–900 MeV/c^2 respectively. The photon candidates used in reconstructing above meson candidates were not required to pass the standard quality criteria (discussed in next section). Other intermediate meson candidates were formed by simply adding the 4-momenta of daughter particles by making sure that none of the constituent

tracks or showers have been used more than once in the decay chain. Candidate $\eta \to \pi^+\pi^-\pi^0$ and $\eta \to \pi^0\pi^0\pi^0$ decays (collectively referred to as $\eta \to 3\pi$ from now on) were required to have a reconstructed invariant mass of 400–700 MeV/c^2. No invariant mass cut was imposed on the η' candidate. To complete the decay chain, a hard photon was added and the energy of the reconstructed event was compared to the center-of-mass energy. The event was selected if $|\Delta E|$ the magnitude of difference between the energy of reconstructed event and the center-of-mass energy was less than 2.5 GeV. Data skim for mode $\Upsilon(1S) \to \gamma\eta'$; $\eta' \to \gamma\rho$ was made by requiring an event to have a pair of oppositely charged good tracks accompanied by a hard photon.

Since most of the reconstructed energy is measured in CsI, $|\Delta E|$ criterion had been kept generous in anticipation of shower energy leakage. The kinematic fitting we will use in the final analysis will allow effectively tighter cuts on $|\Delta E|$ and p, the magnitude of net momentum vector.

3.3 Reconstruction

In our refined version of reconstructing the decay chain, our track selection criteria remained the same, the "good track" as explained in Section 3.2. To reject the background from spurious photons on the other hand, we used some photon selection criteria. Before we list the photon selection criteria used in reconstructing π^0 and $\eta \to \gamma\gamma$ candidates, we introduce the term E9OVERE25.

E9OVERE25. E9OVERE25 is a selection criterion used to decide whether the shower has a lateral profile consistent with being a photon. The decision is made based upon the energy deposited by the shower in inner 3x3 block of nine CC crystals around the highest energy crystal and the energy deposited in 5x5 block of 25 crystals around the highest energy crystal. The energy deposited in inner 9 crystals divided by the energy deposited in 25 crystals is commonly called E9OVERE25. A true photon is expected to deposit almost all of its energy in the inner 3x3 block. This ratio is

then expected to be equal to one for true photons. For isolated photons, this criterion is highly efficient. However, to maintain high efficiency for photons lying in proximity to each other, a modified version, called E9OVERE25Unf(olded), where the energy in the overlapping crystals is shared.

The photon candidates used in reconstructing candidates $\eta \to \gamma\gamma$ and π^0 had to satisfy the following quality criteria:

- At least one of the showers must have lateral profile consistent with being a photon, which is achieved by 99% efficienct E9OVERE25Unf cut.
- None of the showers could be associated to shower fragments from the interaction of charged tracks in the CC. Since the π^0 and η mesons are the decay daughters of highly energetic η and η' mesons, the decay daughters fly off in a collimated jet and some efficiency loss is expected due to this requirement. However, this cut is necessary to reduce the background from false showers.
- eMin, the minimum shower energy be 30 MeV for π^0 candidates and 50 MeV for η candidates.

Further, the default requirement for π^0 and $\eta \to \gamma\gamma$ candidates, that the constituent showers should be reconstructed either in the fiducial barrel or the fiducial endcap calorimeter region was relaxed[1] for π^0 candidates (see Section 3.3.2). It may be noteworthy that this requirement was also relaxed during the data skimming process.

In order to get the maximum information out of the detector, for those decay modes involving charged tracks, an event vertex was calculated using the charged tracks, and the 4-momenta of the photons were calculated using this event vertex as the origin. The algorithm for event vertex is discussed in Appendix 5. The π^0 and

[1] The fiducial regions of the barrel and endcap are defined by $|\cos(\theta)| < 0.78$ and $0.85 < |\cos(\theta)| < 0.95$, respectively; the region between the barrel fiducial region and the endcap fiducial region is not used due to its relatively poor resolution. For this study, we relaxed this requirement (which we call fiducial region cut) for π^0 candidates as there is a significant chance that at least one of the six photons from the $\eta \to \pi^0\pi^0\pi^0$ decay may be detected in the non-fiducial regions.

intermediate η states were mass constrained using these recalculated photons[2] to their nominal masses. This produces an improvement in the resolution ($\approx 10\%$) of the candidate η and η' invariant mass (see Appendix 5). This corresponds to a slight improvement in the sensitivity of the measurement.

Our general analysis strategy is to reconstruct the complete decay chain to build the $\Upsilon(1S)$ candidate, ensuring that none of the constituent tracks or showers have been used more than once, and kinematically constrain the intermediate π^0 and η meson candidates to their nominal masses [14]. The mode $\Upsilon(1S) \to \gamma\eta; \eta \to \gamma\gamma$ was an exception where no mass constraining was done to the $\eta \to \gamma\gamma$ candidate. The candidate $\eta \to \pi^+\pi^-\pi^0$ was built by first constraining a pair of oppositely charged good tracks to originate from a common vertex. Then, a π^0 candidate was added to complete the reconstruction of $\eta \to \pi^+\pi^-\pi^0$ chain. The candidate $\eta \to \pi^0\pi^0\pi^0$ was reconstructed by simply adding the four momenta of three different π^0 candidates, making sure that no constituent photon candidate contributed more than once in the reconstruction. The reconstruction of $\eta' \to \eta\pi^+\pi^-$ where η decays to all neutrals ($\gamma\gamma$ or $3\pi^0$) is similar to $\eta \to \pi^+\pi^-\pi^0$ candidate reconstruction where we first vertexed a pair of oppositely charged good tracks and then added the η candidate constrained to its nominal mass. In the reconstruction of $\eta'; \eta \to \pi^+\pi^-\pi^0$, the η candidate had position information, so we constrained all three, the pair of oppositely charged good tracks and the mass-constrained $\eta \to \pi^+\pi^-\pi^0$ candidate, to originate from a common vertex. Once the final state η or η' candidates were reconstructed, we added a hard photon to build the $\Upsilon(1S)$ candidate. The reconstruction of $\Upsilon(1S) \to \gamma\eta'$; $\eta' \to \gamma\rho$ was slightly different and is not discussed in this section.

[2] Only in the absence of event vertex, π^0 and η candidates are used as provided by the standard CLEO III software called `PhotonDecaysProd` producer.

The Υ candidate was further constrained to the four momentum of the e^+e^- system. The idea behind 4-constraint is two fold: firstly, substituting the traditional $|\Delta\mathrm{E}|$, p cuts used towards judging the *completeness* of event by a single more powerful quantity, the χ^2_{P4} which is capable of taking the correlation $|\Delta\mathrm{E}|$ and p and secondly, χ^2_{P4}, along with other handles will be exploited in discarding the multiple counting leading to combinatoric background, a problem of varied severity from mode to mode. We took into account the crossing angle of the beams when performing 4-momentum constraint and calculating χ^2_{P4}. Multiply reconstructed Υ candidates in one event give an artificially higher reconstruction yield, and also increase the overall width of the signal. The problem of multiple counting is dealt with by selecting the combination with lowest χ^2_{Total}, the sum of chi-squared of the 4-momentum constraint (χ^2_{P4}) and chi-squared values of all the mass-constraints involved in a particular decay chain. For example, there are four mass-constraints involved in the decay chain $\Upsilon(1\mathrm{S}) \to \gamma\eta'; \eta \to \pi^0\pi^0\pi^0$, three π^0 mass-constraints and one η mass-constraint. The mode $\Upsilon(1\mathrm{S}) \to \gamma\eta; \eta \to \pi^0\pi^0\pi^0$ is an exception in which we preferred to accept the $\eta \to \pi^0\pi^0\pi^0$ candidate having the lowest $S^2_\pi \equiv \sum_i^3 S^2_{\pi,i}$, with $S_{\pi,i} \equiv ((m_{\gamma\gamma} - m_{\pi^0})/\sigma_{\gamma\gamma})$ of the ith π^0 candidate. The quantity $\sigma_{\gamma\gamma}$ is the momentum dependent invariant mass resolution of π^0 candidate. To estimate the reconstruction efficiency, we counted the η' or η candidates contributing towards reconstructing an Υ candidate[3] within our acceptance mass window defined as the invariant mass region centered around the mean value and providing 98% signal coverage as determined from signal Monte Carlo. In addition, the event was required to pass trigger and event-type cuts as listed in Tables 3–2 and 3–3. The method outlined above was common to all modes. Mode specific details are explained below.

[3] An alternative scheme is to count the number of Υ candidates reconstructed from good η or η' candidates.

3.3.1 Reconstruction of $\Upsilon(1\mathbf{S}) \to \gamma\eta; \eta \to \pi^+\pi^-\pi^0$

Although multiple counting was not a severe problem for this mode as there are only two tracks and two photons (in principle at least) on the other side of the hard photon, we still had some events in which there were more than one reconstructed $\Upsilon(1\mathrm{S})$ candidates. The $\Upsilon(1\mathrm{S})$ candidate with the lowest value of $(\chi^2_{\mathrm{P4}} + \chi^2_{\pi^0})$ was selected. Candidate π^0 mesons within 7 $\sigma_{\gamma\gamma}$ (i.e., a very loose cut) were used in reconstructing the $\eta \to \pi^+\pi^-\pi^0$ candidate. A fairly loose particle identification criterion using dE/dx information was employed by requiring the charged tracks to be consistent with being pions. We added the pion hypothesis $\mathrm{S}_{dE/dx}$ in quadrature for two tracks ($\mathrm{S}^2_{dE/dx} \equiv \sum_{i=1}^{2} \mathrm{S}^2_{dE/dx}(i)$), where $\mathrm{S}_{dE/dx}$ for the ith track is defined as $\mathrm{S}_{dE/dx}(i) = (dE/dx(\mathrm{measured}) - dE/dx(\mathrm{expected}))/\sigma_{dE/dx}$ and $\sigma_{dE/dx}$ is the dE/dx resolution for pion hypothesis. We then required $\mathrm{S}^2_{dE/dx}$ to be less than 16. Finally, to judge the completeness of the event, a cut of $\chi^2_{\mathrm{P4}} < 100$ was applied. The efficiencies of these cuts are listed in Table 3–4.

Table 3–4. Efficiency of selection criteria for the mode $\Upsilon(1\mathrm{S}) \to \gamma\eta; \eta \to \pi^+\pi^-\pi^0$

Cut	Ind Eff (%)	Cmb Eff (%)
π^0 reconstruction	38.2	34.6
$\sigma_{\gamma\gamma} < 7$	96.5	34.7
$\mathrm{S}^2_{dE/dx} < 16$	100.0	34.7
$\chi^2_{\mathrm{P4}} < 100$	93.4	32.8
all cuts	32.8 ± 0.4	

The invariant mass distribution for the $\eta \to \pi^+\pi^-\pi^0$ candidate from signal MC after all the cuts is shown in Figure 3–1. Figure 3–2 shows the distribution for various variable we cut on. With this highly efficient reconstruction scheme, we found no event within our invariant mass acceptance window (Figures 3–3(d), 3–4). In Figure 3–3(d), it does appear that dE/dx cut rejects a lot of (background) events. We notice that the rejected background is mostly electrons (see Figure 3–5), which can alternatively be rejected using *eop* (the energy deposited in the CsI by a track divided

by its measured momentum) cut. However, using $S^2_{dE/dx}$ as a selection criterion gave us better background rejection compared to *eop* cut, with basically the same efficiency. The efficiency for $S^2_{dE/dx}$ cut was checked using the ω peak (from the continuum process $e^+e^- \rightarrow \gamma\omega$) by plotting the sideband subtracted signal and was found to be $\approx 96\%$, which is lower than the signal MC prediction of 99.9%. We believe the discrepancy is largely accounted for by the fact that background to the ω peak ramps up under the peak, rather than imperfections of the detector response simulation. Thus we will continue to use the 99.9% number as our efficiency, but will give it a suitable systematic uncertainty. The high efficiency and good background rejection of this cut is because the π and e dE/dx lines are well separated in the momentum range of interest.

Likelihood = 128.3

χ^2= 117.5 for 100 - 8 d.o.f., C.L.= 3.8%

Errors		Parabolic	Minos	
Function 1: Two Gaussians (sigma)				
AREA	8201.0	± 93.94	- 0.0000E+00	+ 0.0000E+00
MEAN	0.54727	± 6.9177E-05	- 7.1628E-05	+ 0.0000E+00
SIGMA1	1.16237E-02	± 4.1875E-04	- 3.7866E-04	+ 0.0000E+00
AR2/AREA	0.64843	± 2.3090E-02	- 0.0000E+00	+ 0.0000E+00
* DELM	0.00000E+00	± 0.0000E+00	- 0.0000E+00	+ 0.0000E+00
SIG2/SIG1	0.37259	± 1.0042E-02	- 0.0000E+00	+ 1.0187E-02
Function 2: Chebyshev Polynomial of Order 2				
NORM	1452.9	± 148.8	- 0.0000E+00	+ 0.0000E+00
CHEB01	0.21470	± 0.1355	- 0.0000E+00	+ 0.0000E+00
CHEB02	-0.82008	± 1.7189E-05	- 0.0000E+00	+ 0.0000E+00

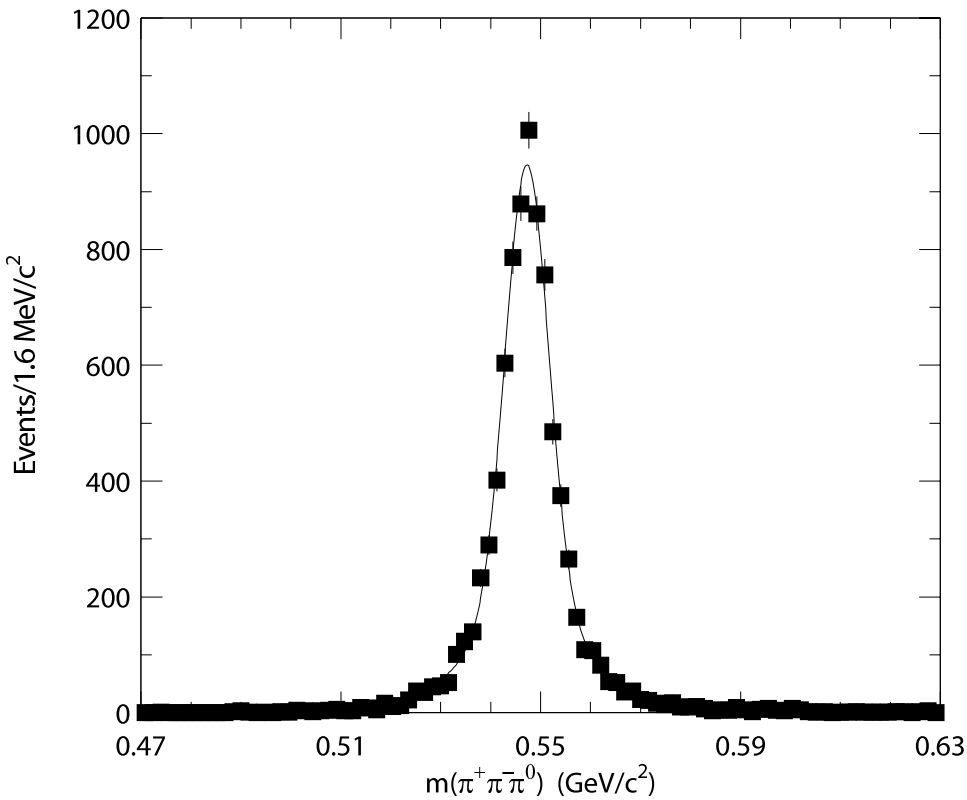

Figure 3–1. Candidate $\eta \to \pi^+\pi^-\pi^0$ reconstructed invariant mass distribution from signal Monte Carlo for the mode $\Upsilon(1S) \to \gamma\eta; \eta \to \pi^+\pi^-\pi^0$. The reconstruction efficiency is $32.8 \pm 0.4\%$ after all the cuts.

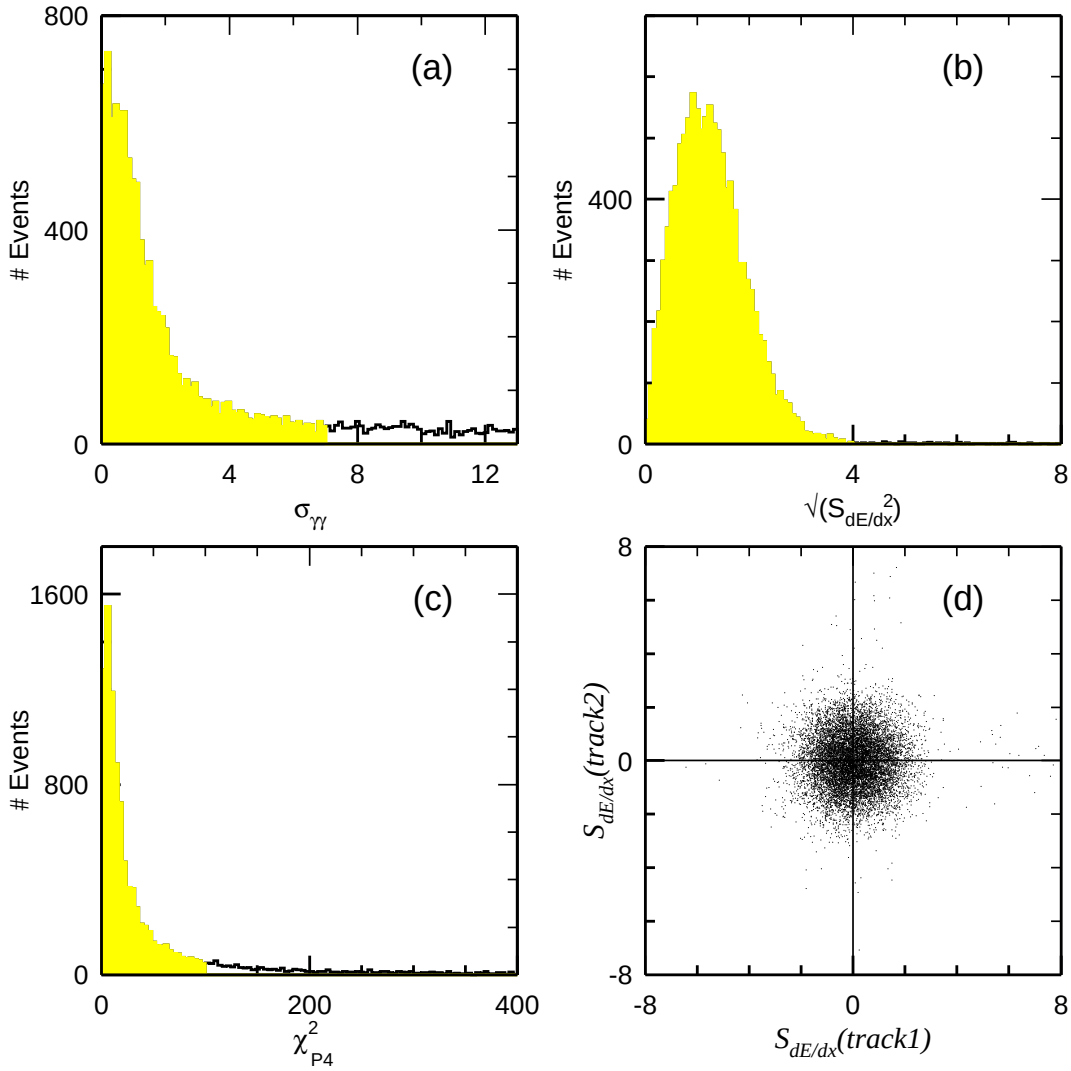

Figure 3–2. Distribution from signal Monte Carlo: For the mode $\Upsilon(1S) \to \gamma\eta; \eta \to \pi^+\pi^-\pi^0$, variables we cut on are plotted. The yellow (shaded) area in these plots represents the acceptance. Plot(a) $\sigma_{\gamma\gamma}$ of the π^0 candidate, plot(b) for $\sqrt{\mathrm{S}^2_{dE/dx}}$, plot(c) for χ^2_{P4}, and plot(d) is a scatter plot of the pion hypothesis $\mathrm{S}_{dE/dx}$ for the charged tracks.

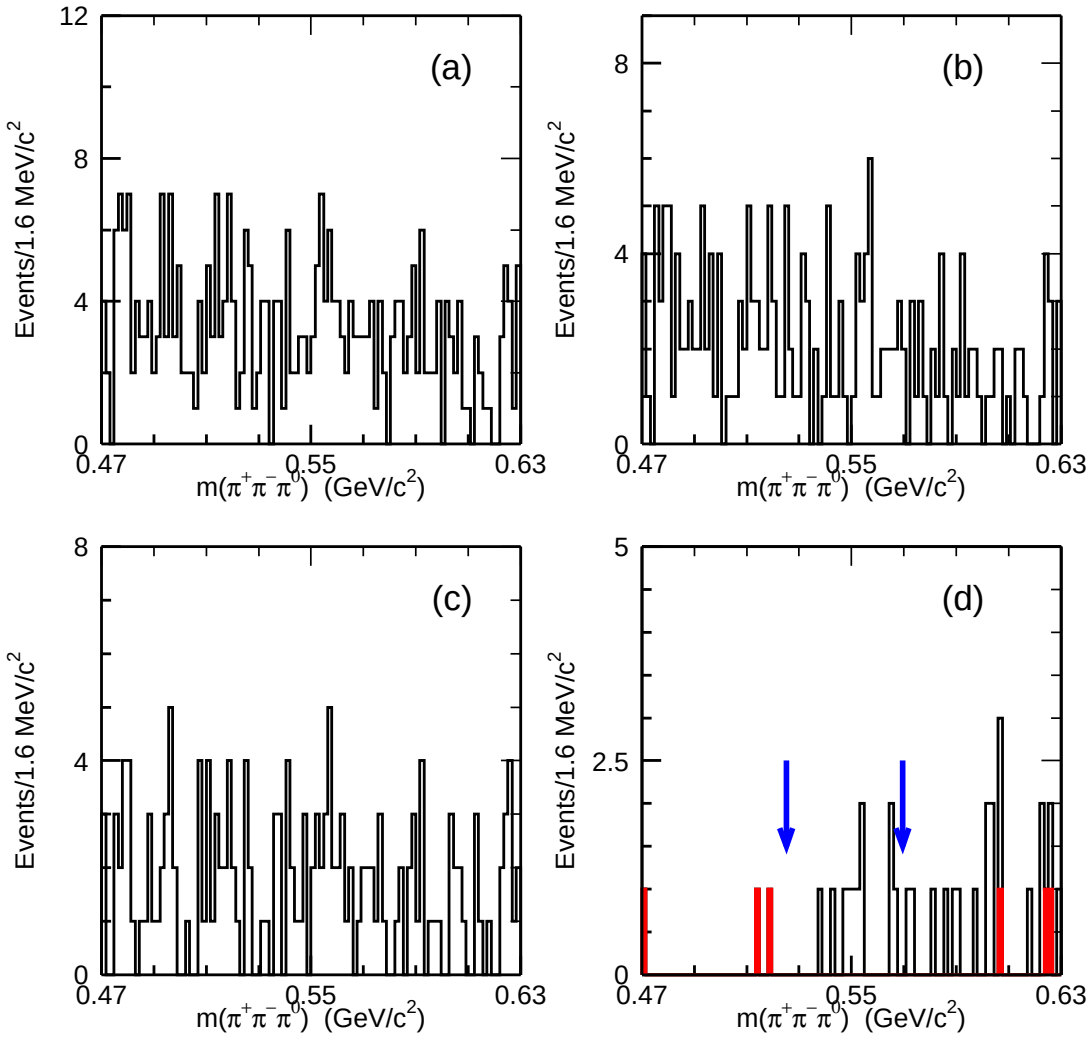

Figure 3–3. Invariant mass of distribution of the η candidate for the mode $\Upsilon(1S) \to \gamma\eta; \eta \to \pi^+\pi^-\pi^0$: Plot(a) with no cuts, plot(b) with a cut on χ^2_{P4} only, plot(c) after cutting on $\sigma_{\gamma\gamma}$ of the π^0 candidate only, plot(d) after cutting on $S^2_{dE/dx}$ alone. The red overlay on plot(d) is obtained after imposing all the cuts. No candidate event was observed in signal region.

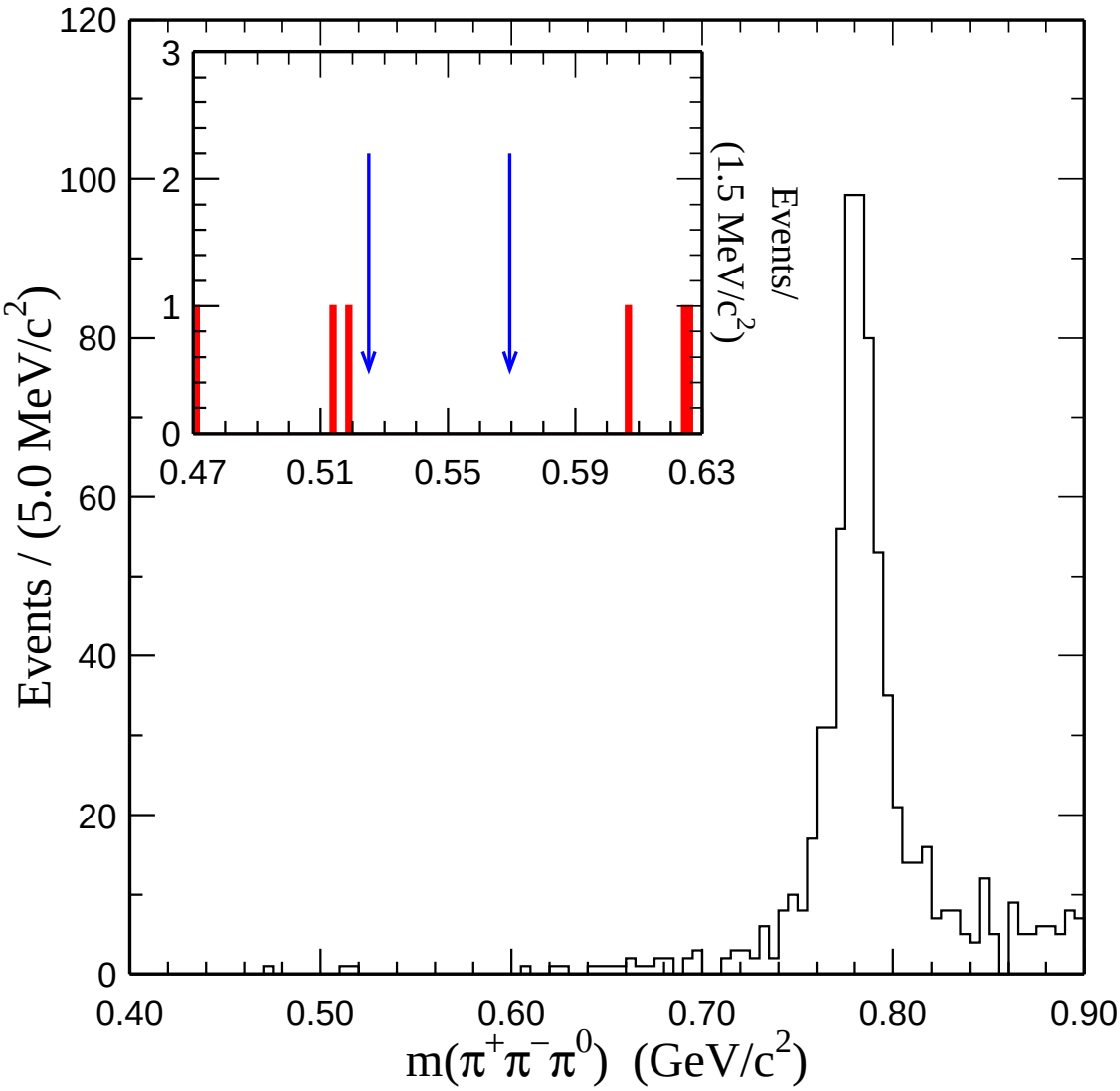

Figure 3–4. Reconstructed η candidate invariant mass distribution in real data for the mode $\Upsilon(1S) \to \gamma\eta; \eta \to \pi^+\pi^-\pi^0$. No events are observed in the signal mass window denoted by the region in between blue arrows (inset), and a clear $\omega \to \pi^+\pi^-\pi^0$ peak is visible from the QED process $e^+e^- \to \gamma\omega$.

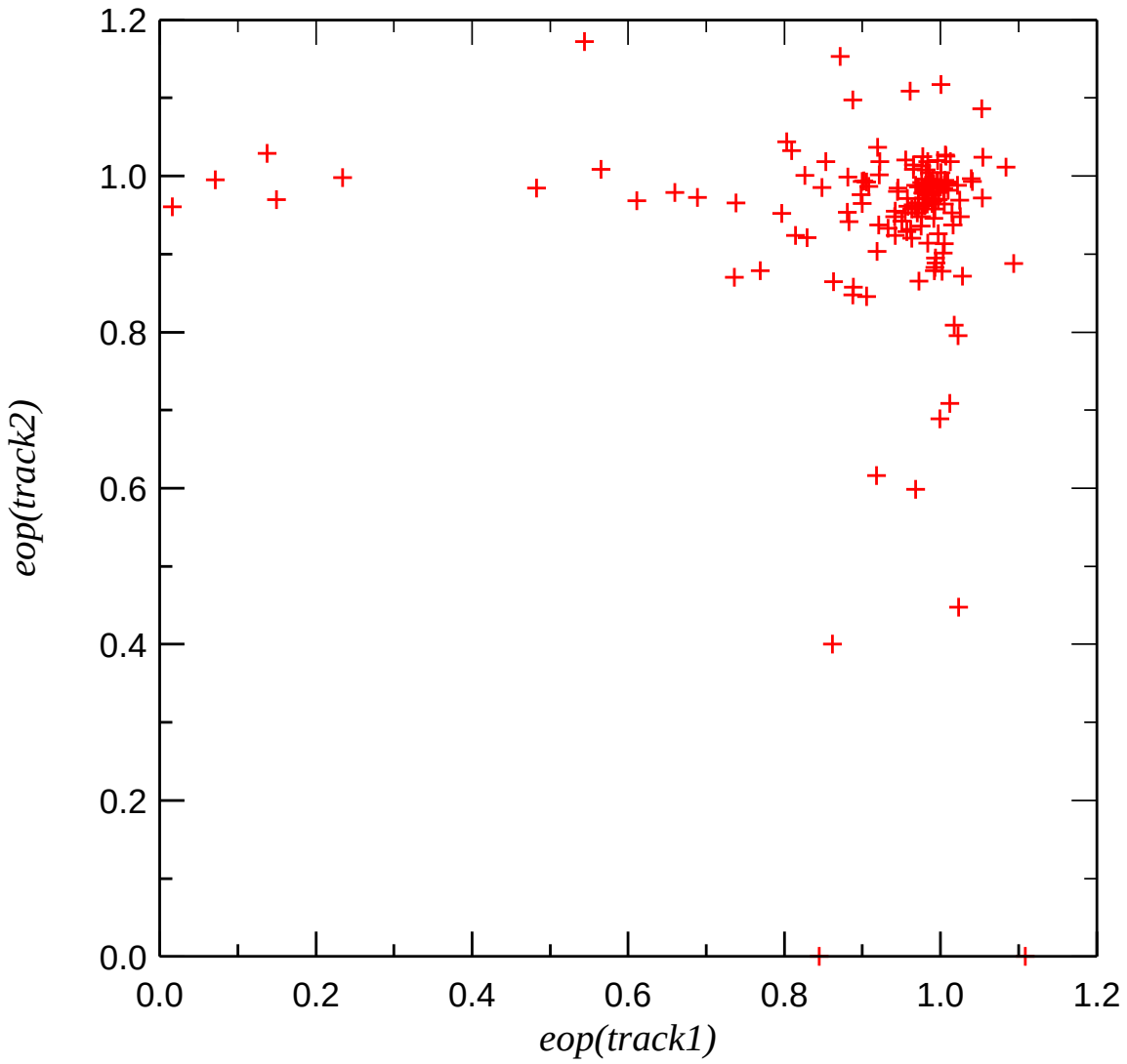

Figure 3–5. Scatter plot of *eop* distribution for track 2 vs track 1 for the events rejected by $S^2_{dE/dx} > 16.0$ cut. Most of the rejected events are clearly electron like.

3.3.2 Reconstruction of $\Upsilon(1\mathbf{S}) \to \gamma\eta; \eta \to \pi^0\pi^0\pi^0$

The kinematics involved in this decay mode are largely responsible for a comparatively low efficiency and reconstruction quality. The decay of high energy η into three π^0 mesons does not cause them to spread out a lot, as a result the showers from different π^0 mesons frequently lie on top of each other. Just one overlap of two showers often makes it impossible to reconstruct two of the π^0 mesons. By seeking the help of *tagger*[4] , we figure that more than 50% of the events suffer from this pathology. In total MC this leaves us with only $\approx 22.7\%$ (5675 out of 25000) events where the showers from the η have **proper tags** . We define an MC η having **proper tag** when all six photons from η decay are tagged to six different reconstructed showers. Roughly 20% of the events with **proper tags** were filtered out by the fiducial region cut (discussed in Section 3.3) alone, which is why this cut was relaxed so that a more reasonable reconstruction efficiency could be obtained.

To address the problem of multiple counting, we select the Υ(1S) candidate in the event having the lowest S_π^2 (defined in Section 3.3). From now on, we will refer to such a candidate as the *best candidate*. Using tagged Monte Carlo, we find that we pick up the correct combination (i.e., each of the three π^0 candidates is reconstructed from the photons candidates which have been tagged to the actual generated ones) approximately 72% of the time[5] .

Having selected the *best* $\Upsilon(1S)$ *candidate*, we require the following two selection criteria to be satisfied:

---

[4] The tagger is a software part of the CLEO III software library. The tagger is capable of performing hit-level tagging, and therefore, can tell us which reconstructed track or shower is due to which generated charged particle or photon. By hit-level tagging it is understood that the tagging software keeps track of the cause of simulated hits (i.e., which hit is from which track, etc.), and so it is very reliable.

[5] An alternative scheme based upon χ^2_{Total} gives statistically same answer, though any two schemes may disagree on an event by event basis.

- $\sqrt{S_\pi^2} < 10.0$. primarily to select good quality π^0 candidates and reduce possible background in real data.

- $\chi^2_{\mathrm{P4}} < 200.0$ to ensure that the reconstructed event conserves the 4-momentum.

In addition, we notice that requiring the number of reconstructed showers in event to be ≤ 13 is 99.9% efficient in signal MC and helps us reduce some background. The reason that this cut is useful is that one source of background is the process $e^+e^- \to \gamma\phi$ where $\phi \to K_S K_L$. The decays chain ends with $K_S \to \pi^0\pi^0$ and a possible $K_L \to \pi^0\pi^0\pi^0$, giving rise to an event with a hard photon along with at least 2 π^0 mesons with some extra showers. Even if the K_L does not decay within the volume of the detector, its interaction in the CC is not well understood and it can possibly leave a bunch of showers. Such a background can easily be rejected by a requirement on the number of showers. From respective Monte Carlo samples, the shower multiplicity for processes $\Upsilon(1\mathrm{S}) \to \gamma\eta; \eta \to \pi^0\pi^0\pi^0$ and $e^+e^- \to \gamma\phi$ is shown in Figures 3–7 (c) and (d) respectively. As per the Monte Carlo, roughly 50% of the type $e^+e^- \to \gamma\phi$ are rejected by the cut restricting number of showers to be ≤ 13 whereas only this requirement is almost 100% efficient in signal MC. Thus, we require the reconstructed event to pass this highly efficient test as well. Table 3–5 lists the selection criteria used in the reconstruction. Figure 3–6 shows the invariant mass distribution from signal MC for the mode $\Upsilon(1\mathrm{S}) \to \gamma\eta; \eta \to \pi^0\pi^0\pi^0$. Figure 3–7 shows the distribution of the quantities we cut on. With this reconstruction scheme, we find no candidate events from real 1S data as the Figure 3–8 shows.

Table 3–5. Efficiency table for the mode $\Upsilon(1\mathrm{S}) \to \gamma\eta; \eta \to \pi^0\pi^0\pi^0$.

Cut	Ind Eff (%)	Cmb Eff (%)
$\sqrt{S_\pi^2}$ of $\pi^0 s < 10$	94.9	12.3
$\chi^2_{\mathrm{P4}} < 200$	95.4	11.8
# Showers ≤ 13	99.9	11.8
all cuts	11.8 ± 0.2	

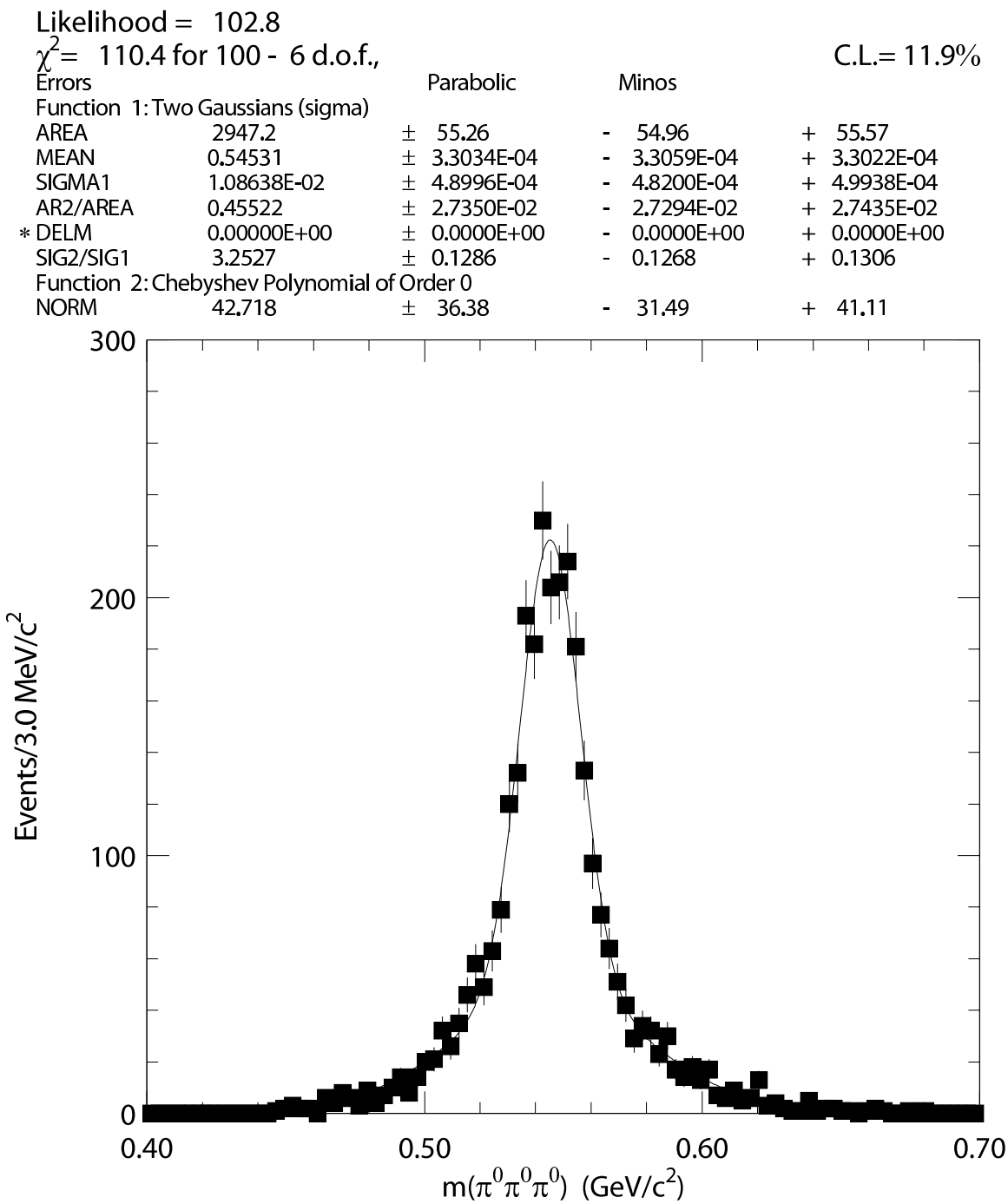

Figure 3–6. Reconstructed invariant mass distribution for the candidate $\eta \to \pi^0\pi^0\pi^0$ from signal Monte Carlo for the mode $\Upsilon(1S) \to \gamma\eta; \eta \to \pi^0\pi^0\pi^0$. The reconstruction efficiency is $11.8 \pm 0.2\%$ after all the cuts.

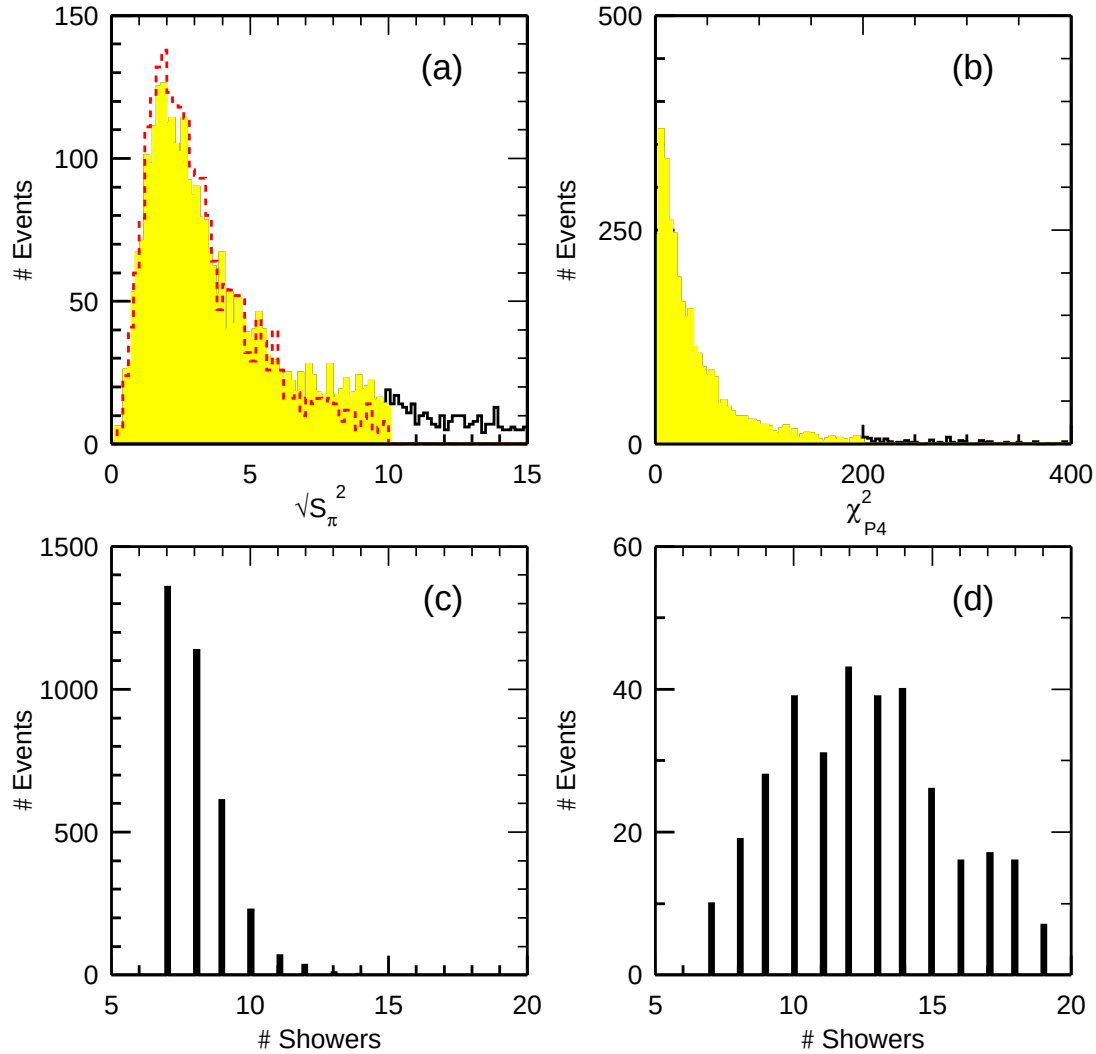

Figure 3–7. Distributions from $\Upsilon(1S) \to \gamma\eta; \eta \to \pi^0\pi^0\pi^0$ signal Monte Carlo, showing the variables we cut on. The yellow (shaded) area in these plots represents the acceptance. Plot (a) $\sqrt{S_\pi^2}$ of the π^0 candidates, plot (b) for χ^2_{P4}, and plot (c) # of showers in the event. The dashed (red) line in plot (a) shows the $\sqrt{S_\pi^2}$ of the tagged π^0 candidates. As can be seen, majority of good events are confined within $\sqrt{S_\pi^2} < 10.0$, giving us a reason to select our acceptance region. Plot (d) shows the shower multiplicity from the signal MC for the process $e^+e^- \to \gamma\phi$. Although plot (d) is not normalized to plot (c), we can clearly see that if Monte Carlo be trusted, a cut on the number of showers help reject $\sim 50\%$ of this background.

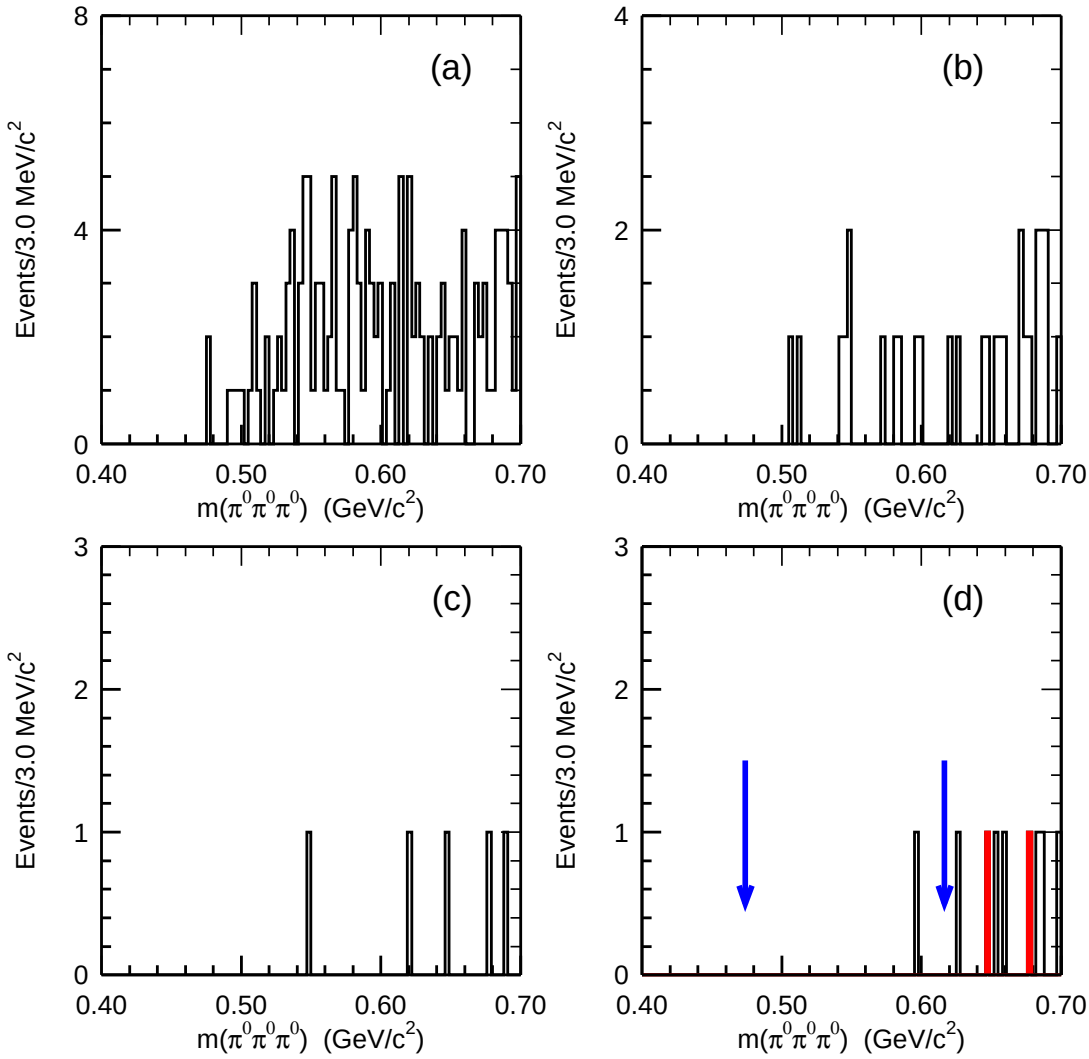

Figure 3–8. Invariant mass of η candidate for the mode $\Upsilon(1S) \to \gamma\eta; \eta \to \pi^0\pi^0\pi^0$: Plot (a) allowing multiple candidates per event, plot (b) after selecting *best candidate*, plot (c) selecting *best candidates* with $\chi^2_{P4} < 200.0$, plot (d) *best candidate* with # of showers cut. The red overlay on plot (d) is obtained after imposing all the cuts. There are no events in the acceptance mass window (denoted by blue arrows) after all the cuts.

3.3.3 Reconstruction of $\Upsilon(1\mathbf{S}) \to \gamma\eta; \eta \to \gamma\gamma$

We first form all possible $\gamma\gamma$ combinations to build η candidate. Then, the $\Upsilon(1S)$ candidate is reconstructed by combining a hard photon to the η candidate, which is kinematically constrained to the 4-momentum of e^+e^- system. We accept an $\Upsilon(1S)$ candidate if $\chi^2_{P4} < 200.0$. We do not attempt to reject events with more than one $\Upsilon(1S)$ candidate as only the right combination enters our final η candidate invariant mass plot.

Our selection criteria so far, namely using a hard photon and constraining the $\Upsilon(1S)$ candidate to the 4-momentum of beam, are not sufficient to suppress the QED background from the process $e^+e^- \to \gamma\gamma\gamma$ (See Figure 3–9). The QED MC was generated using Berends-Kliess generator[22].

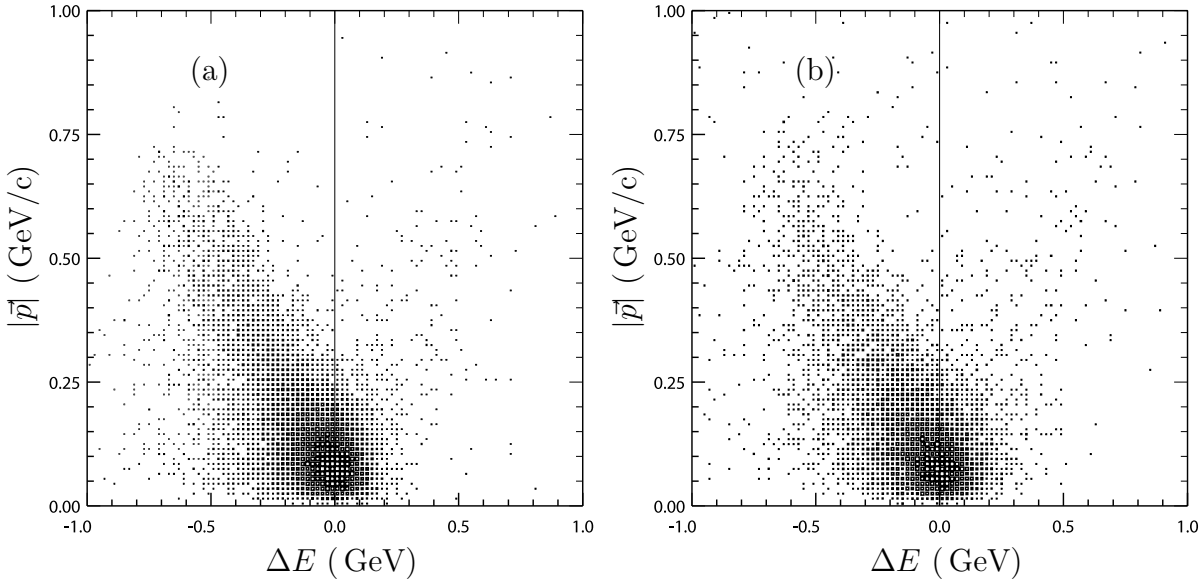

Figure 3–9. $|\vec{p}|$ vs ΔE distribution plot(a) for signal MC for $\Upsilon(1S) \to \gamma\eta; \eta \to \gamma\gamma$ and plot(b) for $e^+e^- \to \gamma\gamma\gamma$ MC.

The QED events, however, have very asymmetric distribution of energy E_{hi} and E_{lo} for two lower energy photons used in reconstructing η. The real η has equal probability of having the decay *asymmetry* from 0 to 1 (Figure 3–10) where *asymmetry*

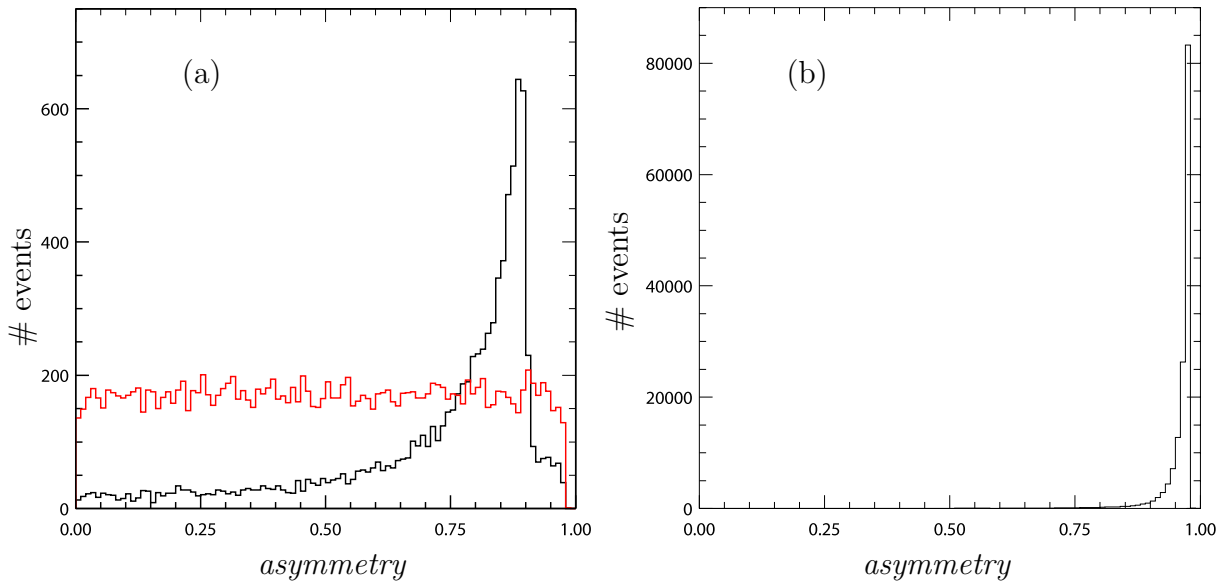

Figure 3–10. *Asymmetry* distribution for η candidate. Plot (a) from Monte Carlo data for $e^+e^- \to \gamma\gamma\gamma$ (black) and signal MC $\Upsilon(1S) \to \gamma\eta; \eta \to \gamma\gamma$ (red) and plot (b) for data18 and data19. For *asymmetry* < 0.75, the events in plot (b) are overshadowed by the events beyond *asymmetry* > 0.75. The huge pile at the higher in end in plot (b) is because in this plot, the events classified as gamGam event-type have not been rejected yet.

is defined as $(E_{hi} - E_{lo})/(E_{hi} + E_{lo})$. We note the signal MC prediction that majority of the signal events are classified as either radGam or gamGam event-types. The events classified as gamGam event-type only, however, have very asymmetric decays with *asymmetry*> 0.84. The event-type gamGam is thus automatically ruled out by the *asymmetry* cut, which is applied at 0.8. The expected efficiency for this cut is 80%, in reality it is more than that as the peak[6] *asymmetry* can not be equal to one. Considering the efficiency and the amount of QED suppression achieved, we add this as one of our basic selection criteria. The QED background, however, is not fully suppressed.

[6] *Asymmetry* equal to one means one of the photons has measured energy equal to 0

3.3.3.1 Possible Background $e^+e^- \to \gamma\gamma(\to e^+e^-)$

We make a brief digression to another possible background which was reported in the previous analysis [9]. This background arises from $e^+e^- \to \gamma\gamma$ where one of the photons converts into an e^+e^- pair sufficiently far into the drift chamber that no tracks are reconstructed. This e^+e^- pair separates in ϕ under the influence of magnetic field, and mimics two showers. Such a "$\gamma\gamma\gamma$" event might satisfy our selection criteria. A distinct geometric characteristic of such a shower pair is that $\Delta\theta$, the difference in polar angle θ of two showers, is close to $0°$, whereas $|\Delta\phi|$, the magnitude of difference in azimuthal angle ϕ of two showers, is not. In [9] a *geometric cut* requiring $|\Delta\theta| > 3°$ was used in reducing this background which was otherwise a substantial fraction of the entries in the final $\eta \to \gamma\gamma$ invariant mass distribution.

Motivated by this, we looked for the presence of such background in our analysis. However, we did not find any obvious signature in real data as Figure 3–11 shows. A further investigation was done by generating a dedicated Monte Carlo sample comprising 115K events for the process $e^+e^- \to \gamma\gamma$ without any ISR (initial state radiation) effects. We did not find any background event of this type surviving our cuts in $e^+e^- \to \gamma\gamma$ Monte Carlo sample either.

3.3.3.2 Handling $e^+e^- \to \gamma\gamma\gamma$ background

To study our main QED background process, $e^+e^- \to \gamma\gamma\gamma$, we generated a dedicated MC sample for this process, using a stringent `ISELECT` function (a piece of code primarily meant to accept the events of interest before computing intensive, full detector simulation is carried out) demanding

- Only 3 photons generated, all with $|\cos(\theta)| < 0.95$
- At least one photon with generated energy of at least 4.0 GeV
- Remaining two photons have $\gamma\gamma$ invariant mass in the range 0.2–1.0 GeV/c^2 and *asymmetry* < 0.8

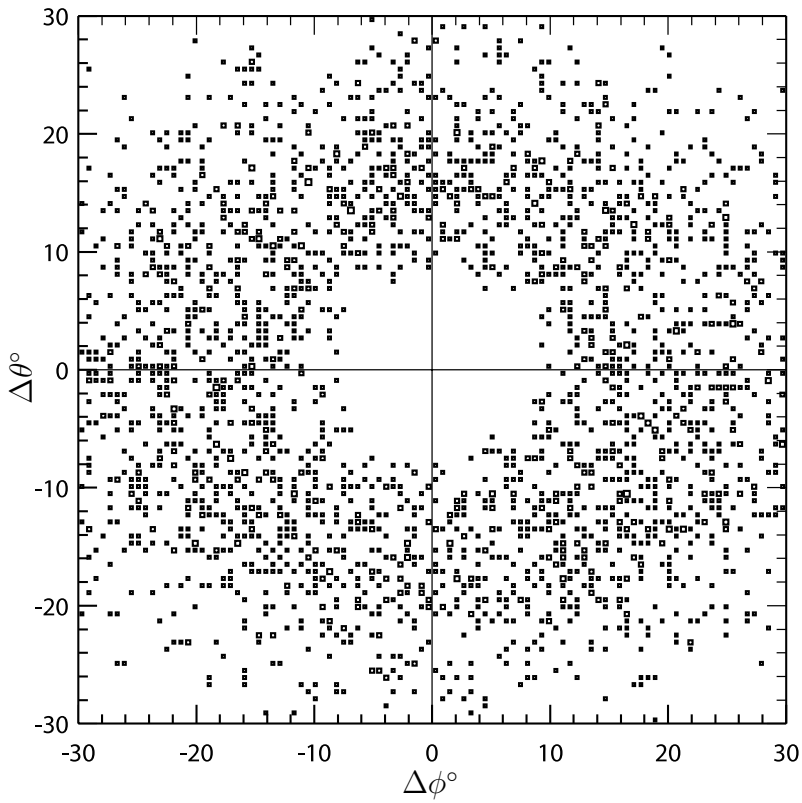

Figure 3–11. Distribution of $\Delta\theta$ vs $\Delta\phi$ in real data for events in the η mass window passing our basic cuts.

We analyze the two MC data samples (signal MC and QED) in detail, but except for *asymmetry* we do not find any distinct feature which can help us help us discriminate between them. There should be, however, some minor differences in distributions of some variables, which may be harnessed collectively to achieve further signal to background separation. Thus we wrote a neural network program in an attempt to combine the information in an optimal way.

Artificial Neural Net. An Artificial Neural Net (ANN) is a mathematical structure inspired from our understanding of biological nervous system and their capability to learn through exposure to external stimuli and to generalize. ANNs have proved their usefulness in diverse areas of science, industry, and business. In the field of experimental high energy physics, ANNs have been exploited in performing trigger operations, pattern recognition and classification of events into different categories,

say signal and background. Generally, the goal is to do a multivariate analysis to carve out a decision surface, a method superior to a series of cuts. ANNs have already made their impact on discovery (top quark).

An ANN consists of *artificial neurons* or *nodes* which exchange information. Each node receives input signal from other nodes, and the weighted sum of these inputs is transformed by an *activation function* $g(x)$, the result of which is the output from the node. This output multiplied by the weight of the node serves as an input to some other node. Without discussing the gory details of the functioning of an ANN, we mention of *feed-forward* neural network where the information flow is in one direction only. The neural network used in this analysis is a multi-layer perceptron [23] which is essentially a *feed-forward* ANN having an input layer accepting a vector of input variables, a few hidden layers and an output layer with single output.

To be able to use a neutral network in solving a problem, it needs to be trained over a set of training *patterns*, which is done iteratively. During the course of training, the weights of individual nodes adapt according to the *patterns* fed to the neural network. The difference between the desired output (1 for signal and -1 background in our case) and the actual output from the neural net is used to modify the weights and the discrepancy (or error) is minimized as the training progresses.

The architecture of the neural net used is [9 14 5], a three layered neural net having $\tanh(x)$ as the *activation function*, with single output in the range [-1,1]. The output from the trained neural net is expected to peak at 1 for signal events and at -1 for background events. The input to the neural net is a vector of six variables, namely the measured energy and polar angle θ of the three showers used in reconstruction. The isotropy in azimuthal angle ϕ renders it powerless in making any discrimination in separating the signal from background. The choice of input vector as well as the training data sample is very important. The general tendency of neural nets is to figure out the easily identifiable differences in the two samples first - invariant mass of

the η candidate being the easy catch between signal MC and QED background here, as with this choice of input vector, the neural net can easily work out the invariant mass of the η candidate. For this reason, we generate a signal MC having a "wide" η and select the data for training where invariant mass of η is in the range 0.4–0.7 GeV/c^2. The background data sample is comprised of the $e^+e^- \to \gamma\gamma\gamma$ Monte Carlo generated at center-of-mass energy 9.46 GeV, having di-photon invariant mass in the range 0.4–0.7 GeV/c^2, a 300 MeV/c^2 window around the nominal η mass. With this sample, the bias due to invariant mass is eliminated. To avoid the well known "over-fitting" problem where the neural-net starts remembering the data too specifically and hence losing its ability to generalize, we build a large training sample of 10,000 events of each type (signal and background). As the training progresses, we monitor (see Figure 3–12) the performance of the neural-net over a similar, independent testing sample comprised of signal and background Monte Carlo data.

3.3.3.3 Final Selection and Comparison of Neural Net vs Asymmetry

Using independent samples of signal and $e^+e^- \to \gamma\gamma\gamma$ Monte Carlo, we compare the performance of neural net cut with *asymmetry* cut. The neural net outperforms the *asymmetry* cut only marginally as is clear from Figure 3–13. For any chosen efficiency, neural net gives a higher background rejection as compared with *asymmetry*. For our final selection, we choose net-value > 0.4 with 51% efficiency while rejecting 86% of the background. To choose the value for this cut, we optimize $S/\sqrt{B}$ which was found to be fairly flat in the range 0.15–0.40 .

The efficiency of the cuts used is listed in Table 3–6. Figure 3–14 shows the signal MC events' $\gamma\gamma$ invariant mass distribution for η candidates surviving our final cuts. The final reconstruction efficiency for this mode is $23.8 \pm 0.3\%$.

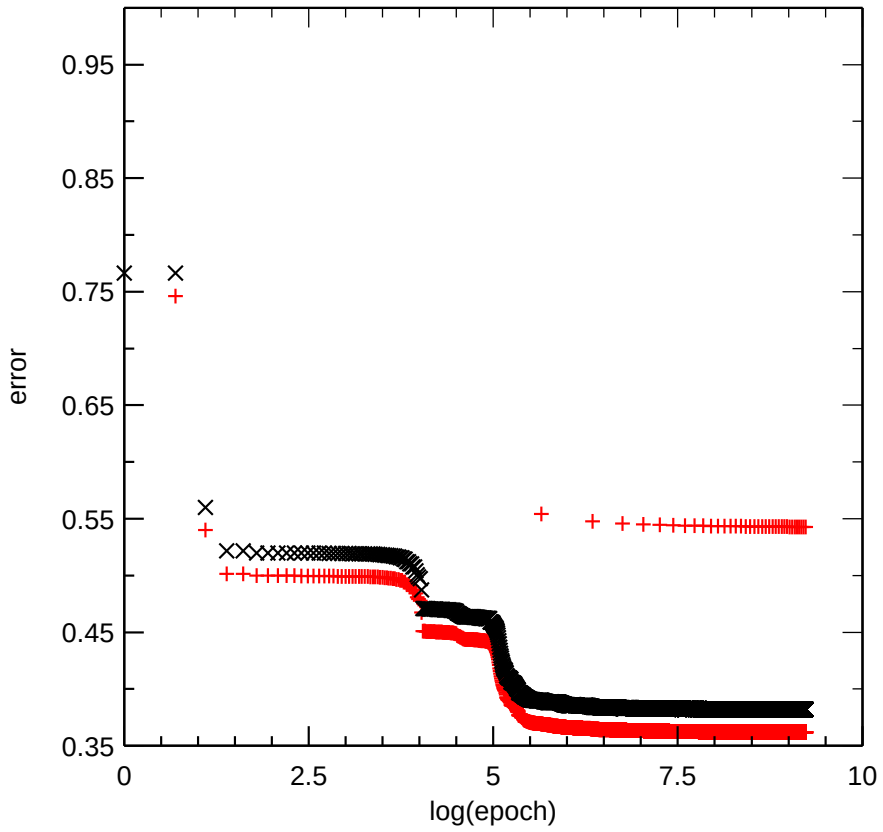

Figure 3–12. Training the Neural Net: During the course of training, red denotes the training error and black denotes the testing error (shifted by 0.02 for clarity) from an independent sample. The testing error follows the training errors closely and over-training is not exhibited at all. The learning process saturates however, and training is stopped after 10K iterations.

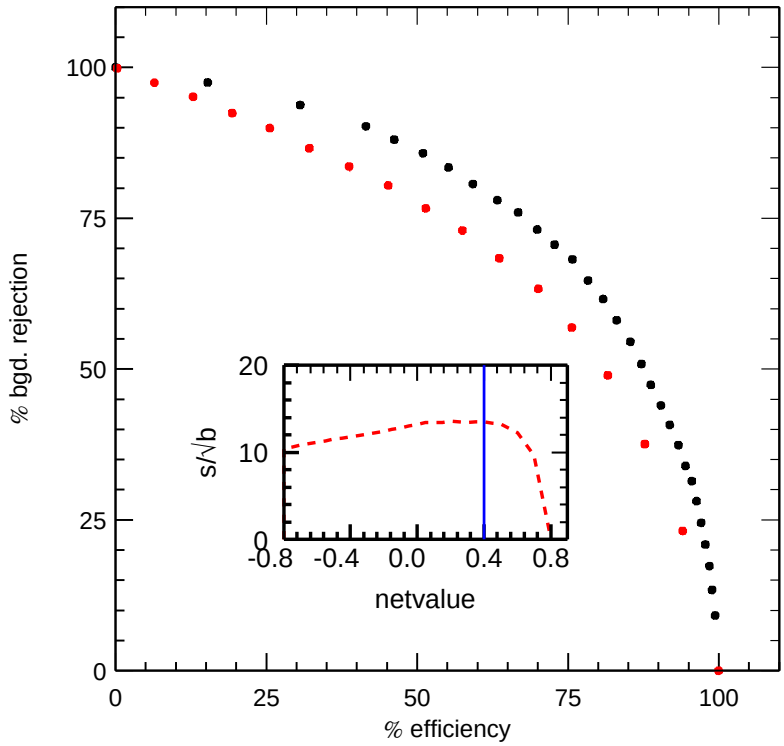

Figure 3–13. Comparison of background rejection vs efficiency: The lower curve in red shows the performance of *asymmetry* cut and upper curve in black is from neural net. For any chosen value of efficiency, neural net gives a higher background rejection as compared to *asymmetry* cut. Inset is $S/\sqrt{B}$ plotted for various values of neural net cut.

Table 3–6. Final efficiency table for the mode $\Upsilon(1S) \to \gamma\eta; \eta \to \gamma\gamma$

Cut	Ind Eff (%)	Cmb Eff (%)
$\chi^2_{\mathrm{P4}} < 2000$	100.0	55.6
asymmetry < 0.8	83.9	46.7
net > 0.4	51.1	23.8
all cuts	23.8 ± 0.3	

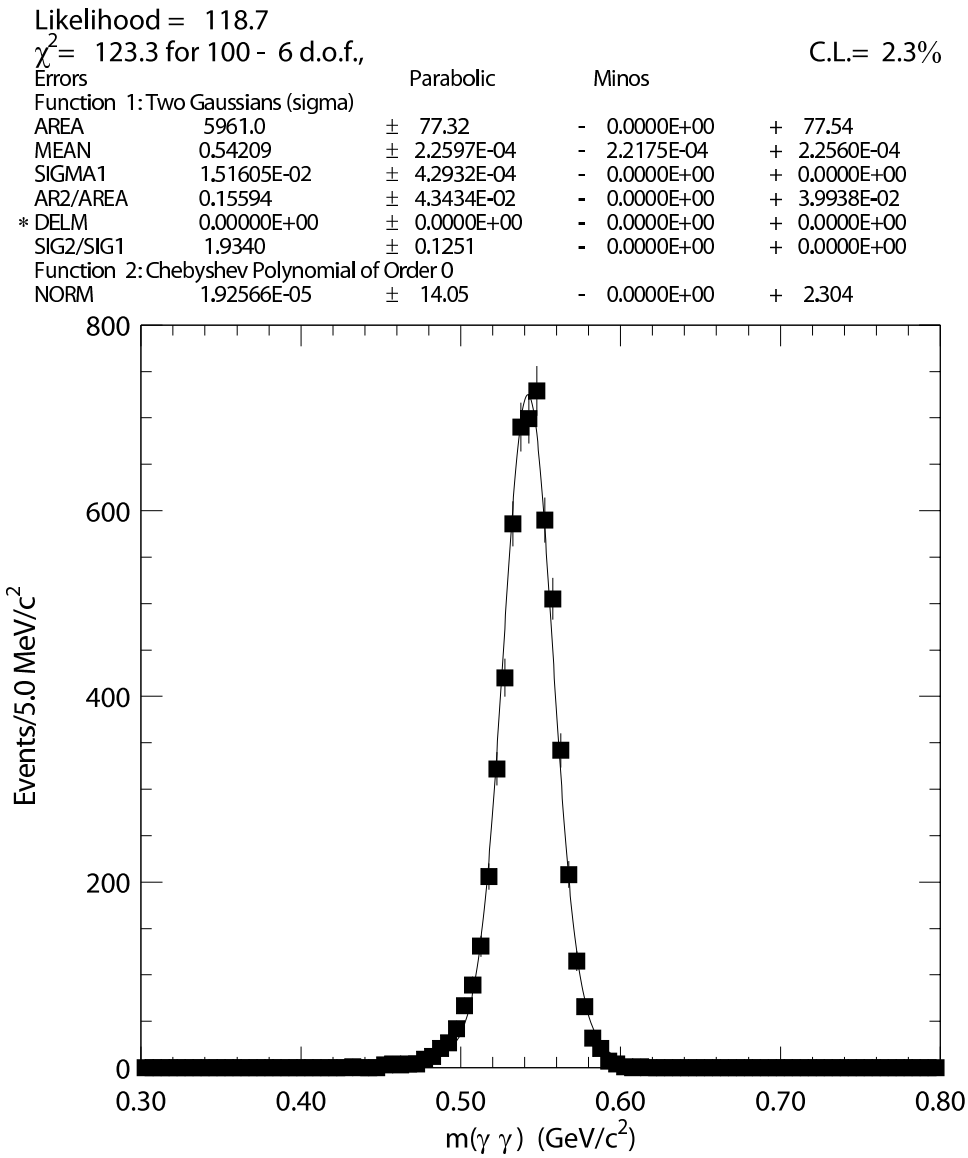

Figure 3–14. $\gamma\gamma$ invariant mass distribution from signal Monte Carlo for the mode $\Upsilon(1S) \to \gamma\eta; \eta \to \gamma\gamma$

3.3.3.4 Data Plots and Upper Limit

Requiring all cuts except the neural net, Figure 3–15 shows the $\gamma\gamma$ invariant mass distribution in real data. After imposing neural net cut as well, the $\gamma\gamma$ invariant mass distribution is shown in Figure 3–16.

We fit the $\gamma\gamma$ invariant mass distribution to a Gaussian of fixed mean and width as obtained from signal MC convoluted with a background function. If we let the

area float, we obtain -2.3 ± 8.7 events (Figure 3–17), consistent with 0. To obtain the upper limit for this mode, we fix the parameters to the ones obtained from Monte Carlo and do likelihood fits for different, fixed signal yields and record the χ^2 of fit. We assign a probability P of obtaining this yield as:

$$P \propto e^{-\frac{\chi^2}{2}},$$

which we normalize to 1.0 and numerically integrate up to 90% of the area to obtain the yield at 90% confidence level as shown in Figure 3–18. Figure 3–19 shows the upper limit area, which is the result of summing up the probability distribution in Figure 3–18 upto 90% .

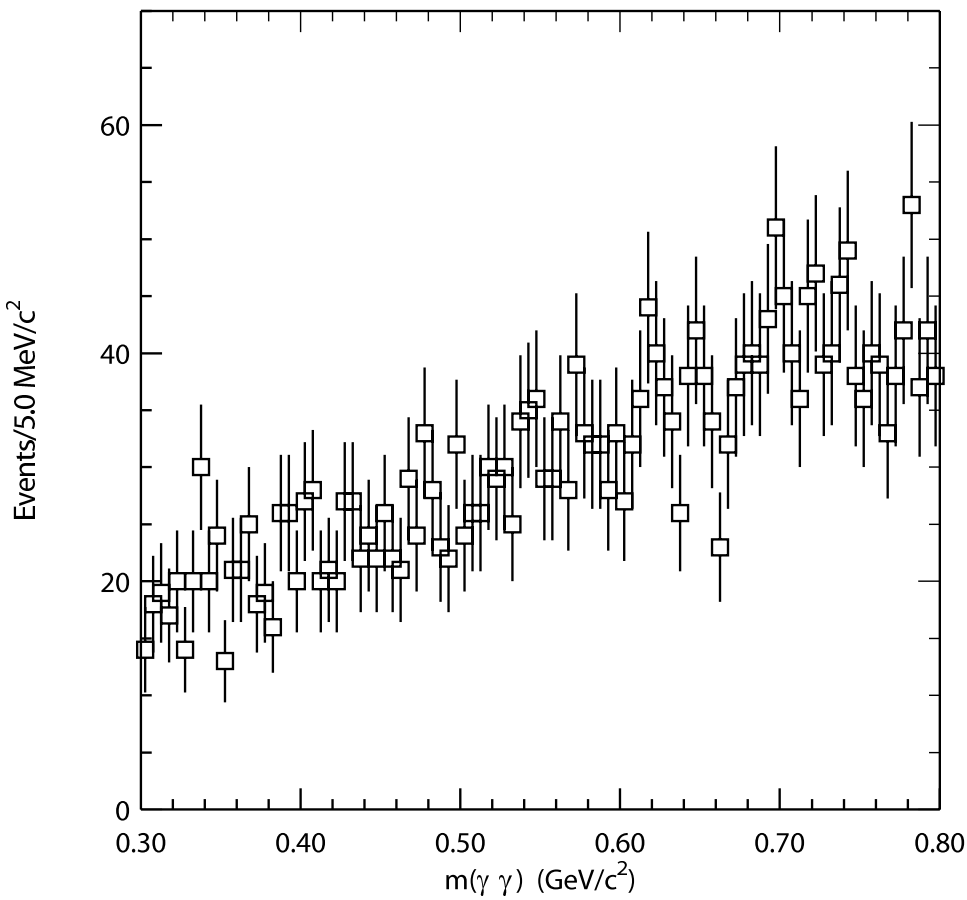

Figure 3–15. $\gamma\gamma$ invariant mass distribution in real data. All cuts except neural net cut are in place.

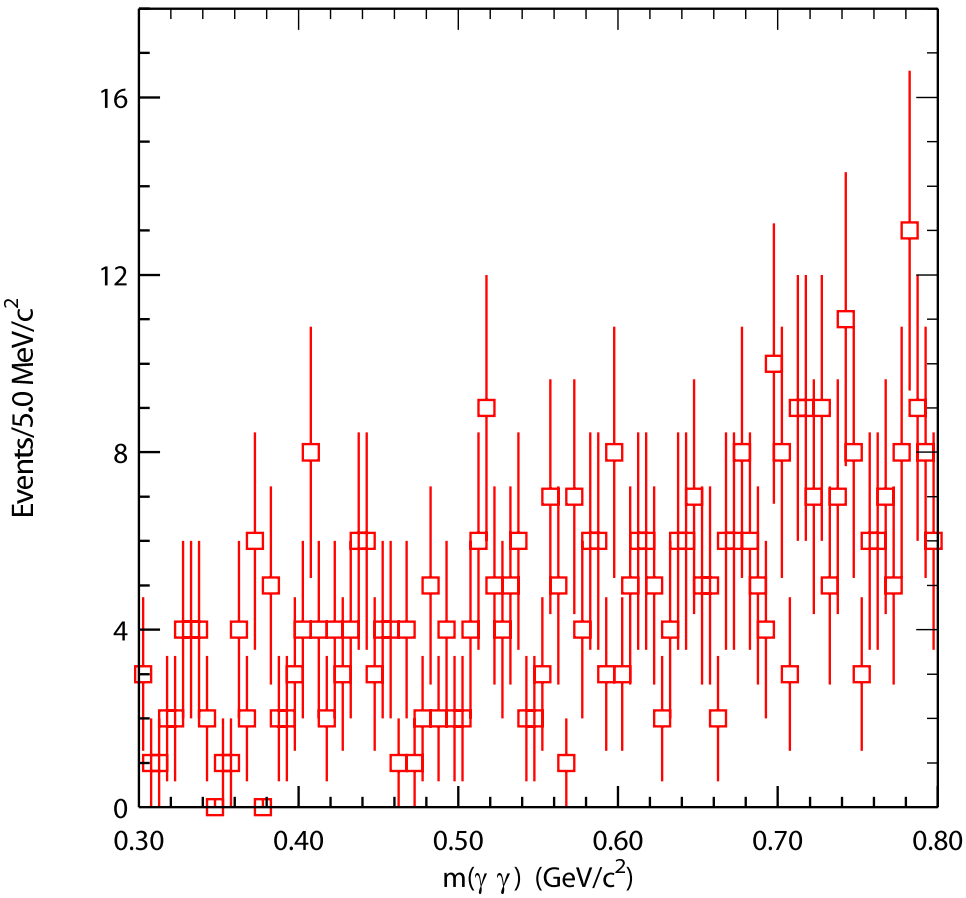

Figure 3–16. $\gamma\gamma$ invariant mass distribution in real data after all cuts.

Likelihood = 91.3

χ^2= 85.2 for 100 - 4 d.o.f., C.L.= 77.6%

Errors			Parabolic		Minos		
Function 1: Two Gaussians (sigma)							
AREA	-2.2984	±	8.698	-	8.363	+	9.047
* MEAN	0.54209	±	0.0000E+00	-	0.0000E+00	+	0.0000E+00
* SIGMA1	1.51605E-02	±	0.0000E+00	-	0.0000E+00	+	0.0000E+00
* AR2/AREA	0.15594	±	0.0000E+00	-	0.0000E+00	+	0.0000E+00
* DELM	0.00000E+00	±	0.0000E+00	-	0.0000E+00	+	0.0000E+00
* SIG2/SIG1	1.9340	±	0.0000E+00	-	0.0000E+00	+	0.0000E+00
Function 2: Chebyshev Polynomial of Order 2							
NORM	962.16	±	50.63	-	49.61	+	51.66
CHEB01	0.58156	±	7.1844E-02	-	7.3095E-02	+	7.0503E-02
CHEB02	4.85822E-02	±	8.0037E-02	-	8.0679E-02	+	7.9255E-02

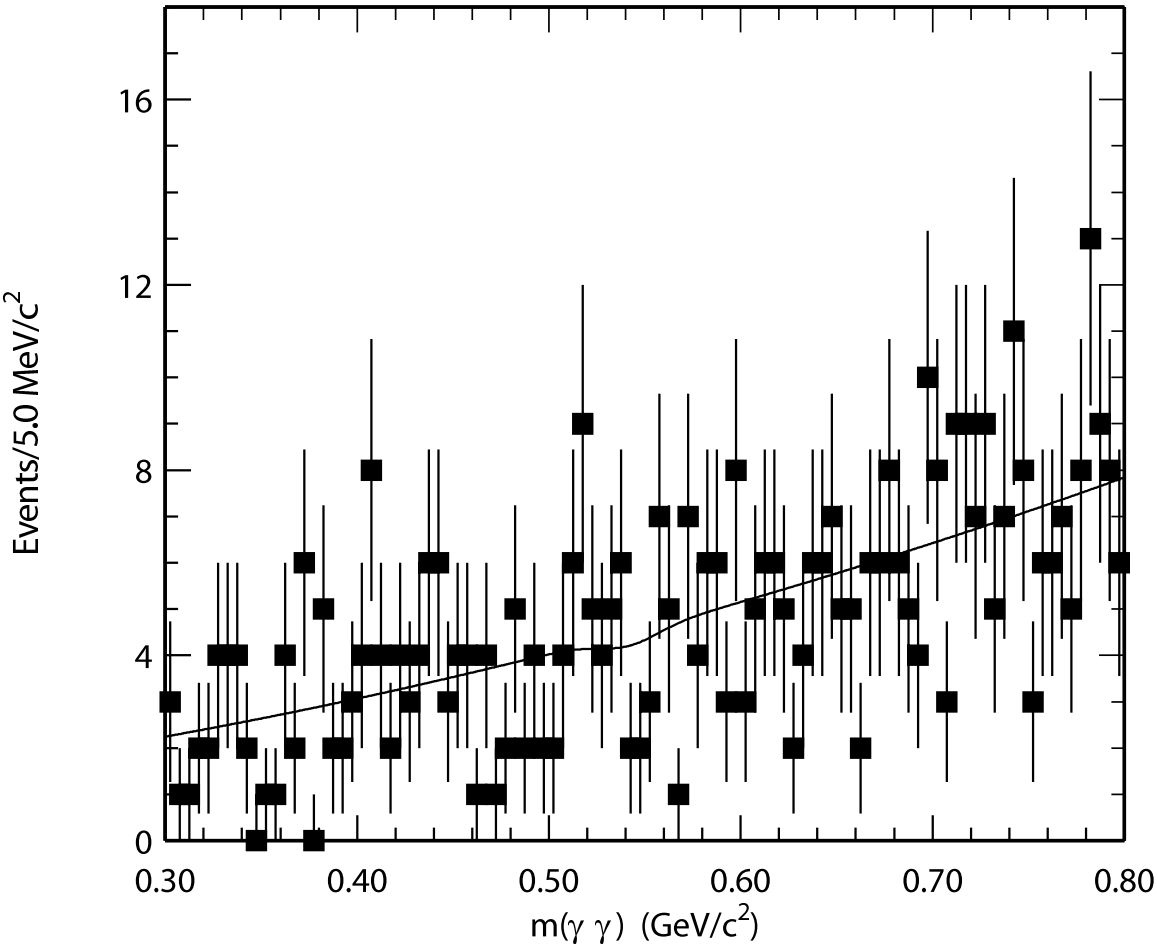

Figure 3–17. Fit to $\gamma\gamma$ invariant mass distribution for the mode $\Upsilon(1S) \to \gamma\eta; \eta \to \gamma\gamma$. Leaving the area floating while keeping the mean, width and other parameters fixed to MC fit parameters, we obtain -2.3 ± 8.7 events, which is consistent with 0.

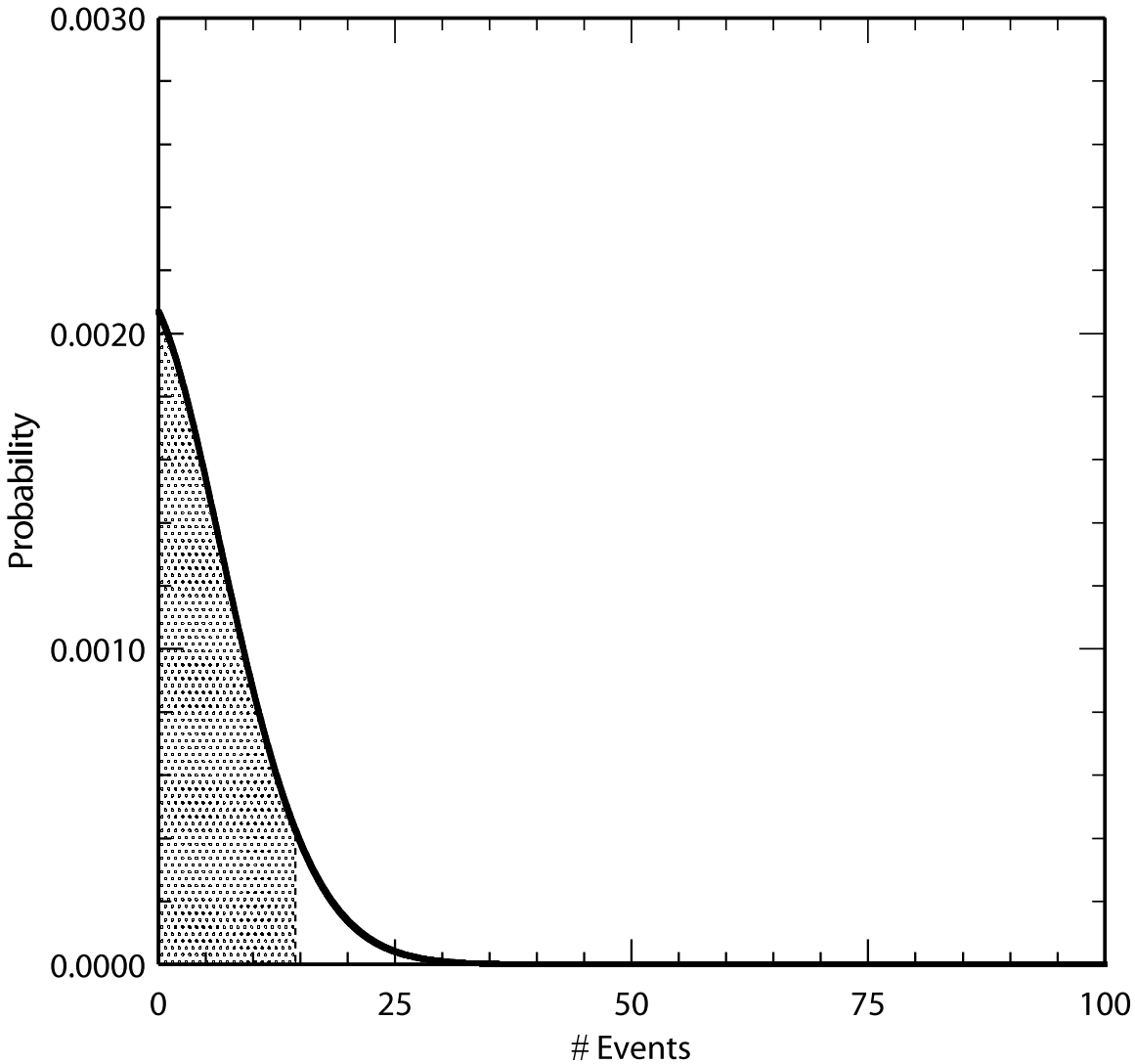

Figure 3–18. Normalized probability distribution for different signal area for the mode $\Upsilon(1S) \to \gamma\eta; \eta \to \gamma\gamma$. The shaded area spans 90% of the probability.

Likelihood = 94.6

χ^2= 87.9 for 100 - 3 d.o.f., C.L.= 73.5%

Errors		Parabolic	Minos	
Function 1: Two Gaussians (sigma)				
* AREA	14.460	± 0.0000E+00	- 0.0000E+00	+ 0.0000E+00
* MEAN	0.54209	± 0.0000E+00	- 0.0000E+00	+ 0.0000E+00
* SIGMA1	1.51605E-02	± 0.0000E+00	- 0.0000E+00	+ 0.0000E+00
* AR2/AREA	0.15594	± 0.0000E+00	- 0.0000E+00	+ 0.0000E+00
* DELM	0.00000E+00	± 0.0000E+00	- 0.0000E+00	+ 0.0000E+00
* SIG2/SIG1	1.9340	± 0.0000E+00	- 0.0000E+00	+ 0.0000E+00
Function 2: Chebyshev Polynomial of Order 2				
NORM	951.63	± 50.50	- 49.47	+ 51.55
CHEB01	0.58880	± 7.2552E-02	- 7.3821E-02	+ 7.1176E-02
CHEB02	0.10505	± 7.3963E-02	- 7.5016E-02	+ 7.2802E-02

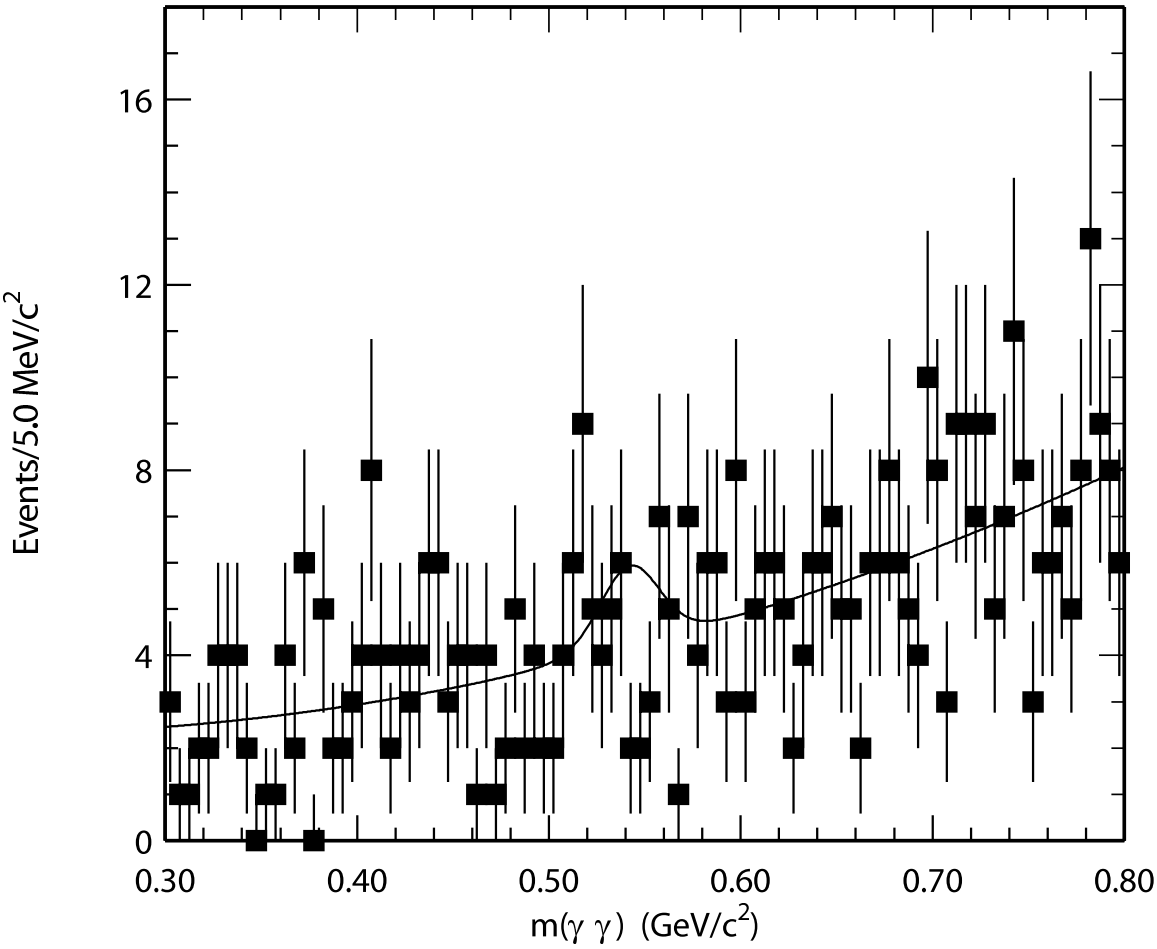

Figure 3–19. The fit to reconstructed $\gamma\gamma$ invariant mass distribution from real data for the mode $\Upsilon(1S) \to \gamma\eta; \eta \to \gamma\gamma$. The area is fixed to the number of events obtained from 90% confidence level upper limit. The mean, width and other parameters are fixed to the ones obtained from Monte Carlo.

3.3.4 Reconstruction of $\Upsilon(1\mathbf{S}) \to \gamma\eta'; \eta \to \gamma\gamma$

By selecting the $\Upsilon(1\mathrm{S})$ candidate with lowest value for $\chi^2_{\mathrm{P4}} + \chi^2_\eta$, we take care of multiple counting, a problem which is not so serious for this mode. Good quality η candidates are selected by requiring the $\chi^2_\eta < 200$ where χ^2_η is the χ^2 of constraining the η candidate to its nominal mass. To select the pion tracks and to reject the background from electron tracks, we require the $\mathrm{S}^2_{dE/dx}$ to be less than 16.0 (this was also a requirement for the mode $\Upsilon(1\mathrm{S}) \to \gamma\eta; \eta \to \pi^+\pi^-\pi^0$). To ensure that the event is fully reconstructed, i.e., balanced in momentum and adds up to the centre-of-mass energy of the e^+e^- system, we require the $\chi^2_{\mathrm{P4}} < 100$. The efficiency of the cuts used is listed in Table 3–7 .

Table 3–7. Final efficiency table for the mode $\eta' \to \eta\pi^+\pi^-$ and then $\eta \to \gamma\gamma$

Cut	Ind Eff (%)	Cmb Eff (%)
$\chi^2_\eta < 200$	99.6	41.9
$\mathrm{S}^2_{dE/dx} < 16$	99.7	41.8
$\chi^2_{\mathrm{P4}} < 100$	97.1	40.6
all cuts	40.6 ± 0.4	

The invariant mass distribution for the reconstructed η' candidate after above mentioned selection criteria from signal MC is shown in Figure 3–20. The invariant mass distribution for η' candidate from real data is shown in Figures 3–22 and 3–23. We find no candidate signal event within our acceptance mass window.

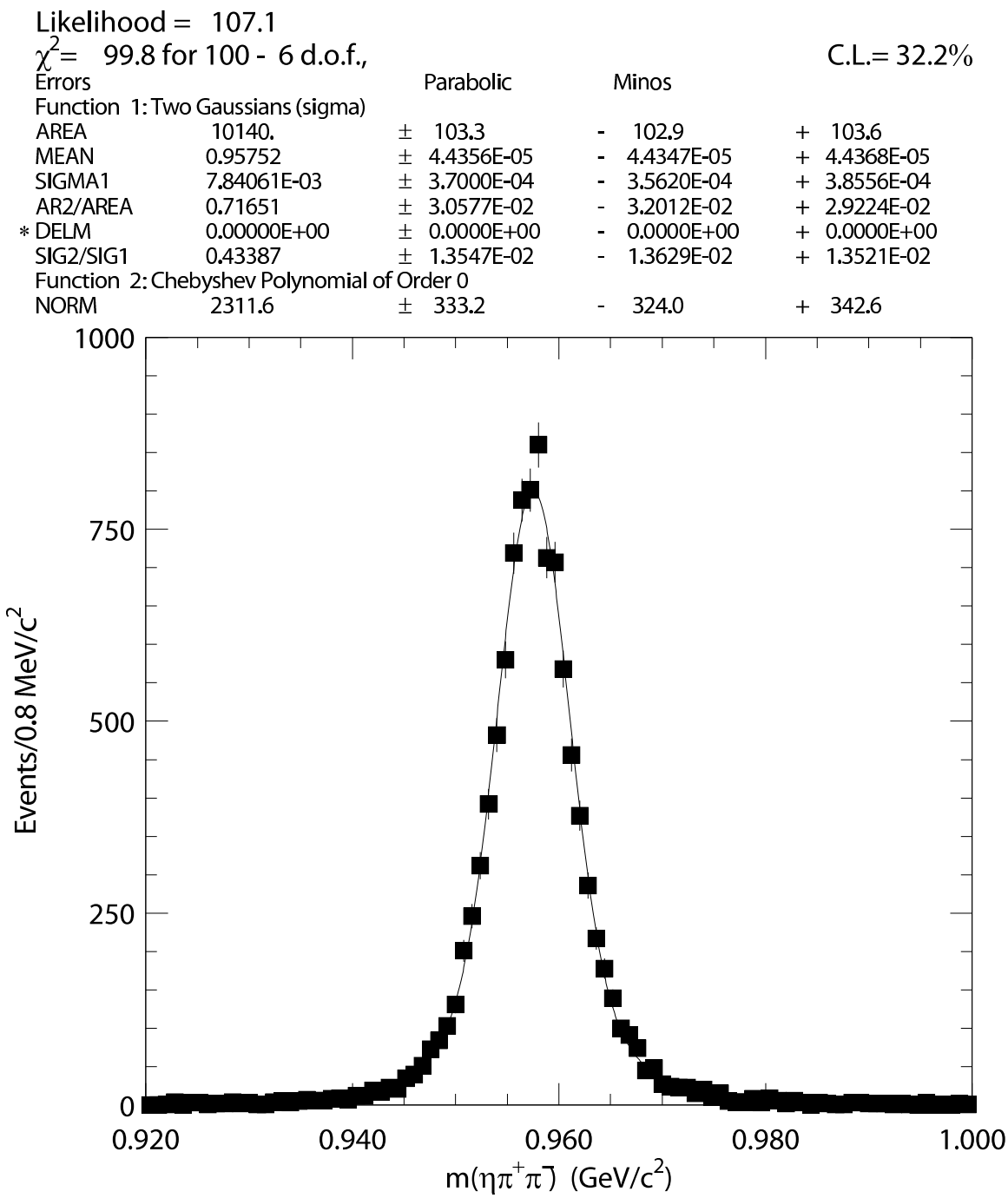

Figure 3–20. Reconstructed candidate η' invariant mass distribution from signal Monte Carlo for the mode $\Upsilon(1S) \to \gamma\eta'; \eta \to \gamma\gamma$. The reconstruction efficiency is $40.6 \pm 0.4\%$ after all the cuts.

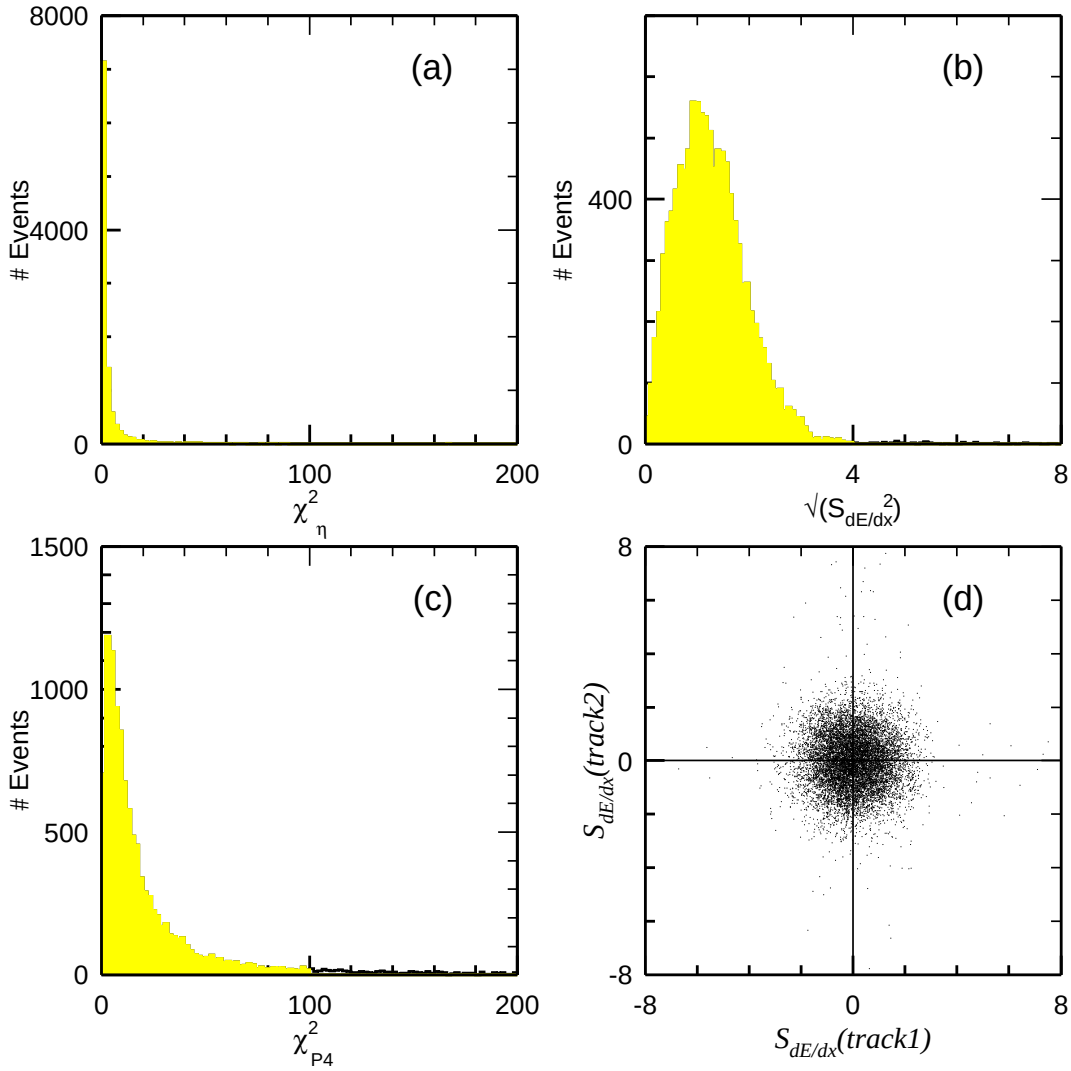

Figure 3–21. Distribution from signal Monte Carlo: For the mode $\Upsilon(1S) \to \gamma\eta'; \eta \to \gamma\gamma$, variables we cut on are plotted. The yellow (shaded) area in these plots represents the acceptance. Plot(a) χ^2_η distribution, plot(b) for $\sqrt{S^2_{dE/dx}}$, plot(c) for χ^2_{P4}, and plot(d) is a scatter plot of the dE/dx σ for pion hypothesis for the charged tracks.

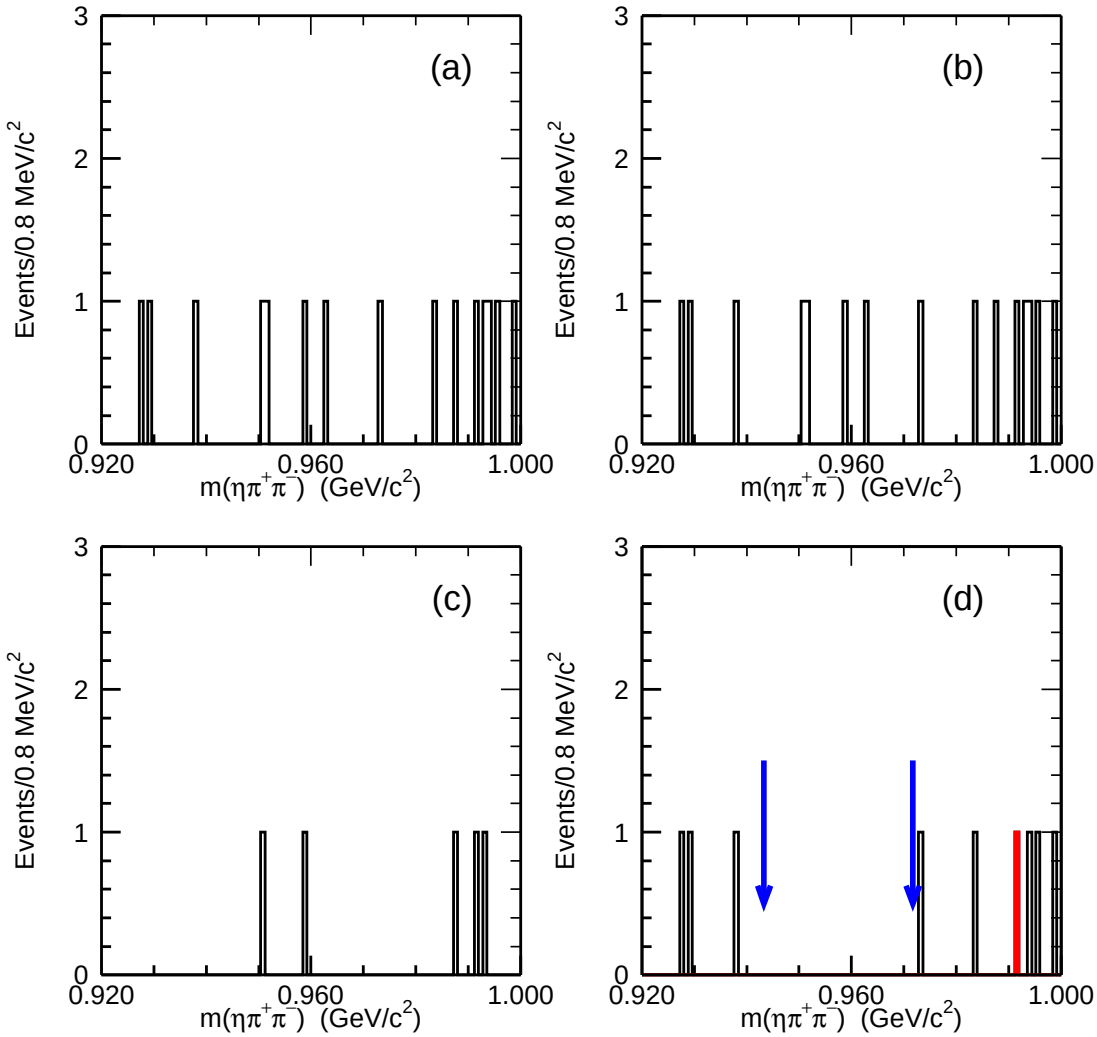

Figure 3–22. Invariant mass of η' candidate for the mode $\Upsilon(1S) \to \gamma\eta'; \eta \to \gamma\gamma$: Plot(a) without any cuts, plot(b) after selecting candidates with $\chi^2_\eta < 200$, plot(c) after dE/dx cut, plot(d) requiring $\chi^2_{P4} < 100$. The red overlay on plot(d) is obtained after imposing all the cuts. No candidate signal event is observed in our acceptance mass window (denoted by blue arrows).

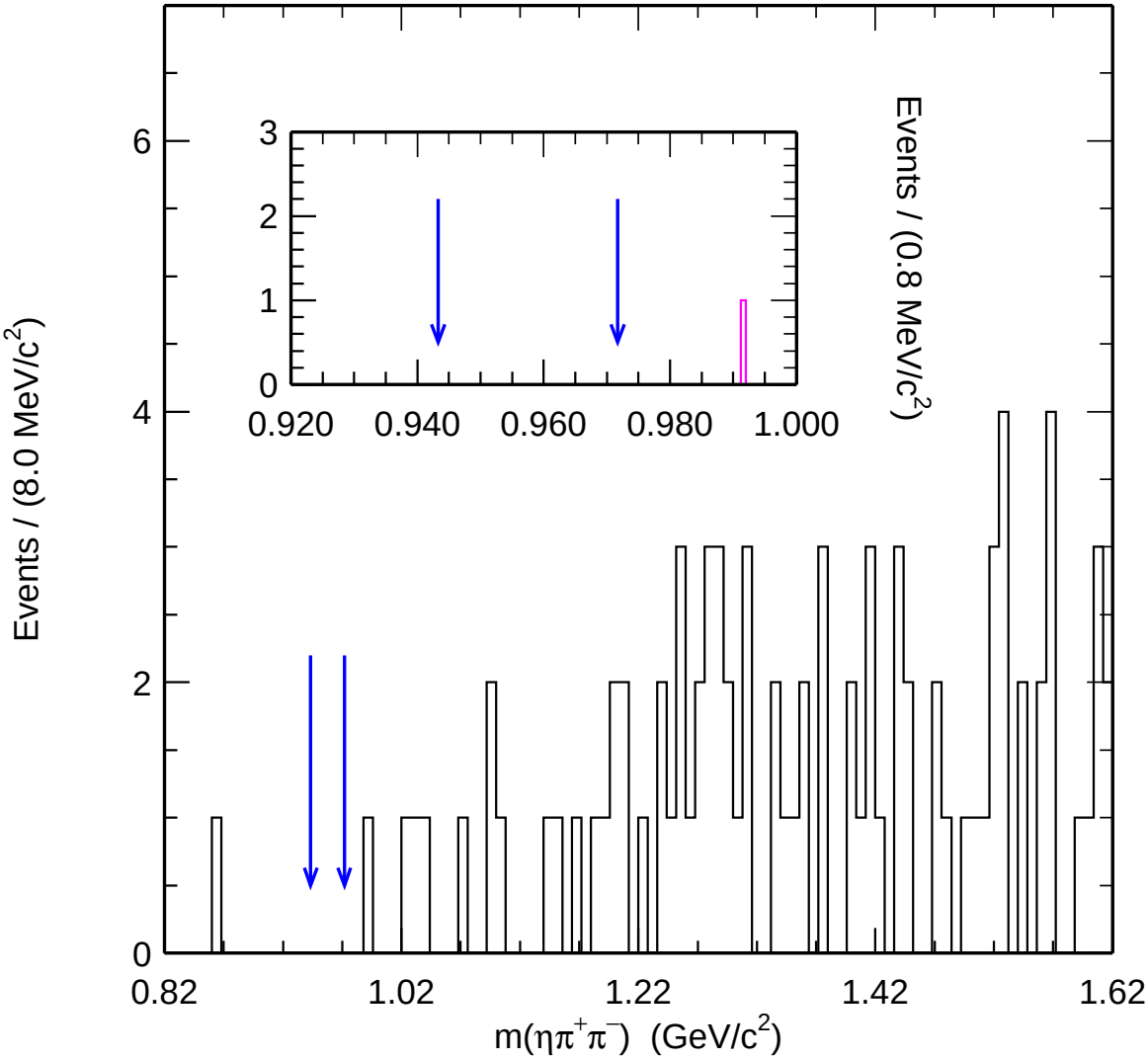

Figure 3–23. Extended range of invariant mass distribution of η' candidate for the mode $\Upsilon(1S) \to \gamma\eta'; \eta \to \gamma\gamma$. No candidate signal event is observed in our acceptance mass window (inset).

3.3.5 Reconstruction of $\Upsilon(1S) \to \gamma\eta'; \eta \to \pi^0\pi^0\pi^0$

This is one of the three modes studied in this analysis where multiple counting poses a serious problem. The origin of the problem, like in the mode $\Upsilon(1S) \to \gamma\eta; \eta \to \pi^0\pi^0\pi^0$, lies in the decay of high energy η into 3 π^0 mesons where the showers from different π^0 mesons lie so close to each other in the CC and are so close in energy that an overwhelming number of η candidates are reconstructed. Such η candidates have invariant mass close to the nominal η mass, leading to poor resolution and an artificially high efficiency.

From the whole raff of $\Upsilon(1S)$ candidates, we select the one having lowest χ^2_{Total} where $\chi^2_{Total} = \chi^2_{\pi^0_1} + \chi^2_{\pi^0_2} + \chi^2_{\pi^0_3} + \chi^2_{\eta} + \chi^2_{\mathrm{P4}}$. The π^0 candidates are selected by requiring $\sqrt{S^2_\pi} < 10$. Good quality η candidates are selected by requiring the $\chi^2_\eta < 200$. To be consistent with other modes, we require $\sqrt{\mathrm{S}^2_{dE/dx}}$ to be less than 4. Energy-momentum conservation is enforced by requiring χ^2_{P4} to be less than 200. The efficiency for all these cuts is listed in Table 3–8 and the distribution for cut variables is shown in Figure 3–25.

Table 3–8. Final efficiency table for the mode $\eta' \to \eta\pi^+\pi^-$ and then $\eta \to \pi^0\pi^0\pi^0$

Cut	Ind Eff (%)	Cmb Eff (%)
$\chi^2_\eta < 200$	98.3	22.8
$\sqrt{\mathrm{S}^2_{dE/dx}} < 4$	99.9	22.7
$\chi^2_{\mathrm{P4}} < 200$	96.3	21.9
$\sqrt{S^2_\pi}$ of $\pi^0 s < 10$	73.7	16.6
all cuts	16.6 ± 0.4	

Using the above reconstruction scheme, the invariant mass for reconstructed η' candidate is shown in Figure 3–24. We find no candidate event in real data as the Figures 3–26 and 3–27 show.

Likelihood = 104.0

χ^2= 99.9 for 100 - 8 d.o.f., C.L.= 27.0%

Errors		Parabolic	Minos	
Function 1: Two Gaussians (sigma)				
AREA	4138.0	± 108.8	- 105.1	+ 114.2
MEAN	0.95706	± 9.4093E-05	- 9.4181E-05	+ 9.4031E-05
SIGMA1	8.95188E-03	± 7.1537E-04	- 6.6378E-04	+ 7.8420E-04
AR2/AREA	0.52764	± 4.8912E-02	- 5.0541E-02	+ 4.7314E-02
* DELM	0.00000E+00	± 0.0000E+00	- 0.0000E+00	+ 0.0000E+00
SIG2/SIG1	0.39751	± 2.1951E-02	- 2.1682E-02	+ 2.2505E-02
Function 2: Chebyshev Polynomial of Order 2				
NORM	6300.3	± 822.1	- 879.7	+ 788.0
CHEB01	-5.29920E-02	± 5.5787E-02	- 5.7735E-02	+ 5.6000E-02
CHEB02	-0.90488	± 7.4757E-02	- 6.4937E-02	+ 8.8170E-02

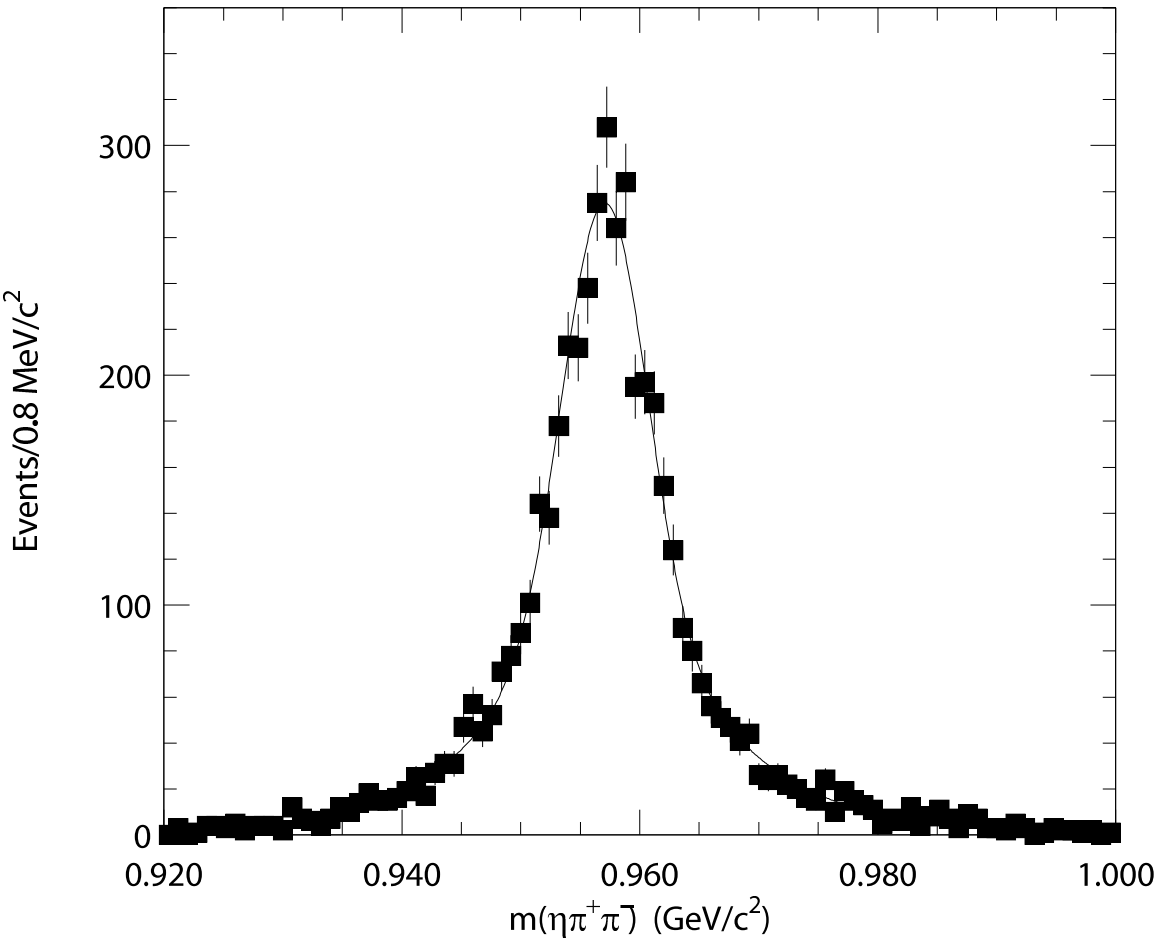

Figure 3–24. Reconstructed invariant mass distribution of the candidate η' from signal Monte Carlo for the mode $\Upsilon(1S) \rightarrow \gamma\eta'; \eta \rightarrow \pi^0\pi^0\pi^0$: The reconstruction efficiency is $16.6 \pm 0.4\%$ after all the cuts.

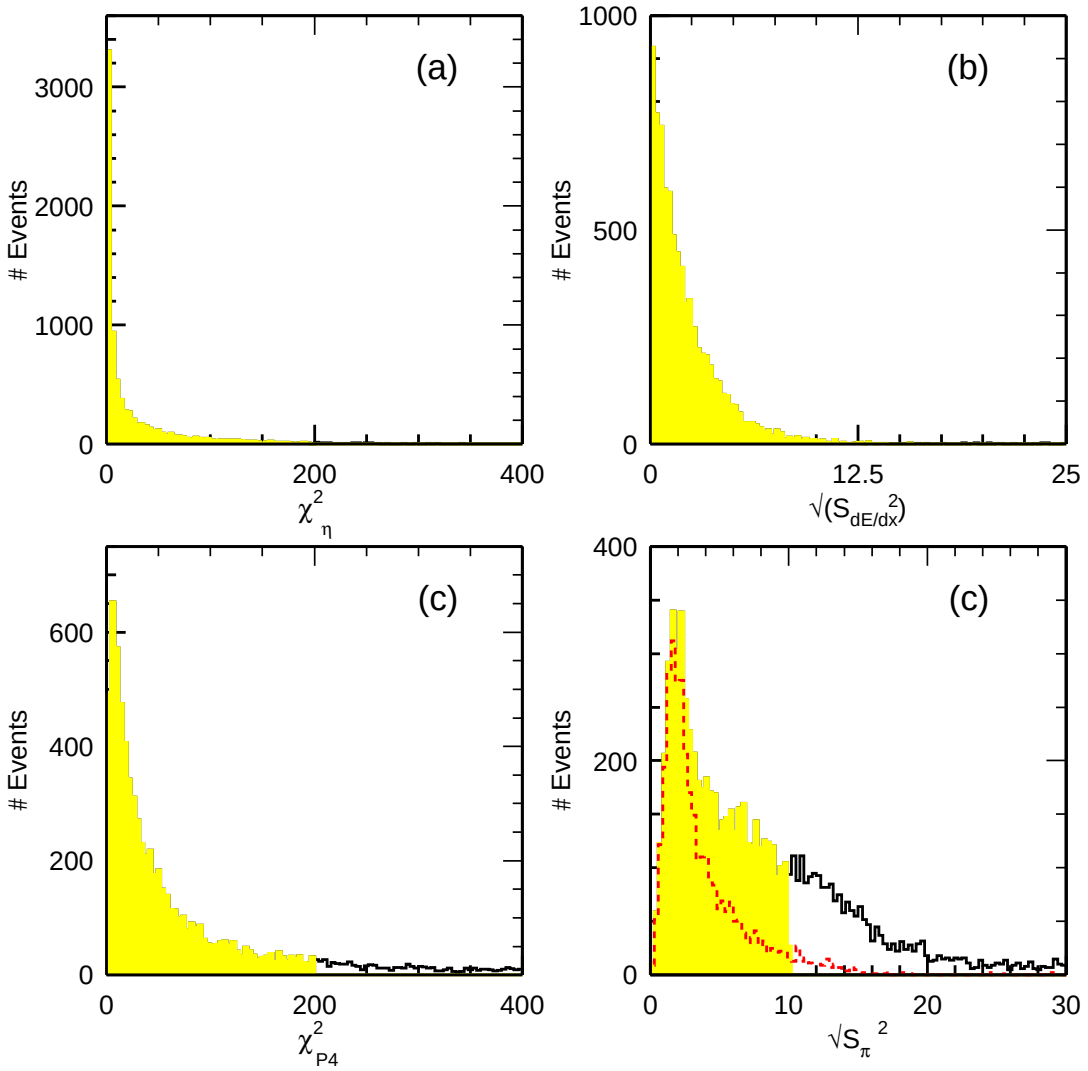

Figure 3–25. Distributions from signal Monte Carlo: For the mode $\Upsilon(1S) \to \gamma\eta'; \eta \to \pi^0\pi^0\pi^0$, variables we cut on are plotted. The yellow (shaded) area in these plots represents the acceptance. Plot(a) for χ^2_η, Plot(b) $\sqrt{S^2_{dE/dx}}$ for two tracks, plot(c) for χ^2_{P4}, and plot(d) $\sqrt{S^2_\pi}$ of the π^0 candidates. The dashed (red) line in plot(d) shows the $\sqrt{S^2_\pi}$ of the tagged π^0 candidates. As can be seen, majority of good events are confined within $\sqrt{S^2_\pi} < 10.0$, giving us a reason to select our acceptance region.

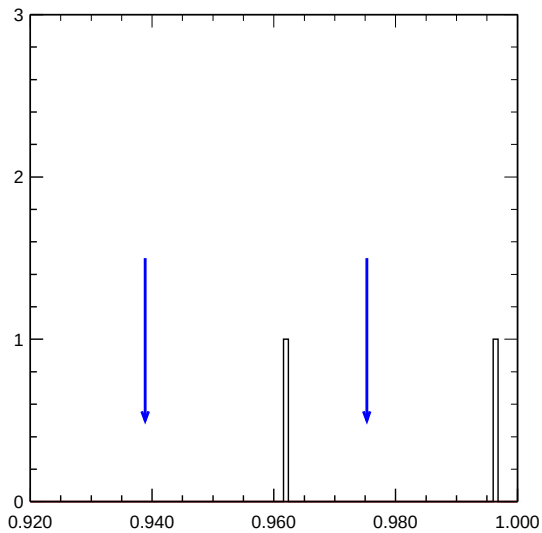

Figure 3–26. Invariant mass of η' candidate for the mode $\Upsilon(1S) \to \gamma\eta'; \eta \to \pi^0\pi^0\pi^0$: We found two events when no cuts are in place. None of the two events in the η' invariant mass histogram survive the $\chi^2_{\mathrm{P4}} < 200$ requirement.

3.3.6 Reconstruction of $\Upsilon(1\mathbf{S}) \to \gamma\eta'; \eta \to \pi^+\pi^-\pi^0$

We first constrain a pair of oppositely charged tracks to originate from a common vertex. Next, we add a π^0 candidate and build the η candidate. The η candidate is mass-constrained to its nominal mass and then vertexed to another pair of oppositely charged tracks to make η'.

The kinematics of the charged tracks involved in this mode is such that using wrong tracks at the η reconstruction level results in η' having invariant mass within the acceptance region very often. This leads to multiple counting and poor resolution. To handle this situation, the $\Upsilon(1S)$ candidate with lowest χ^2_{Total} is selected where χ^2_{Total} means $\chi^2_{\pi^0} + \chi^2_{\eta} + \chi^2_{\mathrm{P4}}$. The selected $\Upsilon(1S)$ candidate is required to pass the consistency checks listed in Table 3–9.

Figure 3–28 shows the invariant mass distribution for η' candidates passing our selection criteria. Figure 3–29 shows the distribution of cut variables used in this

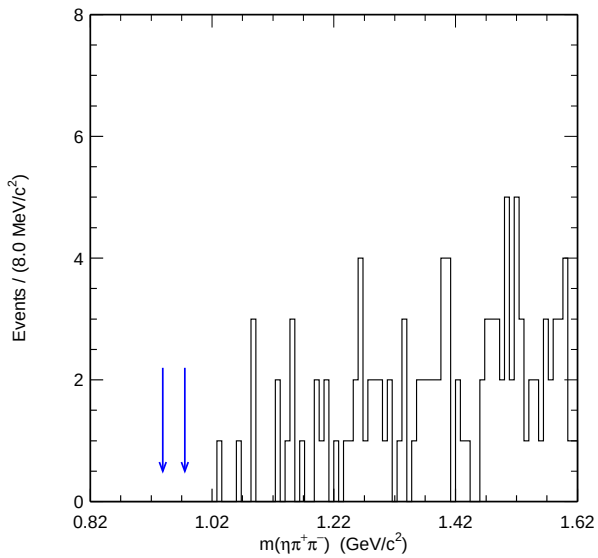

Figure 3–27. Extended range of invariant mass distribution of η' candidate for the mode $\Upsilon(1S) \to \gamma\eta'; \eta \to \pi^0\pi^0\pi^0$. No candidate signal event is observed in our acceptance mass window

mode. In real data, we find two candidate events passing our selection cuts, as shown in Figure 3–30. These two events have been looked at in detail and show no signs of not being good signal events.

Table 3–9. Final efficiency table for the mode $\Upsilon(1S) \to \gamma\eta'; \eta \to \pi^+\pi^-\pi^0$

Cut	Ind Eff (%)	Cmb Eff (%)
$\chi^2_{\mathrm{P4}} < 200$	96.6	25.4
$\sigma_{\gamma\gamma}$ of $\pi^0 < 10$	97.9	24.8
$\chi^2_{\eta} < 100$	99.1	24.7
$\sqrt{\mathrm{S}^2_{dE/dx}} < 4$	98.9	24.5
all cuts	24.5 ± 0.4	

Likelihood = 111.0

χ^2= 112.5 for 100 - 8 d.o.f., C.L.= 7.2%

Errors		Parabolic	Minos	
Function 1: Two Gaussians (sigma)				
AREA	6125.0	± 107.5	- 106.1	+ 109.1
MEAN	0.95752	± 5.4365E-05	- 5.4391E-05	+ 5.4347E-05
SIGMA1	7.00002E-03	± 4.1859E-04	- 3.9725E-04	+ 4.4388E-04
AR2/AREA	0.56394	± 3.4331E-02	- 3.5332E-02	+ 3.3364E-02
* DELM	0.00000E+00	± 0.0000E+00	- 0.0000E+00	+ 0.0000E+00
SIG2/SIG1	0.36746	± 1.5146E-02	- 1.4990E-02	+ 1.5392E-02
Function 2: Chebyshev Polynomial of Order 2				
NORM	12188.	± 717.1	- 726.8	+ 711.2
CHEB01	-0.17360	± 4.6555E-02	- 4.6885E-02	+ 4.6422E-02
CHEB02	-0.68293	± 7.0060E-02	- 6.5904E-02	+ 7.4719E-02

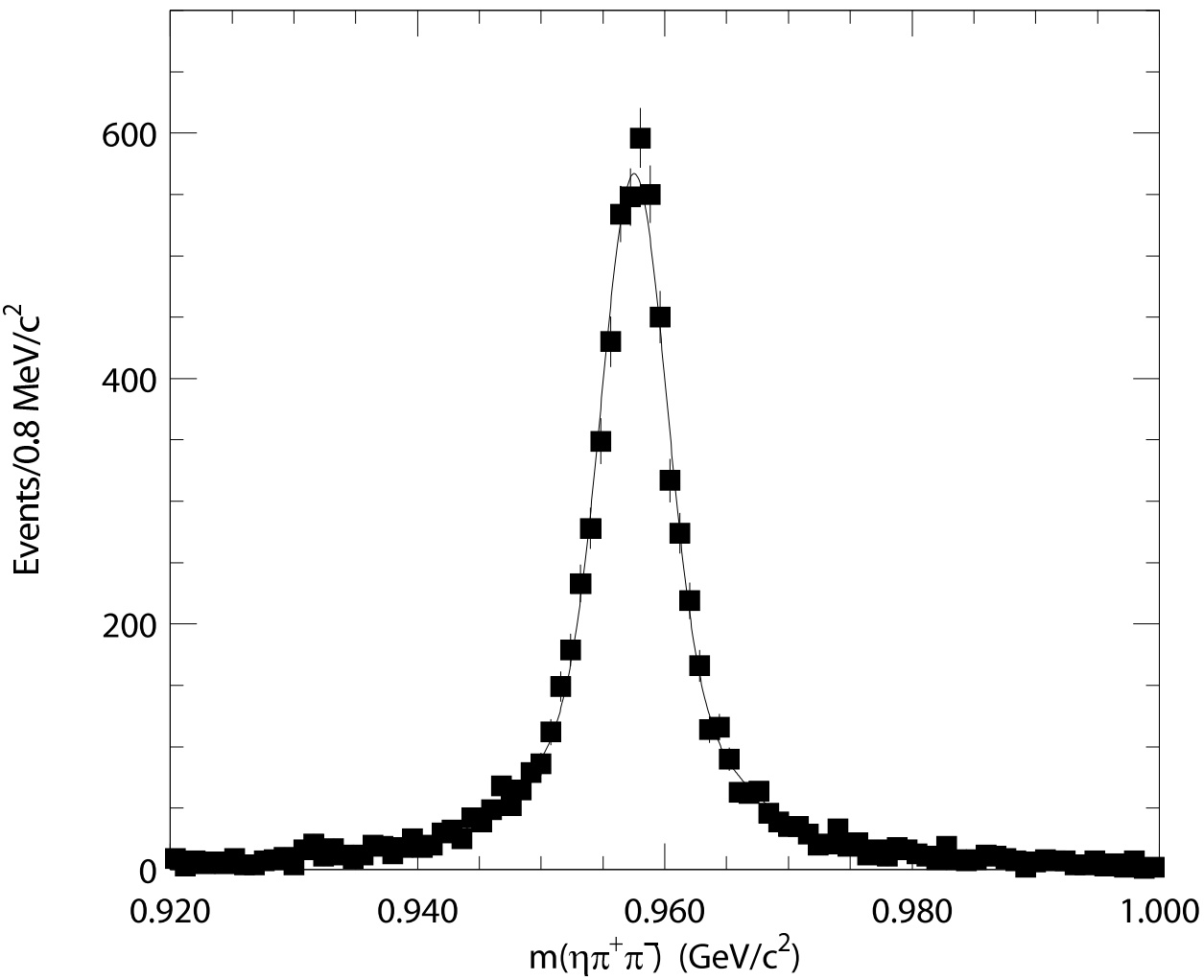

Figure 3–28. Reconstructed candidate η' invariant mass distribution from signal Monte Carlo for the mode $\Upsilon(1S) \rightarrow \gamma\eta'; \eta \rightarrow \pi^+\pi^-\pi^0$: The reconstruction efficiency is $24.5 \pm 0.5\%$ after all the cuts.

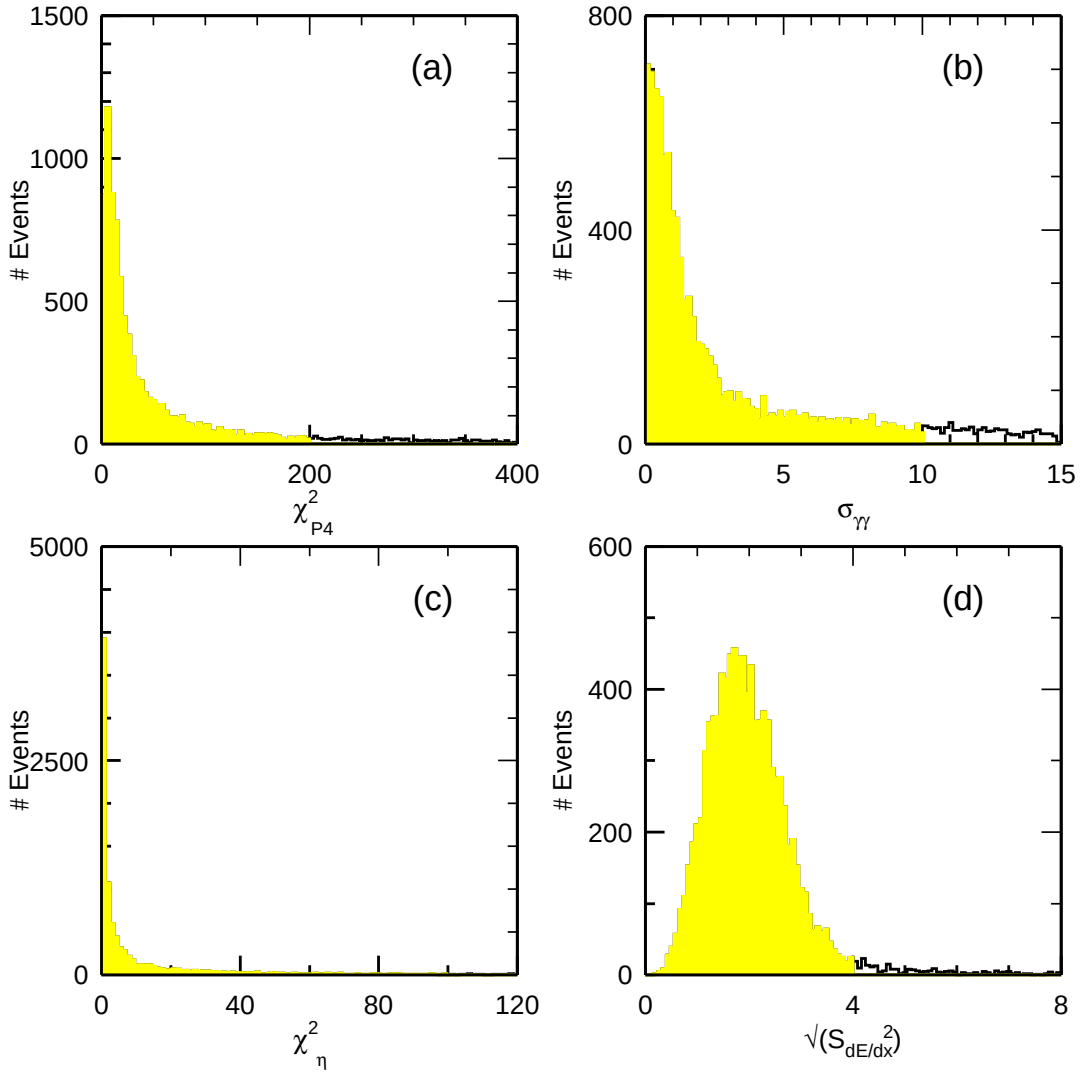

Figure 3–29. Distribution from signal Monte Carlo: For the mode $\Upsilon(1S) \to \gamma\eta'; \eta \to \pi^+\pi^-\pi^0$, variables we cut on are plotted. The yellow (shaded) area in these plots represents the acceptance. Plot(a) for χ^2_{P4}, plot(b) for $\sigma_{\gamma\gamma}$ of π^0 candidate plot(c) for χ^2_η, and Plot(d) $\sqrt{S^2_{dE/dx}}$ for all four tracks.

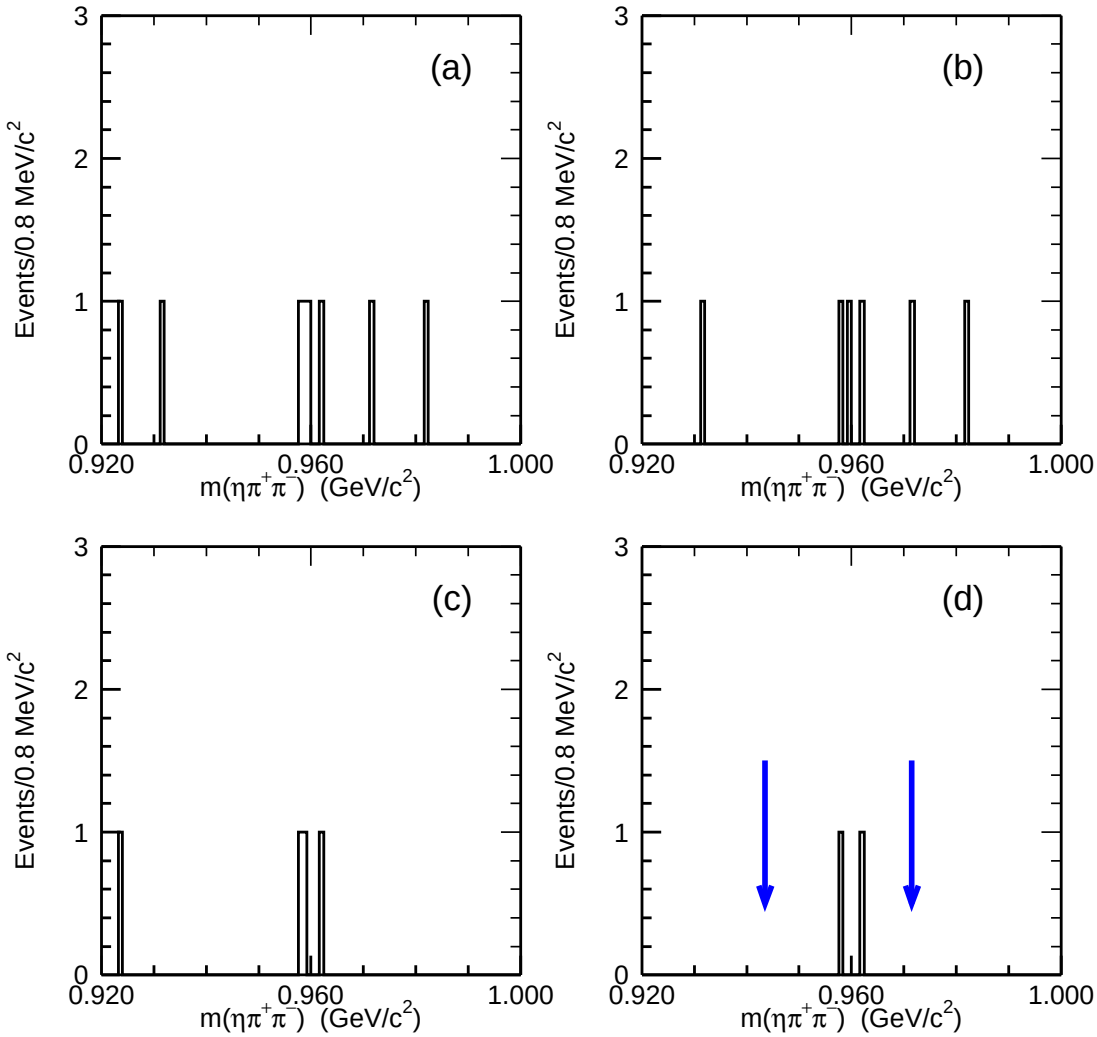

Figure 3–30. Invariant mass of η' candidate for the mode $\Upsilon(1S) \to \gamma\eta'; \eta \to \pi^+\pi^-\pi^0$: Plot(a) with no cuts, plot(b) with the requirement $\chi^2_{\mathrm{P4}} < 100$, plot(c) with pion hypothesis consistency in the form $\sqrt{\mathrm{S}^2_{dE/dx}} < 4.0$, and plot(d) with all the cuts. We find two candidate events.

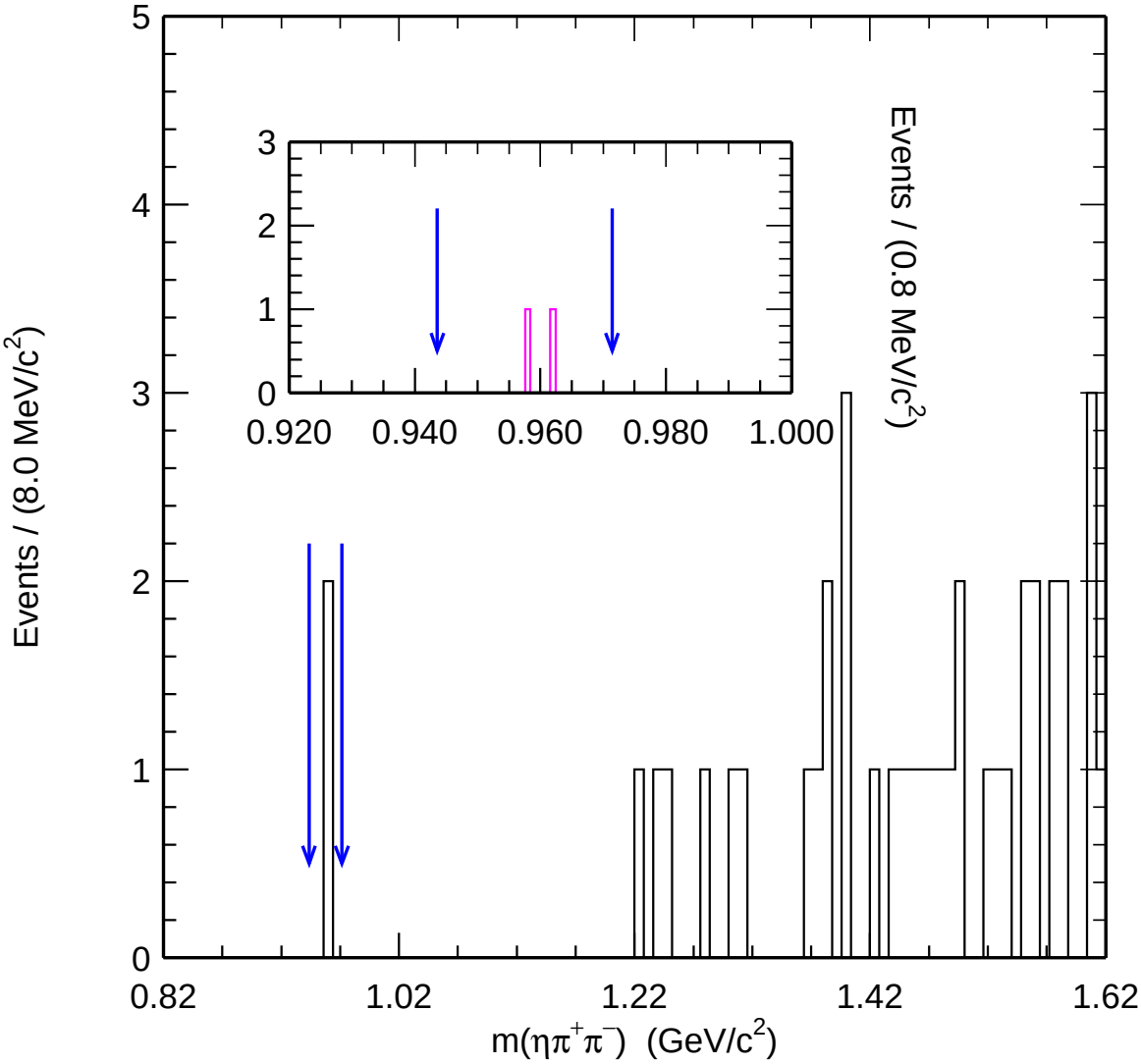

Figure 3–31. Extended range of invariant mass distribution of η' candidate for the mode $\Upsilon(1S) \to \gamma\eta'; \eta \to \pi^+\pi^-\pi^0$. Two good candidate signal events are observed in our acceptance mass window (inset).

3.3.7 Reconstruction of $\Upsilon(1\mathbf{S}) \to \gamma\eta'$; $\eta' \to \gamma\rho$

The ρ candidate is reconstructed by constraining two oppositely charged good tracks to originate from a common vertex. We then select a photon candidate (which we refer to as the "soft photon" having energy E_s in contrast with the high energy radiative photon) having lateral profile consistent with being a photon and not associated to a charged track. This soft photon is added to the ρ candidate to reconstruct η' candidate. The $\Upsilon(1\mathrm{S})$ candidate is then reconstructed by adding[7] a hard photon to the η' candidate. The $\Upsilon(1\mathrm{S})$ candidate is constrained to the 4-momentum of the initial e^+e^- system and during the kinematic fitting, we keep track of the four-momenta of constituents (i.e., ρ, soft photon and the hard photon). We then use the updated E_s and the updated invariant mass of the η' candidate in our analysis. The kinematic fitting improves both the resolution as well as η' yield (see Figure 3–32). To handle multiple counting, the combination having lowest value for fit $\chi^2_{\mathrm{P}4}$ was selected.

To reduce the background from misidentified charged tracks, we combine the dE/dx and $RICH$ information for the pair of charged tracks in one number, (e.g., $\Delta\chi^2_{ID}(\pi - K)$ to distinguish between pions and kaons) as follows:

$$\begin{aligned}\Delta\chi^2_{ID}(\pi - K) \;=\; & \mathrm{S}^2_{dE/dx}(\pi^+) - \mathrm{S}^2_{dE/dx}(K^+) \;+ \mathrm{S}^2_{dE/dx}(\pi^-) - \mathrm{S}^2_{dE/dx}(K^-) \\ & -2\log(\mathcal{L}_{RICH}(\pi^+)) + 2\log(\mathcal{L}_{RICH}(K^+)) \\ & -2\log(\mathcal{L}_{RICH}(\pi^-)) + 2\log(\mathcal{L}_{RICH}(K^-))\end{aligned} \tag{3–1}$$

where $\Delta\chi^2_{ID}(\pi - K) < 0$ implies that the pair is more likely to be $\pi^+\pi^-$ than K^+K^-. Our particle identification cut "Particle Identification" as listed in Table 3–10 comprises of the requirement $\Delta\chi^2_{ID}(\pi - K) < 0$ and $\Delta\chi^2_{ID}(\pi - p) < 0$ simultaneously.

[7] The particles for this mode are not combined in the way as described in Section 3.3. We rather build an object where 4-momenta and the error matrices of individual particles are kept track during the kinematic fitting.

To be able to use the *RICH* information, we require that a track's momentum be above the Cherenkov radiation threshold for both mass hypotheses under consideration, and there are at least 3 photons within 3σ of the Cherenkov angle for at least one of the mass hypotheses. We also require that both the mass hypotheses under consideration were analyzed by *RICH* during pass2. If neither dE/dx nor *RICH* information is available, we accept the pair as $\pi^+\pi^-$ by default.

We also veto the electrons by requiring the *eop* for both tracks be outside of the range 0.95–1.05 and $\Delta\chi^2_{ID}(e-\pi) > 0$. Muon tracks are rejected by requiring that the DPTHMU (defined in Section 2.3.5) for both tracks be less than 5.

To ensure that the reconstructed decay chain makes the complete event, χ^2_{P4} is required to be < 100. Finally, to reject the complete, background events of type $e^+e^- \to \gamma\gamma\rho$, we require E_s, the updated energy (after kinematic fitting) of the photon from η' decay to be greater than 100.0 MeV. The efficiency of the cuts used is listed in Table 3–10.

Figure 3–33 shows the $\eta' \to \gamma\rho$ invariant mass distribution for signal MC events passing our selection criteria. In real data, our cuts are not sufficient to suppress the continuum background as Figure 3–34 shows. There is no visible peak in the η' invariant mass distribution either. To subtract the continuum background, we try two different approaches where 1) we subtract the scaled continuum data from 4S data and assume the same efficiency at higher energy 2) we parameterize the background using a smooth background function (a flat background in this case). We fit the invariant mass distribution for η' candidates using a double Gaussian function (the fit parameters are fixed from MC) and a polynomial background function. We let the area float and compare the uncertainty on the final yield from fit and chose the one which gives us smaller relative uncertainty. We find that continuum subtracted distribution, when fitted with yield floating gives us -3.5 ± 6.3 events whereas -3.1 ± 5.3 events are obtained without continuum subtraction as Figures 3–36 and 3–35 show.

Since the difference between relative uncertainties is very small and the efficiency at the 4S energy is not well studied, we choose not to do a continuum subtraction using 4S data.

Table 3–10. Efficiency table for the mode $\Upsilon(1S) \to \gamma\eta'$; $\eta' \to \gamma\rho$

Cut	Ind Eff (%)	Cmb Eff (%)
Particle Identification	99.2	45.8
Electron Veto	91.7	42.0
Muon Rejection	99.1	41.6
4-Momentum Consistency	98.8	41.4
E_s	97.0	40.1
all cuts	40.1 ± 0.4	

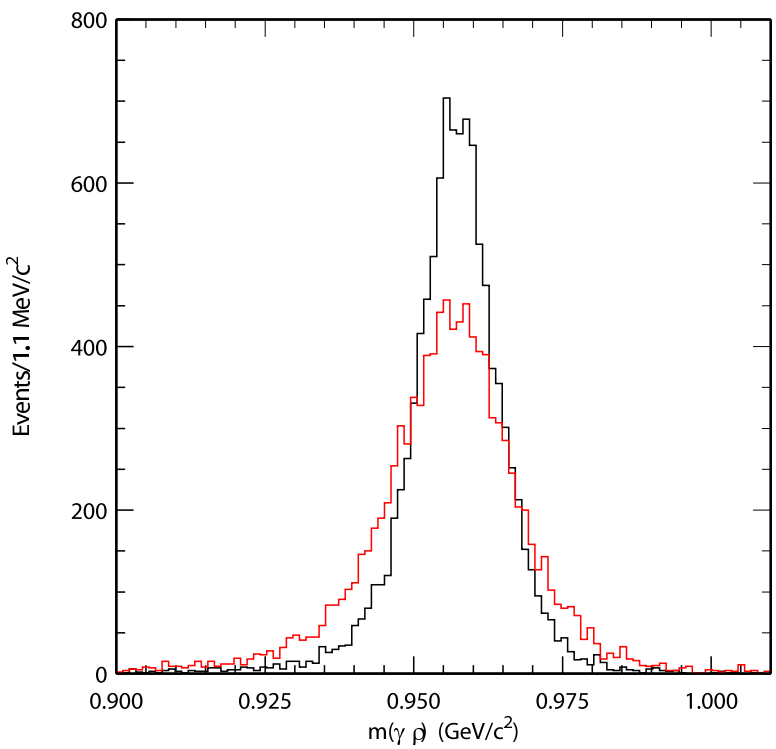

Figure 3–32. Reconstructed $\gamma\rho$ candidate invariant mass distribution from signal MC for $\eta' \to \gamma\rho$: The kinematic fitting improves the invariant mass resolution by $\approx 30\%$ and reconstruction efficiency by $\approx 5\%$.

Likelihood = 133.1

χ^2= 126.2 for 100 - 8 d.o.f., C.L.= 1.0%

Errors		Parabolic	Minos	
Function 1: Two Gaussians (sigma)				
AREA	10023.	± 110.0	- 106.9	+ 0.0000E+00
MEAN	0.95729	± 7.3778E-05	- 7.3482E-05	+ 7.3754E-05
SIGMA1	5.07704E-03	± 3.2340E-04	- 3.3426E-04	+ 3.0377E-04
AR2/AREA	0.49286	± 8.2800E-02	- 7.6504E-02	+ 8.0954E-02
* DELM	0.00000E+00	± 0.0000E+00	- 0.0000E+00	+ 0.0000E+00
SIG2/SIG1	1.8421	± 5.9078E-02	- 0.0000E+00	+ 6.2613E-02
Function 2: Chebyshev Polynomial of Order 2				
NORM	3446.0	± 342.4	- 311.3	+ 0.0000E+00
CHEB01	-0.25317	± 3.0666E-05	- 0.0000E+00	+ 0.0000E+00
CHEB02	-0.78044	± 6.6059E-02	- 0.0000E+00	+ 5.5959E-02

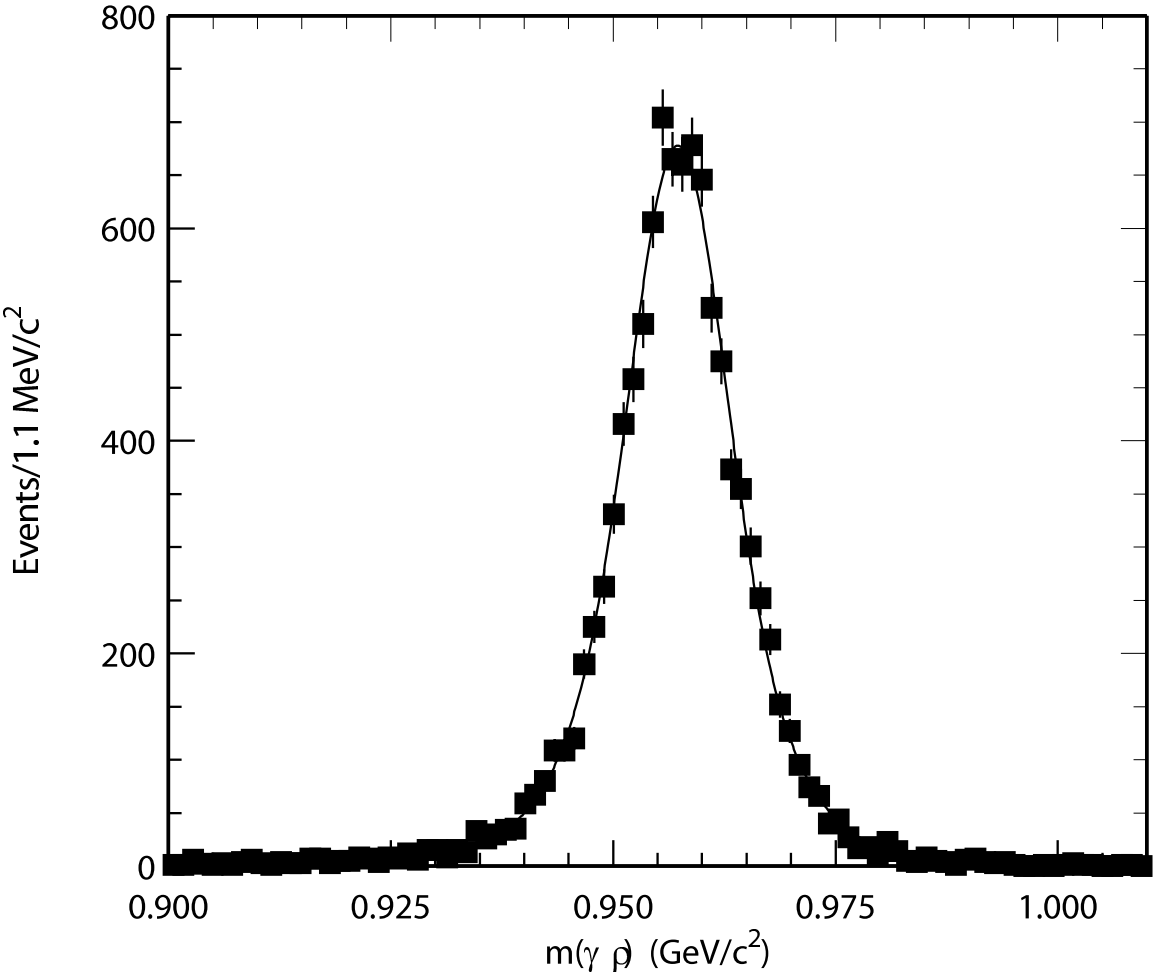

Figure 3–33. Reconstructed invariant mass distribution from signal Monte Carlo for the mode $\Upsilon(1S) \to \gamma\eta'$; $\eta' \to \gamma\rho$: The reconstruction efficiency is $40.1 \pm 0.4\%$ after all the cuts.

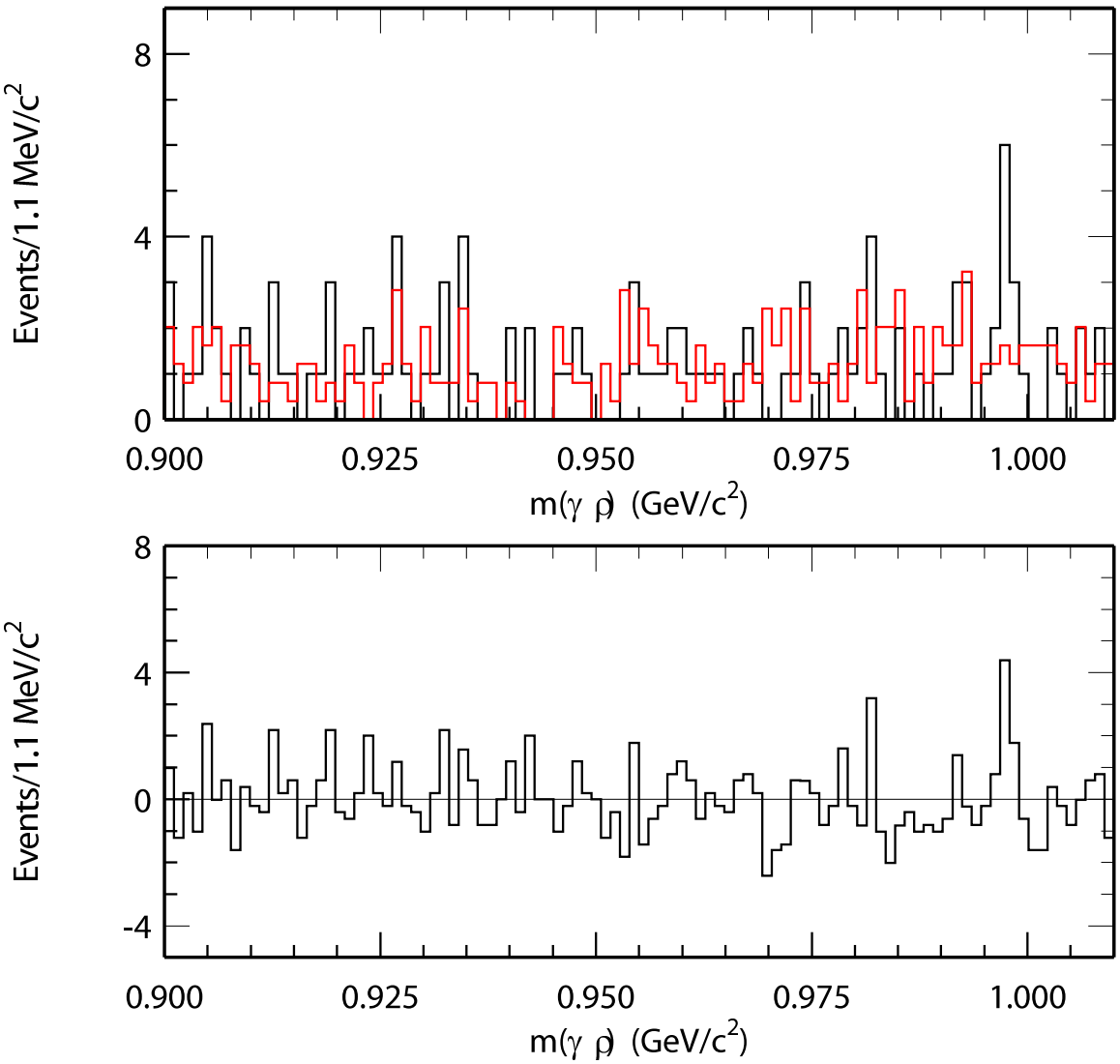

Figure 3–34. Reconstructed invariant mass distribution in real data for the mode $\Upsilon(1S) \to \gamma\eta'$; $\eta' \to \gamma\rho$: In top plot, black histogram shows the distribution from 1S data and overlaid in red is the scaled distribution from 4S data. The bottom plot after subtracting the continuum. We assume the same reconstruction efficiency at 4S energy.

Likelihood = 118.3

χ^2= 108.6 for 100 - 3 d.o.f., C.L.= 19.8%

Errors		Parabolic	Minos	
Function 1: Two Gaussians (sigma)				
AREA	-3.0881	± 5.279	- 4.970	+ 5.619
* MEAN	0.95729	± 0.0000E+00	- 0.0000E+00	+ 0.0000E+00
* SIGMA1	5.07704E-03	± 0.0000E+00	- 0.0000E+00	+ 0.0000E+00
* AR2/AREA	0.49286	± 0.0000E+00	- 0.0000E+00	+ 0.0000E+00
* DELM	0.00000E+00	± 0.0000E+00	- 0.0000E+00	+ 0.0000E+00
* SIG2/SIG1	1.8421	± 0.0000E+00	- 0.0000E+00	+ 0.0000E+00
Function 2: Chebyshev Polynomial of Order 1				
NORM	1146.2	± 113.9	- 110.2	+ 117.7
CHEB01	2.97205E-02	± 0.1486	- 0.1486	+ 0.1476

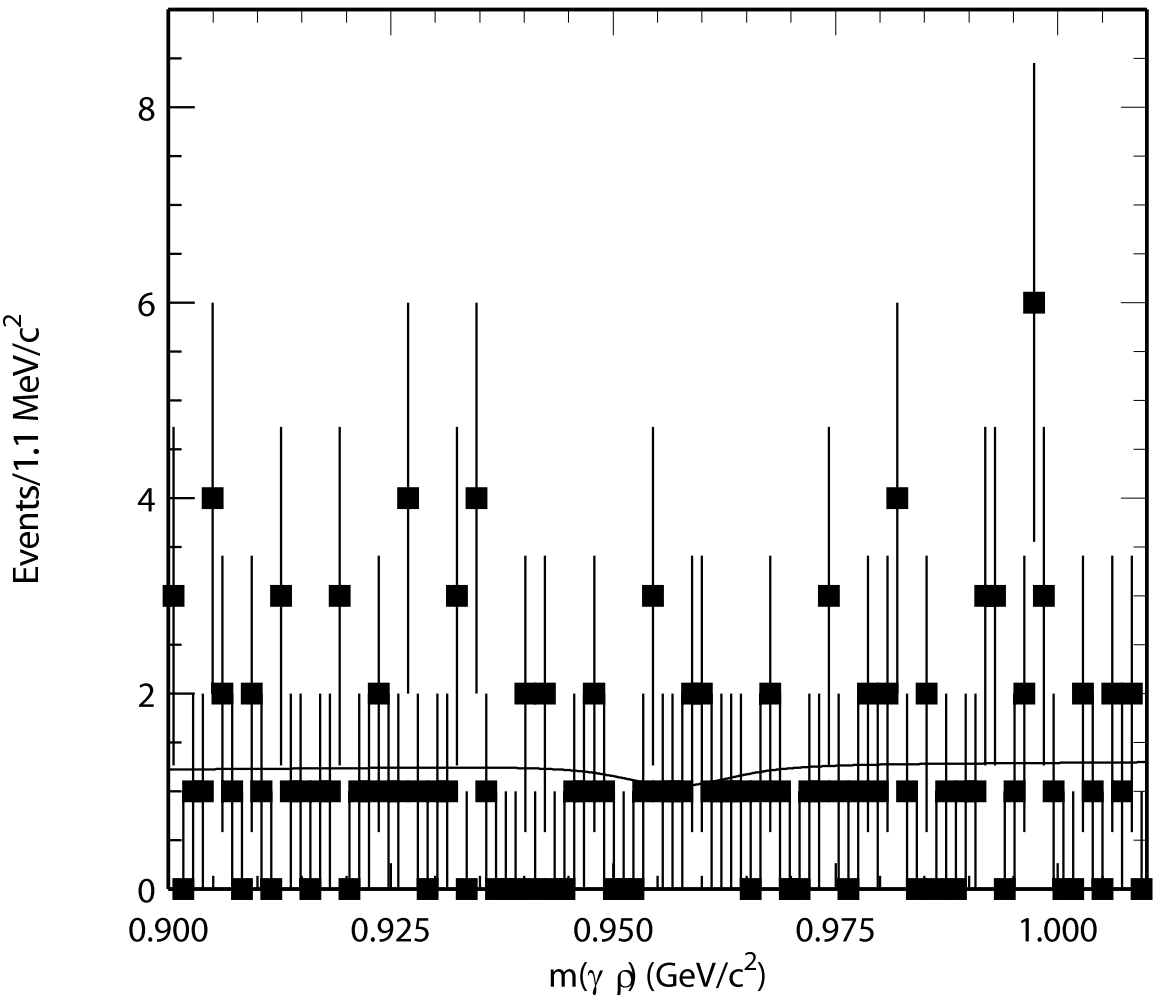

Figure 3–35. Without continuum subtraction, the fit to data plot for the mode $\Upsilon(1S) \to \gamma\eta'$; $\eta' \to \gamma\rho$: Leaving the area floating while keeping the mean, width and other parameters fixed to MC fit parameters, we obtain -3.1 ± 5.3 events.

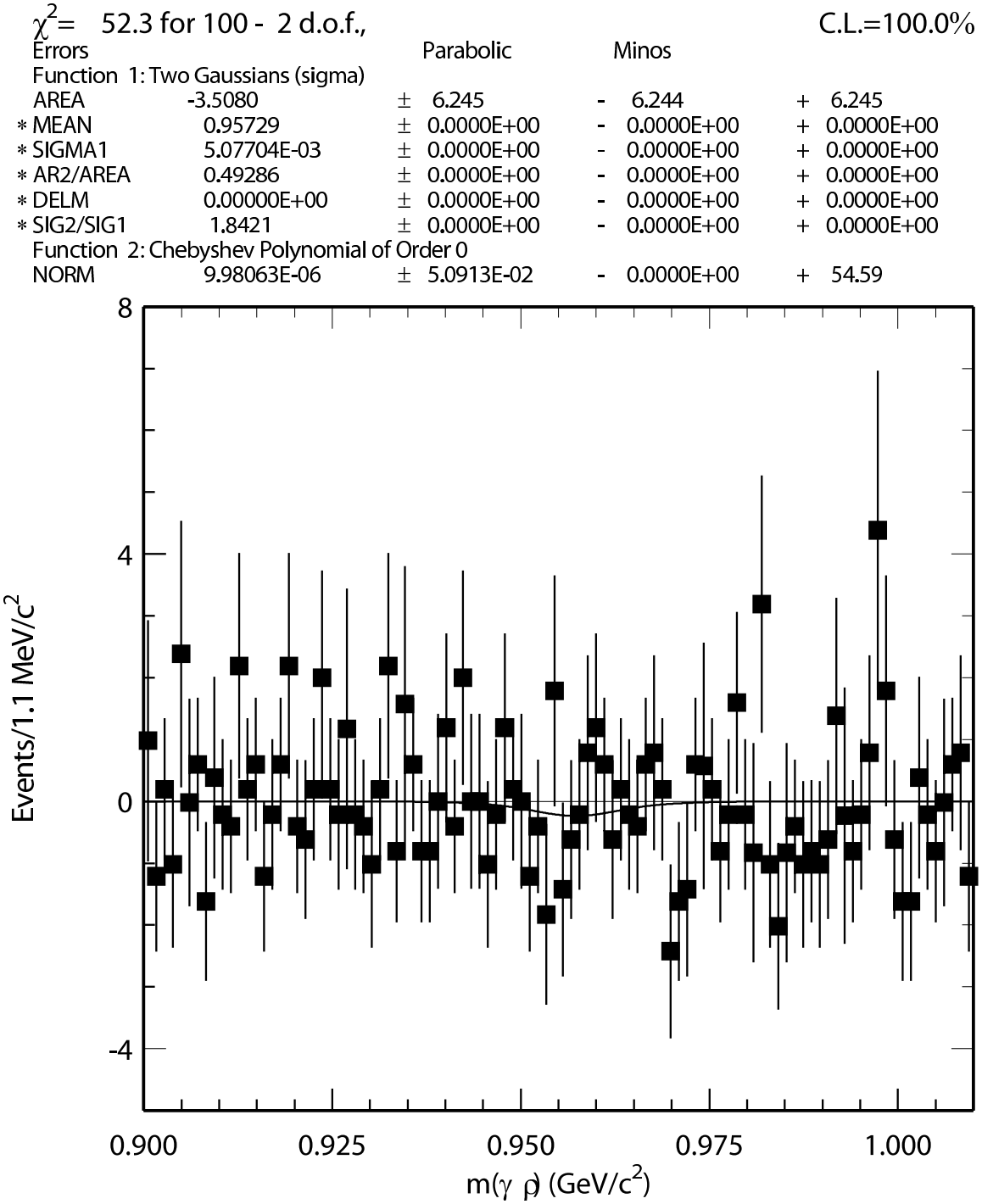

Figure 3–36. The fit to the continuum subtracted data plot for the mode $\Upsilon(1S) \to \gamma\eta'$; $\eta' \to \gamma\rho$: Leaving the area floating while keeping the mean, width and other parameters fixed to MC fit parameters, we obtain -3.5 ± 6.3 events. The underlying continuum has been subtracted using the distribution from 4S data.

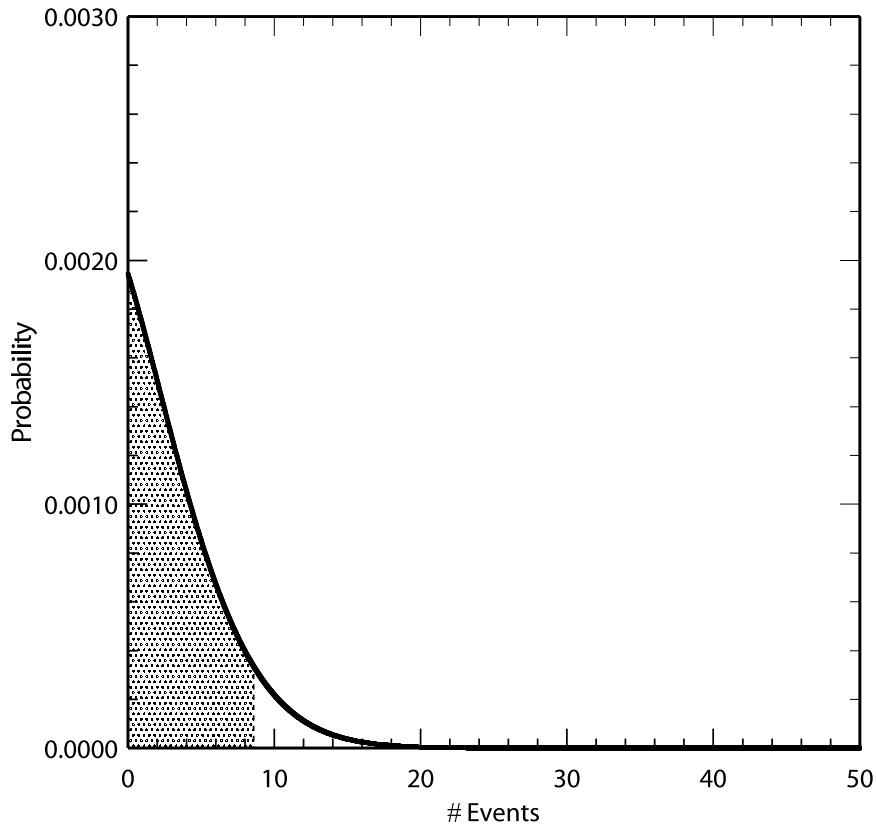

Figure 3–37. The normalized probability distribution for different signal area for the mode $\Upsilon(1S) \rightarrow \gamma\eta'$; $\eta' \rightarrow \gamma\rho$: The shaded area spans 90% of the probability.

Since we observe no clear signal, we calculated the upper limit yield at 90% C.L. on the lines described in Section 3.3.3.4. We obtain an upper limit of 8.59 events at 90% C.L. from the 1S data and a slightly lower number from continuum subtracted 1S distribution where 8.35 events is obtained. We do a χ^2 fit for continuum subtracted distribution rather than a likelihood fit. The upper limit plots are shown in Figures 3–38 and 3–39.

Likelihood = 122.1

χ^2= 116.0 for 100 - 2 d.o.f., C.L.= 10.3%

Errors		Parabolic	Minos	
Function 1: Two Gaussians (sigma)				
* AREA	8.5900	± 0.0000E+00	- 0.0000E+00	+ 0.0000E+00
* MEAN	0.95729	± 0.0000E+00	- 0.0000E+00	+ 0.0000E+00
* SIGMA1	5.07704E-03	± 0.0000E+00	- 0.0000E+00	+ 0.0000E+00
* AR2/AREA	0.49286	± 0.0000E+00	- 0.0000E+00	+ 0.0000E+00
* DELM	0.00000E+00	± 0.0000E+00	- 0.0000E+00	+ 0.0000E+00
* SIG2/SIG1	1.8421	± 0.0000E+00	- 0.0000E+00	+ 0.0000E+00
Function 2: Chebyshev Polynomial of Order 1				
NORM	1063.0	± 100.3	- 97.27	+ 103.4
CHEB01	1.95267E-02	± 0.1491	- 0.1491	+ 0.1482

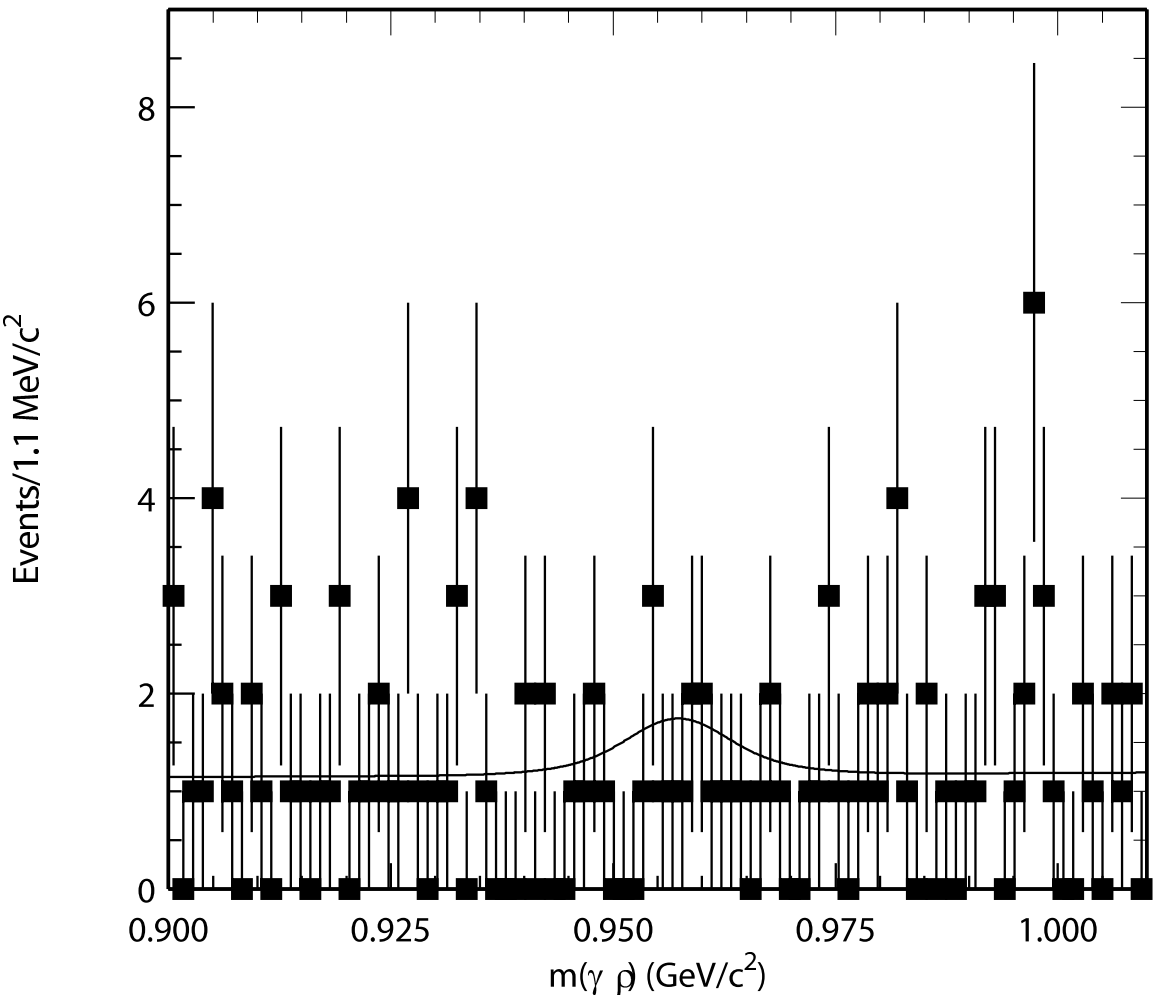

Figure 3–38. The 90% upper limit fit to the invariant mass distribution without continuum subtraction

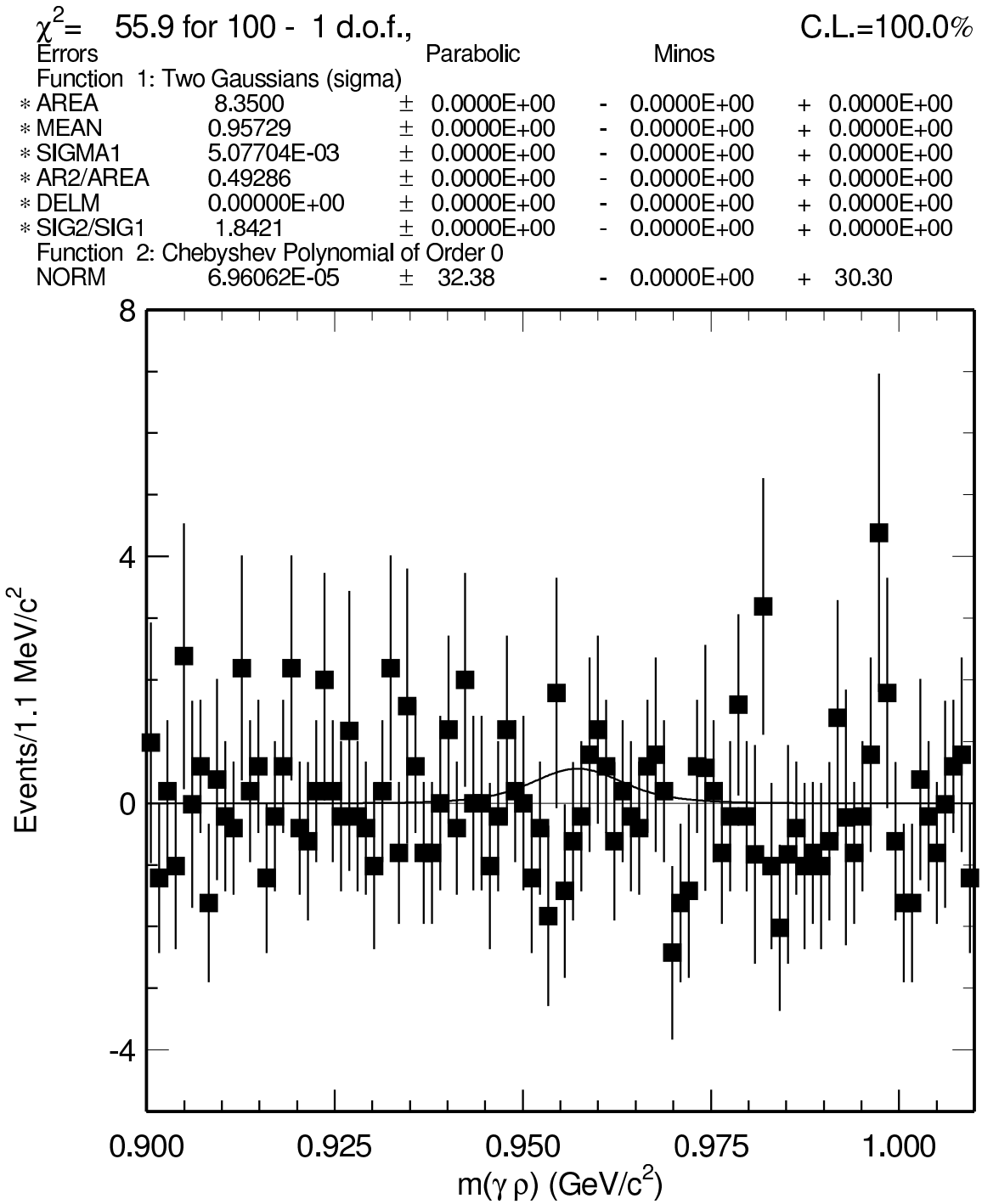

Figure 3–39. After subtracting the underlying continuum, the 90% upper limit fit to the invariant mass distribution

3.4 Summary

In this chapter, we discussed the reconstruction of seven different decay channels (three submodes of η and four submodes of η') for the radiative decays of $\Upsilon(1S)$ into η and η'. The reconstruction efficiency for each mode was obtained from signal Monte Carlo generated with the $(1+\cos^2\theta)$ angular distribution expected for decays $\Upsilon(1S) \to \gamma + \text{pseudoscalar}$. The selection criteria were deliberately minimal to ensure high efficiencies.

To increase our sensitivity, we mass-constrained the intermediate mesons (except for ρ meson in the mode $\eta' \to \gamma\rho$) to their nominal masses. We also used the event vertex information (if available) to improve the shower 3-momentum measurement, eventually improving the invariant mass resolution of the final η and η' by around 10%. We were also able to improve the candidate η' invariant mass resolution in the mode $\eta' \to \gamma\rho$ by performing the 4-momentum constraint to the $\Upsilon(1S)$ candidate in a special way.

The 3-photon final state resulting from $\Upsilon(1S) \to \gamma\eta; \eta \to \gamma\gamma$ was dominated by the QED background process $e^+e^- \to \gamma\gamma\gamma$, which we tried to reject by training a neural net program. The performance of neural net was slightly better than the alternative choice of optimizing the *asymmetry* cut and a large proportion of the background was lowered; however, some background events still remained. Similarly, in the mode $\Upsilon(1S) \to \gamma\eta'; \eta' \to \gamma\rho$, by tightening the E_s cut, most of the background was rejected. No clear signal was observed in either of the two background limited modes, and upper limits were measured (see Sections 3.3.3.4 and 3.3.7, page 94) at the 90% C.L.

For the modes which were found to be virtually background free, no signal candidate events were observed in our acceptance mass window, the exception being $\Upsilon(1S) \to \gamma\eta'; \eta \to \pi^+\pi^-\pi^0$ where two good signal candidates were observed. However, both the reconstruction efficiency and the branching ratio of $\eta' \to$ daughters is higher

for the mode $\Upsilon(1S) \to \gamma\eta'; \eta \to \gamma\gamma$, yet no signal event was observed in this mode challenge the claim of signal from the mode $\Upsilon(1S) \to \gamma\eta'; \eta \to \pi^+\pi^-\pi^0$.

Since there is no clear signal, we can only quote upper limits on the branching ratios. In the next chapter we evaluate the systematic uncertainties from our event selection criteria, combine the results from different submodes and quote individual as well as combined upper limits.

CHAPTER 4
SYSTEMATIC UNCERTAINTIES AND COMBINED UPPER LIMIT

4.1 Systematic Uncertainties

We note that we already know that our measurement will be a limit, and that the statistical uncertainties are going to dominate over the systematic uncertainties. Therefore, although we do our best to correctly evaluate the systematic uncertainties, it is not necessary to evaluate them with as great a precision as is necessary for measurements where they are a limiting factor.

4.1.1 Trigger Considerations

There are two trigger lines which are important for this analysis. The events in the modes involving charged tracks in them are primarily collected online by the firing of ELTRACK trigger line. Monte Carlo predicts that the in-efficiency of trigger cut (after all other selection criteria are met) in the η' modes $\eta'; \eta \to \pi^0\pi^0\pi^0$, $\eta'; \eta \to \pi^+\pi^-\pi^0$, and $\eta' \to \gamma\rho$ is 1.1%, 0.9%, and 2%, respectively. For the mode $\eta'; \eta \to \gamma\gamma$, MC predicts no loss in efficiency due to trigger cut. The highest in-efficiency due to trigger cut in the modes with charged tracks is found to be 2.8%, which is noted for the mode $\Upsilon(1S) \to \gamma\eta; \eta \to \pi^+\pi^-\pi^0$. Although these are predictions of the Monte Carlo, high efficiency of trigger is reassuring and implies a small uncertainty. It is also difficult to do data based checks for this trigger (in-)efficiency, however the small inefficiency implies a small systematic uncertainty. We assign 1% systematic uncertainty due to possible mismodeling of trigger in modes with charged tracks.

For the all neutral modes where η decays to $\gamma\gamma$ or $3\pi^0$, the important trigger lines are BARRELBHABHA or ENDCAPBHABHA, which fire when two high energy showers are registered back-to-back in CC. Although these lines are well understood for $e^+e^- \to \gamma\gamma$ events, the trigger efficiency for higher multiplicity showers, not

necessarily back-to-back and possessing energy lower than the beam energy is less well studied. From the luminosity ($954.2\,\mathrm{pb}^{-1}$) of our QED Monte Carlo sample $e^+e^- \to \gamma\gamma\gamma$ (which we used in our study of the decay mode $\Upsilon(1S) \to \gamma\eta; \eta \to \gamma\gamma$), we expect 485 events in our real data sample, which is raised to 2942 events if we relax the neural-net cut. In real data, we find 471 and 2869 events for cut configuration with and without the neural-net cut, respectively. Our yield falls short of the expectation by $\sim 3\%$, which again is reassuring that our efficiencies are rather understood. We therefore assign $\sqrt{2869}/2869 + (2942 - 2869)/2869 \sim 4.5\%$ systematic uncertainty due to trigger simulation in "all neutral" modes.

4.1.2 Standard Contributions

We use standard numbers for systematic uncertainty contributions from imperfect modeling of tracks and showers as advised by the CLEO Systematic Study of Systematics program (SSS) [24]. SSS is a group effort to determine the systematic uncertainties of the detector for use by collaborators in their analyses.

The uncertainty in the photon, π^0 and η reconstruction efficiency arises from possible deficiencies in the Monte Carlo simulation of photon and hadronic interactions in the calorimeter. Within the SSS, the systematic errors of the π^0 reconstruction were determined [25] to be less than 5%. We therefore assign a systematic uncertainty contribution from mismodeling of the calorimeter response as 2.5% for each shower, or 5% for $\pi^0 \to \gamma\gamma$, $\eta \to \gamma\gamma$ candidates. For $\eta \to \pi^0\pi^0\pi^0$, we assign a 15% systematic uncertainty due to calorimetry.

The track finding systematic efficiencies have been studied in detail [26] using tau-decays in the low multiplicity events and found the tracking systematic uncertainty as $(-0.17 \pm 0.20)\%$. A conservative value of 0.5% has been used in [27, 28] and 1.0% per track in [1, 29]. We prefer to use the conservative estimate of 1% in this analysis. Thus, we assign a systematic uncertainty of 2% for modes involving two charged tracks and 4% for the decay sequence $\eta' \to \eta\pi^+\pi^-, \eta \to \pi^+\pi^-\pi^0$.

4.1.3 Contributions from Event Selection Criteria

As discussed in Section 3.3.1, we study the efficiency of pion hypothesis $S_{dE/dx}$ for two tracks is combined in quadrature ($S^2_{dE/dx}$) in data using the ω peak from the process $e^+e^- \to \gamma\omega$ and find a 4% systematic difference in the efficiency. This cut is also used in the modes $\eta'; \eta \to \gamma\gamma$, $\eta'; \eta \to \pi^0\pi^0\pi^0$, and $\eta'; \eta \to \pi^+\pi^-\pi^0$, we therefore assign 4%, 4%, and 5.7% systematic uncertainties, respectively.

To evaluate the systematic uncertainties for the mode $\Upsilon(1S) \to \gamma\eta'$; $\eta' \to \gamma\rho$, we exploit the ρ peak present in data owing to the continuum process $e^+e^- \to \gamma\gamma\rho$. We measure the ρ signal in data over a floating background function with all cuts in place except the one under consideration and with all cuts in place. From these numbers, we calculate the effective efficiency of the cut. For MC, we report the individual cut efficiency relative to the events in η' invariant mass plot that survive all the cuts. The difference with MC and data efficiency values is taken as the systematic uncertainty which are added in quadrature.

Table 4–1. Systematics' table for $\Upsilon(1S) \to \gamma\eta'$; $\eta' \to \gamma\rho$

Cut	Data Eff (%)	MC Eff (%)	Sys. Err (%)
Particle Identification	97.35	99.08	1.75
Electron Veto	94.94	91.87	-3.35
Muon Rejection	97.93	98.99	1.07
Overall Sys Err			3.93

In the reconstruction of decay chaine $\Upsilon(1S) \to \gamma\eta; \eta \to \gamma\gamma$, we use only two cuts other than the 4-momentum consistency. One of the cuts, namely energy *asymmetry* of two showers from η decay is rather well understood and can be taken on its face value. The other cut is *netvalue* > 0.4, the output from the neural net and warrants an investigation for systematic uncertainty. The uncertainty, in this case, arises not because of the inability of MC to model the prescribed background process properly but with our own understanding of background itself.

In the absence of a signal, the task of finding the systematic uncertainty becomes difficult as the conventional approach of taking the difference between data and MC efficiencies, as we did in mode $\eta' \to \gamma\rho$, is not applicable. Instead, we test the neural net's efficiency on background, by comparing the efficiency of passing events in QED Monte Carlo, with the efficiency of passing events in data (which is dominated by QED events). To be conservative in our estimate of systematic uncertainty, we calculate the relative difference in efficiency for a wide range of possible choices for the cut (see Figure 4–1) and select the maximum relative difference and thus, the maximum possible uncertainty as per our approach. We obtain a systematic uncertainty of 7.0% for *netvalue* > -0.6 having an efficiency of 97% in signal MC and background rejection ratios as 24.7% and 23.0% in QED MC and real data, respectively. It may be recalled that the actual value of neural net cut used in event selection is *netvalue* > 0.4 with 51% efficiency in signal MC while rejecting 86% of the background from QED MC. We note that this does not prove that the neural net is incorrectly modeled in our real analysis, as it is likely that the QED Monte Carlo that we generated does not mimic all the types of event in the real data sample. Once again, our choices are erring on the side of conservative estimates of the systematic uncertainty.

We do not attribute any systematic uncertainty to find a 4.0 GeV hard photon. Just from the basic cuts listed in Tables 3–2 and 3–3, we find that efficiency of finding the hard-photon after all other basic cuts is $\sim 96\%$. Although we can not study the in-efficiency of 4.0 GeV cut by relaxing it further as this is our "skim-cut," we plot the energy of hard photon in six of the seven modes from respective MC samples after all our selection criteria has been met. We find that there is no cut off at 4.0 GeV, but just a small tail as shown in Figure 4–2, which confirms that the efficiency of this cut is close to maximal.

The final systematic uncertainties for decay modes of η and η' are tabulated in Tables 4–2 and 4–3, respectively. It is worthwhile to note that there is no systematic

uncertainty due to analysis cuts in the mode $\Upsilon(1S) \rightarrow \gamma\eta; \eta \rightarrow \pi^0\pi^0\pi^0$. The possible event selection uncertainty in this mode has already been taken care of in the calorimetery mismodeling. We also ignore any systematic uncertainty due to the highly efficient cuts on χ^2_η (applicable only in the η' modes) and $\chi^2_{\mathrm{P}4}$ in all the modes.

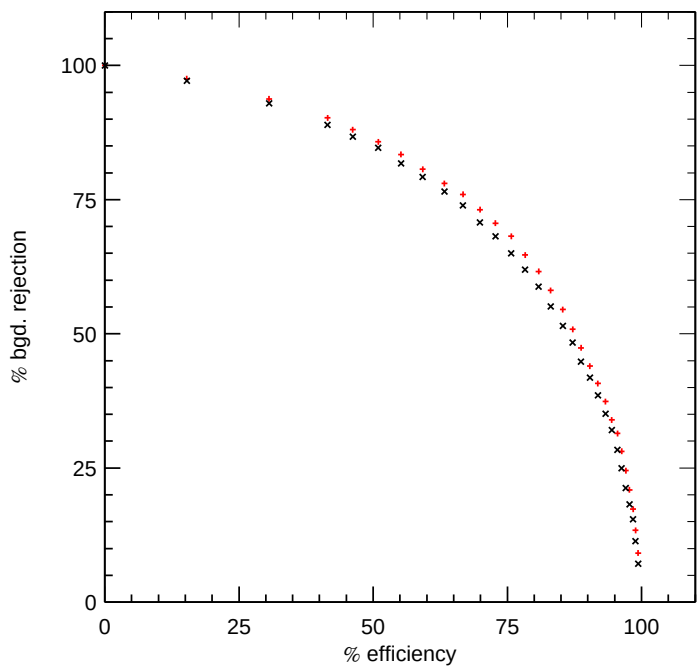

Figure 4–1. Amount of background rejected for various values of asymmetry and neural net cut having the same efficiency. The "efficiency" is obtained from signal Monte Carlo. "Background rejection" is obtained either from QED Monte Carlo sample (red pluses) or from real data (black crosses).

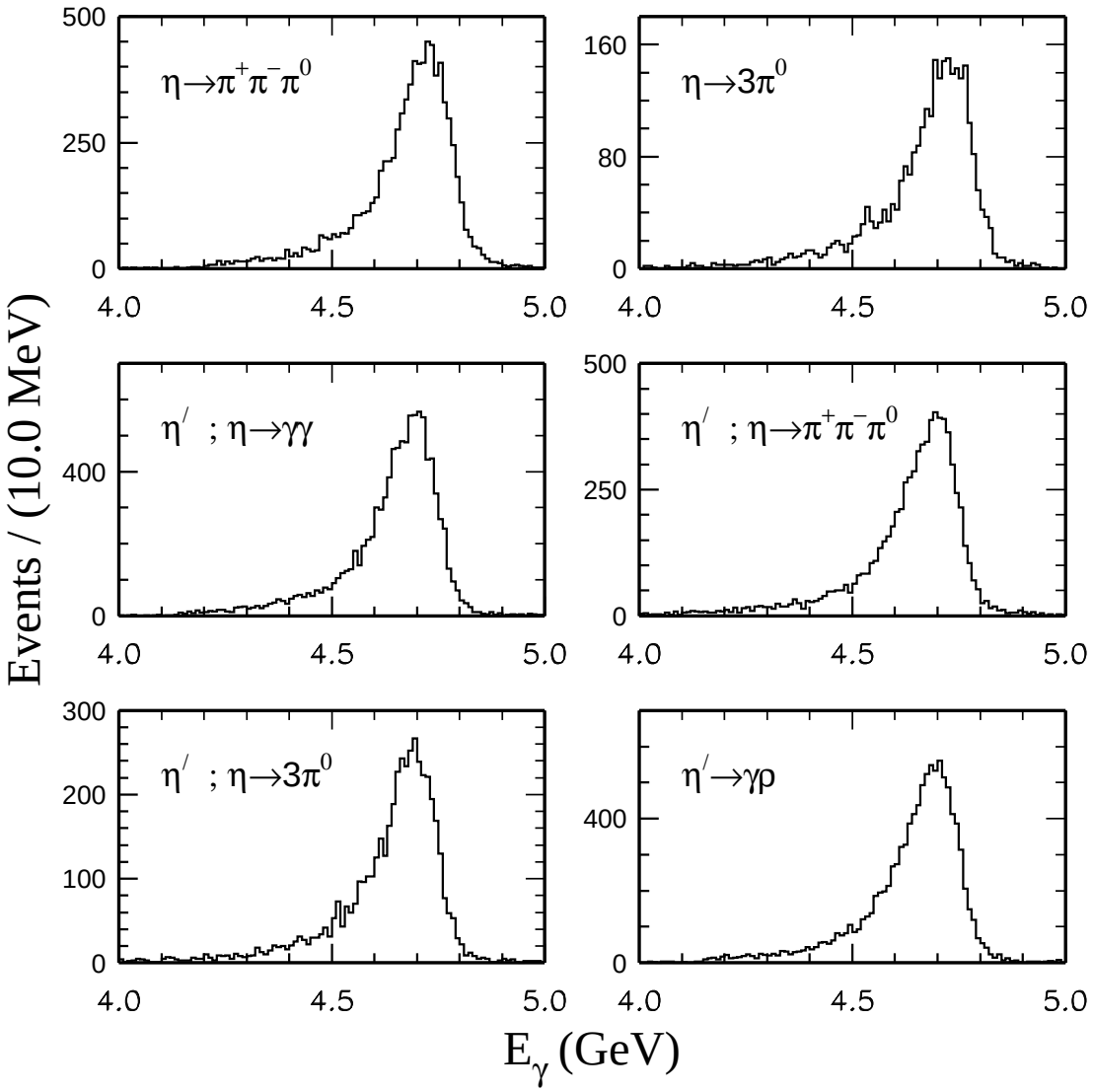

Figure 4–2. Energy of the hard photon in MC samples after all our selection criteria for respective modes

Table 4–2. Systematics uncertainties for various decay modes of η.

Source	$\eta \to \gamma\gamma$	$\eta \to \pi^+\pi^-\pi^0$	$\eta \to \pi^0\pi^0\pi^0$
Trigger Mismodeling	4.5%	1%	4.5%
Tracking	-	2%	-
Calorimetry	5%	5%	15%
Analysis Cuts	7%	4%	-
MC (Stat. Error)	1.3%	1.2%	1.7%
Overall	9.8%	6.9%	16.0%

Table 4–3. Systematics uncertainties for various decay modes of η'

Source	$\eta'; \eta \to \gamma\gamma$	$\eta'; \eta \to \pi^+\pi^-\pi^0$	$\eta'; \eta \to \pi^0\pi^0\pi^0$	$\eta' \to \gamma\rho$
Trigger Mismodeling	1%	1%	1%	1%
Tracking	2%	4%	2%	2%
Calorimetry	5%	5%	15%	2.5%
Analysis Cuts	4%	5.7%	4%	3.9%
MC (Stat. Error)	1.0%	1.6%	2.4%	1.0%
Overall	6.9%	8.8%	15.9%	5.2%

4.2 Combined Upper Limits

In order to get final limits for the two modes under investigation, we need to combine the results from the submodes. This is not easy, because in each case we have one submode with background, and roughly Gaussian statistics, and other submodes which have no data in the signal region and Poisson statistics are applicable. Furthermore, we wish to include the systematic uncertainties into the calculation to calculate our final limits.

We derive the combined probability distribution for the branching fraction as $\mathcal{L}_{\mathrm{P}} = \prod_i \mathcal{L}_{\mathrm{P},i}$ with $\mathcal{L}_{\mathrm{P},i}$ being the normalized likelihood functions of the ith submodes. All likelihood functions are in terms of the $\Upsilon(1\mathrm{S}) \to \gamma\mathrm{P}$ branching fraction $\mathcal{B}(\Upsilon(1\mathrm{S}) \to \gamma\mathrm{P}) = N_{\mathrm{P}}/(\epsilon_i \cdot \mathcal{B}_{\mathrm{P},i} \cdot N_{\Upsilon(1\mathrm{S})})$ where $\mathrm{P} = \eta, \eta'$, and ϵ_i and $\mathcal{B}_{\mathrm{P},i}$ denote the efficiency and branching fractions of ith mode, and N_{P} is the number of signal events randomly thrown. The likelihood functions for background limited modes $\Upsilon(1\mathrm{S}) \to \gamma\eta; \eta \to \gamma\gamma$ and $\Upsilon(1\mathrm{S}) \to \gamma\eta'$; $\eta' \to \gamma\rho$ and $\Upsilon(1\mathrm{S}) \to \gamma\eta; \eta \to \gamma\gamma$ are taken from Sections 3.3.3.4 and 3.3.7 (page 94), respectively. For modes with zero or few observed events, we generate Poisson-distributed branching ratios compatible with experimental outcome. The systematic uncertainties are incorporated [30] by smearing the likelihood functions by Gaussian distributions given by the errors on final mode branching fractions, efficiencies and $N_{\Upsilon(1\mathrm{S})}$. The constituent $\mathcal{L}_i$'s as well as the combined $\mathcal{L}$ are shown in Figures 4–3 – 4–6

The combined upper limit on the branching ratios $\Upsilon(1\mathrm{S}) \to \gamma\mathrm{P}$ is obtained by integrating the corresponding combined probability distribution $\mathcal{L}$ up to 90% area in the physically allowed region which are

$$\mathcal{B}(\Upsilon(1\mathrm{S}) \to \gamma\eta) < 9.3 \times 10^{-7}$$

$$\mathcal{B}(\Upsilon(1\mathrm{S}) \to \gamma\eta') < 1.77 \times 10^{-6}.$$

The upper limit due to individual modes, excluding and including the systematic errors are listed in Table 4–4. It is noteworthy that the combined limit for the $\Upsilon(1S) \to \gamma\eta'$ is larger than one of the constituent modes ($\Upsilon(1S) \to \gamma\eta'; \eta \to \gamma\gamma$). This happens as $\Upsilon(1S) \to \gamma\eta'; \eta \to \pi^+\pi^-\pi^0$ actually has a positive answer.

Table 4–4. Results of the search for $\Upsilon(1S) \to \gamma\eta'$ and $\Upsilon(1S) \to \gamma\eta$. Results include statistical and systematic uncertainties, as described in the text. The combined limit is obtained after including the systematic uncertainties.

	$\eta'; \eta \to \gamma\gamma$	$\eta'; \eta \to \pi^+\pi^-\pi^0$	$\eta'; \eta \to \pi^0\pi^0\pi^0$	$\eta' \to \gamma\rho$
Observed events	0	2	0	-3.1 ± 5.3
$\mathcal{B}_{\eta',i}\%$	17.5 ± 0.6	10.0 ± 0.4	14.4 ± 0.5	29.5 ± 1.0
Reconstruction efficiency (%)	40.6 ± 2.8	24.5 ± 2.2	16.6 ± 2.6	40.1 ± 2.1
$\mathcal{B}(\Upsilon(1S) \to \gamma\eta')$(90% C.L.) (excluding sys. uncertainties)	$< 1.53 \times 10^{-6}$	$< 10.25 \times 10^{-6}$	$< 4.54 \times 10^{-6}$	$< 3.42 \times 10^{-6}$
$\mathcal{B}(\Upsilon(1S) \to \gamma\eta')$(90% C.L.) (including sys. uncertainties)	$< 1.54 \times 10^{-6}$	$< 10.41 \times 10^{-6}$	$< 4.69 \times 10^{-6}$	$< 3.44 \times 10^{-6}$
Combined limit on $\mathcal{B}(\Upsilon(1S) \to \gamma\eta')$		$< 1.77 \times 10^{-6}$		

	$\eta \to \gamma\gamma$	$\eta \to \pi^+\pi^-\pi^0$	$\eta \to \pi^0\pi^0\pi^0$
Observed events	-2.3 ± 8.7	0	0
$\mathcal{B}_{\eta,i}\%$	39.4 ± 0.3	22.6 ± 0.4	32.5 ± 0.3
Reconstruction efficiency (%)	23.8 ± 2.4	32.8 ± 2.2	11.8 ± 1.9
$\mathcal{B}(\Upsilon(1S) \to \gamma\eta)$(90% C.L.) (excluding sys. uncertainties)	$< 7.27 \times 10^{-6}$	$< 1.47 \times 10^{-6}$	$< 2.83 \times 10^{-6}$
$\mathcal{B}(\Upsilon(1S) \to \gamma\eta)$(90% C.L.) (including sys. uncertainties)	$< 7.35 \times 10^{-6}$	$< 1.47 \times 10^{-6}$	$< 2.91 \times 10^{-6}$
Combined limit on $\mathcal{B}(\Upsilon(1S) \to \gamma\eta)$		$< 9.3 \times 10^{-7}$	

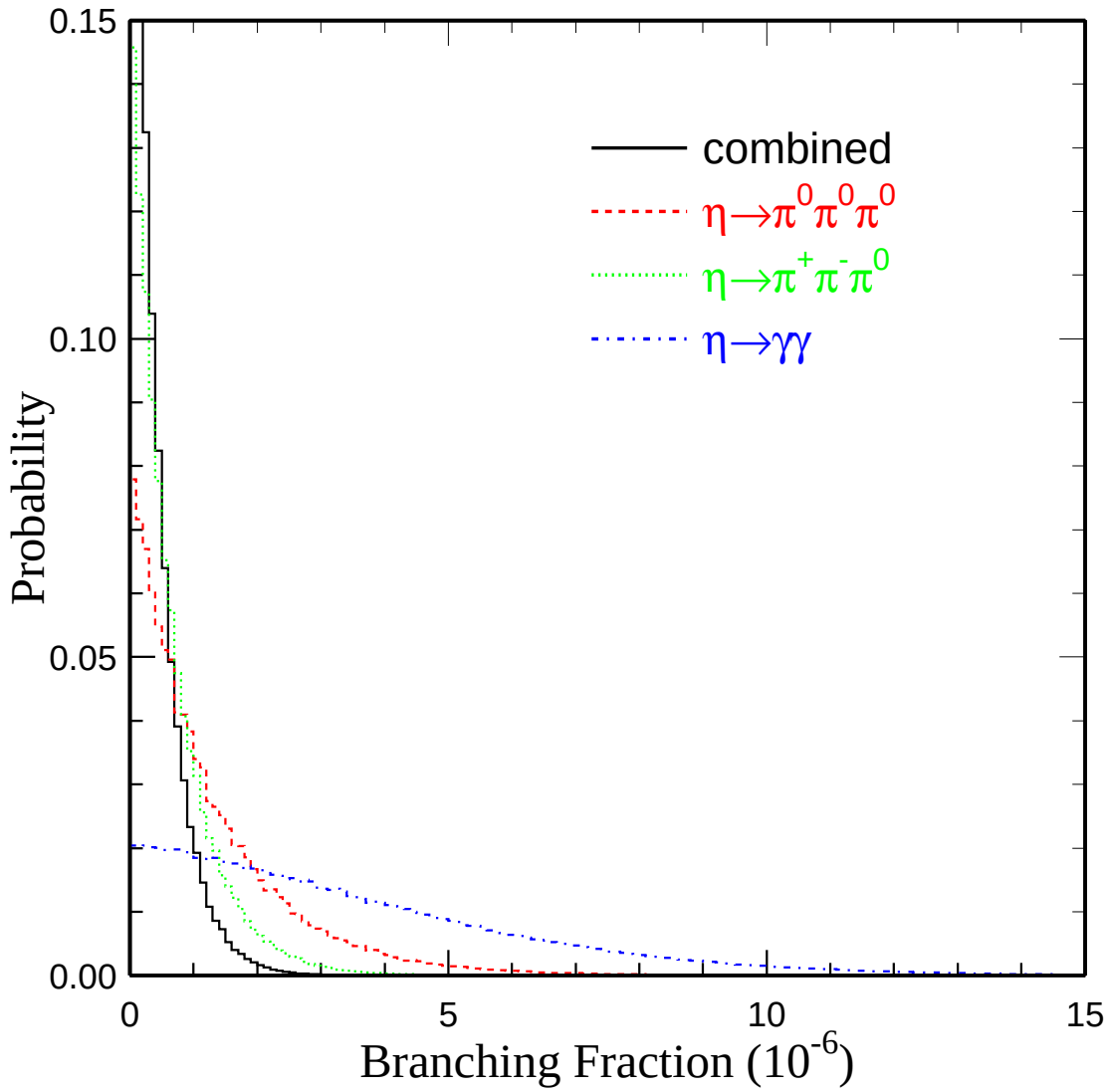

Figure 4–3. Probability distribution as function of branching ratio for the decay mode $\Upsilon(1S) \to \gamma\eta$: Black curve denotes the combined distribution. The distributions have been normalized to the same area.

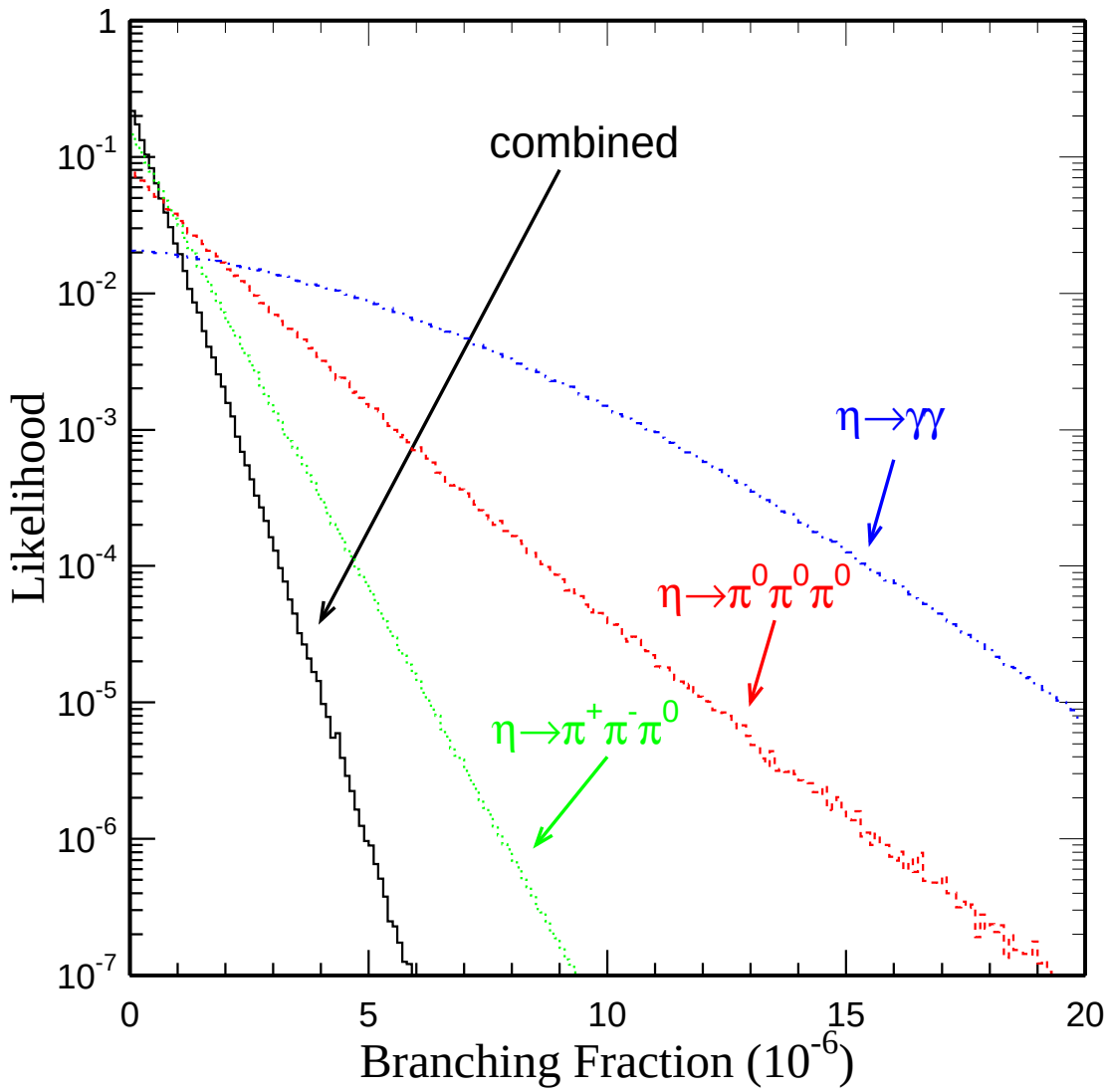

Figure 4–4. Plotted on log-scale, the likelihood distribution as function of branching ratio for the decay mode $\Upsilon(1S) \to \gamma\eta$: Black curve denotes the combined distribution. All distributions have been normalize to the same area.

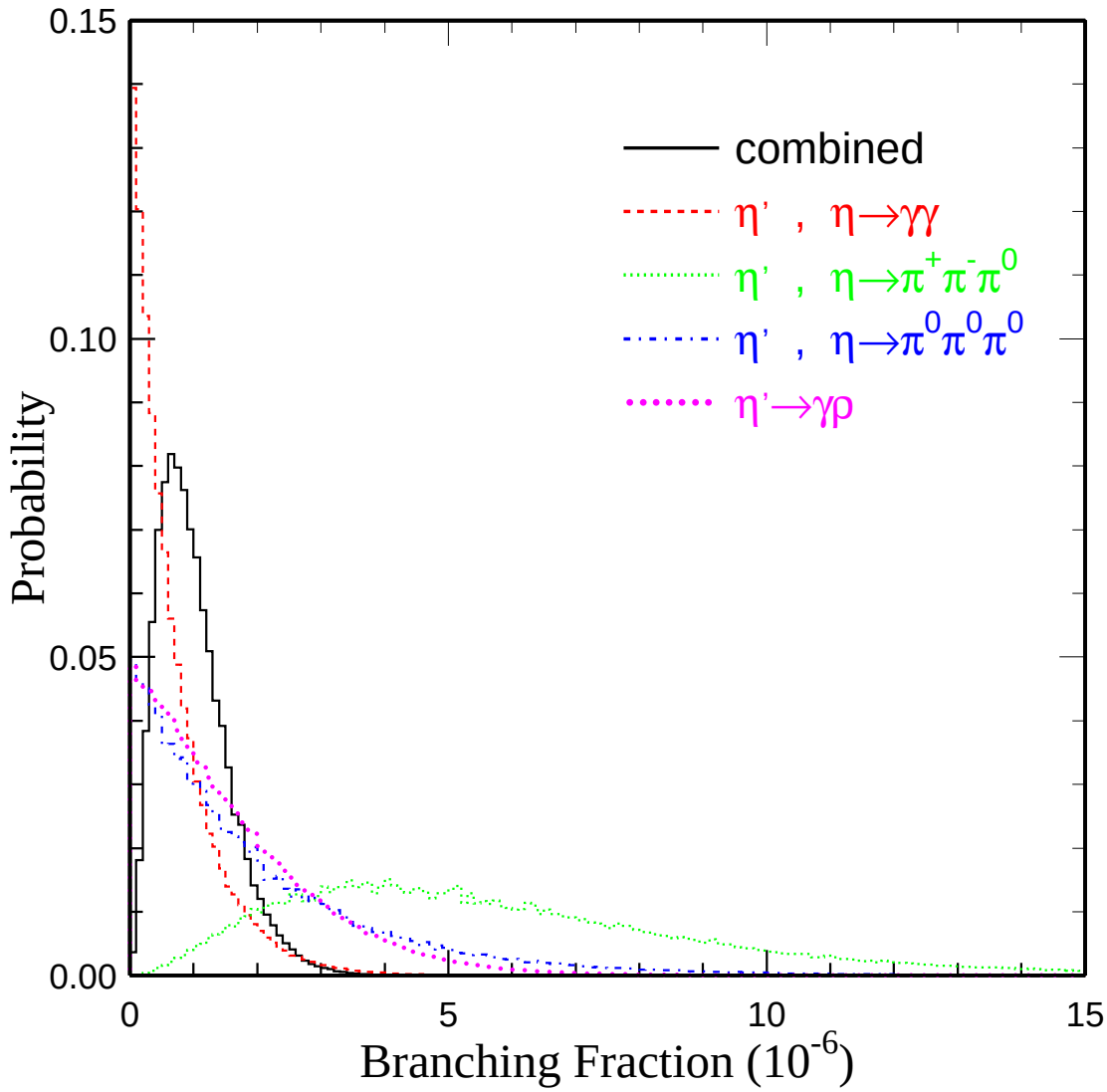

Figure 4–5. Probability distribution as function of branching ratio for the decay mode $\Upsilon(1S) \to \gamma\eta'$: Black curve denotes the combined distribution. All distributions have been normalize to the same area.

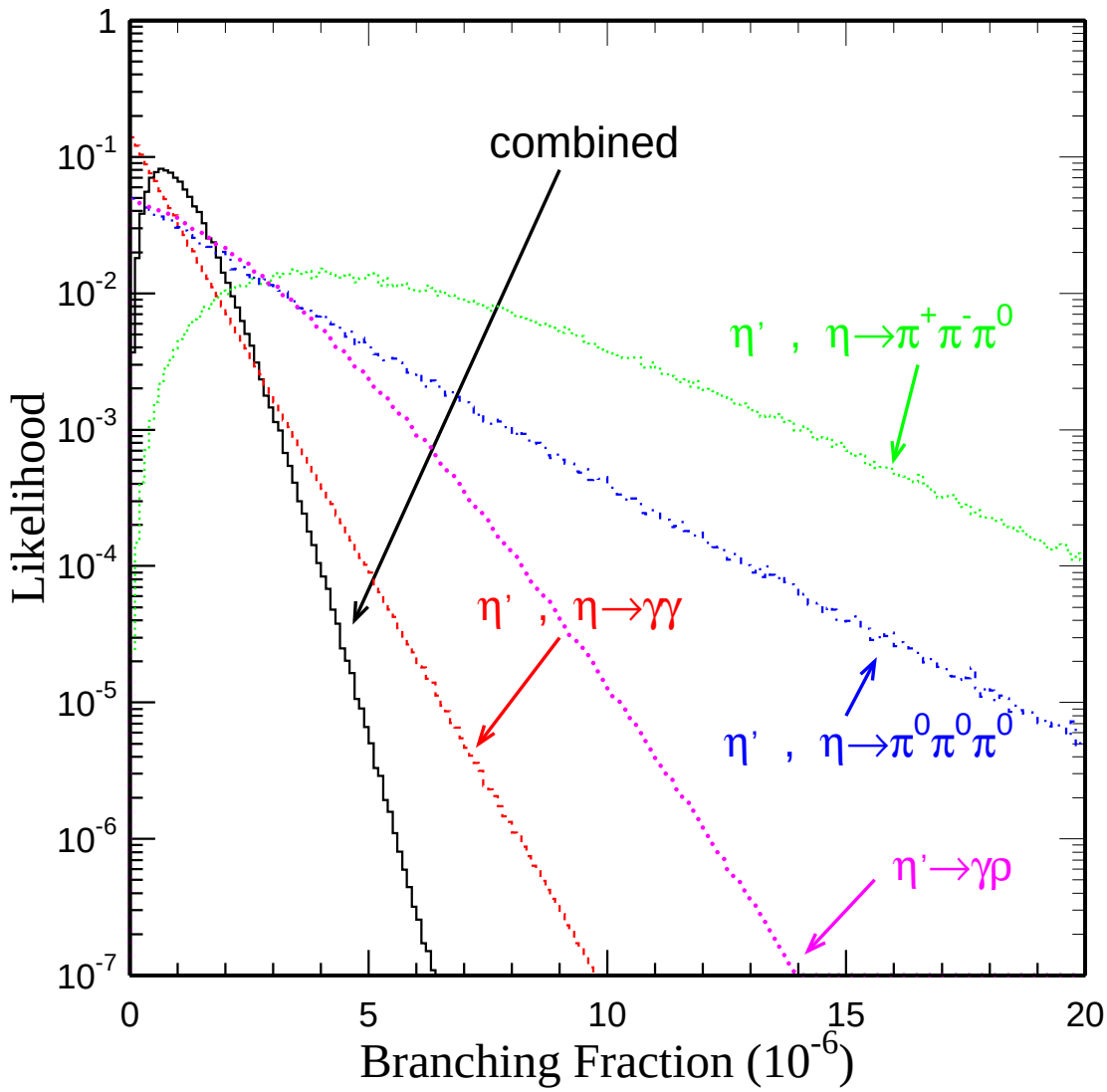

Figure 4–6. Plotted on log-scale, the likelihood distribution as function of branching ratio for the decay mode $\Upsilon(1S) \to \gamma\eta'$: Black curve denotes the combined distribution. All distributions have been normalized to the same area.

CHAPTER 5
SUMMARY AND CONCLUSIONS

We report on a new search for the radiative decay of $\Upsilon(1S)$ to the pseudoscalar mesons η and η' in $(21.2 \pm 0.2) \times 10^6$ $\Upsilon(1S)$ decays collected with the CLEO III detector. The η meson was searched for in the three modes $\eta \to \gamma\gamma$, $\eta \to \pi^+\pi^-\pi^0$ or $\eta \to \pi^0\pi^0\pi^0$. The η' meson was searched for in the mode $\eta' \to \gamma\rho$ or $\eta' \to \pi^+\pi^-\eta$ with η decaying through any of the above three modes. All these modes, except $\eta' \to \gamma\rho$ have been investigated in CLEO II data amounting to $N_{\Upsilon(1S)}= (1.45 \pm 0.03) \times 10^6$ $\Upsilon(1S)$ mesons and resulted in upper limits which were reported as $\mathcal{B}(\Upsilon(1S) \to \gamma\eta')$ $< 1.6\times10^{-5}$ and $\mathcal{B}(\Upsilon(1S) \to \gamma\eta) < 2.1\times10^{-5}$ at the 90% confidence level. These limits were already significantly smaller than naive predictions, and also the model of Körner and colleagues[10], whose perturbative QCD approach predictions for $\mathcal{B}(J/\psi \to \gamma X)$ where $X = \eta, \eta', f_2$ as well as $\mathcal{B}(\Upsilon(1S) \to \gamma f_2)$ agree with experimental results.

With CLEO III data sample 14.6 times as large as the original CLEO II data sample we find no significant signal in any of the modes. Based purely upon the luminosities, we would expect the new upper limits to be scaled down by a factor of between 14.6 (in background-free modes) and $\sqrt{14.6}$ in background dominated modes. In the search for $\Upsilon(1S) \to \gamma\eta$ we find no hint of a signal, and manage to reduce the limit by an even larger factor than this. In the search for $\Upsilon(1S) \to \gamma\eta'$, however, we find two clean candidate events in the channel $\Upsilon(1S) \to \gamma\eta'; \eta \to \pi^+\pi^-\pi^0$, which, though we cannot claim them as signal, do indicate the possibility that we are close to the sensitivity necessary to obtain a positive result. Because of these two events, our combined limit for $\Upsilon(1S) \to \gamma\eta'$ is not reduced by as large a factor as the luminosity ratio, and in fact is looser than that obtained using one submode ($\Upsilon(1S) \to \gamma\eta'; \eta \to \gamma\gamma$) alone. In this analysis we found upper limits which we report at 90% confidence

level as

$$\mathcal{B}(\Upsilon(1\mathrm{S}) \to \gamma\eta) < 9.3 \times 10^{-7},$$

$$\mathcal{B}(\Upsilon(1\mathrm{S}) \to \gamma\eta') < 1.77 \times 10^{-6}.$$

Our results are sensitive enough to test the appropriateness of pseudoscalar mixing technique as pursued by Chao [11] where mixing angles among various pseudoscalars including η_b are calculated. Then using the predicted allowed M1 transition $\Upsilon \to \gamma\eta_b$ he predicts $\mathcal{B}(\Upsilon(1\mathrm{S}) \to \gamma\eta) = 1 \times 10^{-6}$ and $\mathcal{B}(\Upsilon(1\mathrm{S}) \to \gamma\eta') = 6 \times 10^{-5}$. Our limits are significantly smaller than Chao's predictions and do not favor his approach.

The sensitivity challenge posed by both extended vector dominance model and twist approach of Ma are beyond our reach. In extended VDM, Intemann predicts $1.3 \times 10^{-7} < \mathcal{B}(\Upsilon(1\mathrm{S}) \to \gamma\eta) < 6.3 \times 10^{-7}$ and $5.3 \times 10^{-7} < \mathcal{B}(\Upsilon(1\mathrm{S}) \to \gamma\eta') < 2.5 \times 10^{-6}$ where the two limits determined by having destructive or constructive interference, respectively, between the terms involving $\Upsilon(1\mathrm{S})$ and $\Upsilon(2\mathrm{S})$. Even if it is determined that the amplitudes are added constructively, our limit stays higher than the VDM prediction for $\Upsilon(1\mathrm{S}) \to \gamma\eta$.

In a more realistic approach, Ma has calculated the leading contribution to branching ratio using the twist expansion [13]. Ma's prediction of $\mathcal{B}(\Upsilon(1\mathrm{S}) \to \gamma\eta') \approx 1.7 \times 10^{-6}$ is consistent with our result. However, his prediction for $\mathcal{B}(\Upsilon(1\mathrm{S}) \to \gamma\eta) \approx 3.3 \times 10^{-7}$ is a factor ~ 3 smaller than our limit.

To conclude, our upper limits at 90% C.L. suggest that pseudoscalar mixing approach as pursued by Chao does not explain the exceedingly small rate for radiative decays of $\Upsilon(1\mathrm{S})$ into pseudoscalar η and η'. The approach adopted by Ma is encouraging and it is desirable to include the relativistic corrections and other effects in QCD to explain our experimental results.

APPENDIX
EVENT VERTEX AND RE-FITTING OF $\pi^0 \to \gamma\gamma$

The standard $\pi^0 \to \gamma\gamma$ and $\eta \to \gamma\gamma$ candidates as extracted from the frame are reconstructed by assuming that showers originate from the origin of CLEO coordinate system. In the absence of event vertex information, this is the best course. To improve our $\pi^0 \to \gamma\gamma$ and $\eta \to \gamma\gamma$ 4-momentum resolution, we mass constrain the $\gamma\gamma$ pair to the nominal mass while assuming that the showers originate from the event vertex.

Although CLEO III software provides us with event vertex information by means of the package `EventVertexProd`, an algorithm based upon kinematic fitting [31], and thus giving us the best possible measurement of the event vertex, we believe that the procedure is a bit too slow and our analysis does not require a very precise information of x and y coordinates of the event vertex. It is rather the z coordinate of event vertex which is most critical as far photon momentum is concerned. So, we measure the event vertex using a relatively faster alternative, a brief sketch of which follows.

The event vertex (x_v,y_v,z_v) calculation is based upon CLEO II routine `V3FIND` where the event vertex is calculated separately in x,y and in z. The z_v coordinate is taken as the weighted average of z0 of individual tracks with weights being the inverse of r.m.s. error on z0. For x,y part , all pairs of tracks are formed and the weighted average of these pairs is taken as (x_v,y_v) . In our implementation, we first form a list of quality tracks, and start with beam spot as the *guess vertex* . We swim the tracks to the *guess vertex* and calculate the (x_v,y_v,z_v) , which is taken as the new *guess vertex* and the process is iterated until converges. At each iteration, we calculate the r.m.s error on z_v and keep only the tracks which have z within one standard deviation of z_v. The mathematical expressions for z_v and standard deviation σ_z are in terms of

the individual values z_k and corresponding weights w_k are:

$$z_v = \overline{z} = \sum w_k z_k / \sum w_k \tag{A-1}$$

$$\sigma_z^2 = (\sum w_k (z_k - \overline{z})) \times n_{eff}/(n_{eff} - 1) \tag{A-2}$$

where n_{eff} is given by

$$n_{eff} = (\sum w_k)^2 / \sum w_k^2. \tag{A-3}$$

The (x_v,y_v) part is calculated by first finding the intersection points x,y for all track pairs. Then we take the weighted average of these points to find (x_v,y_v). The equations to this end are:

$$dm = sin(\phi_1)cos(\phi_2) - cos(\phi_1)sin(\phi_2) \tag{A-4}$$

$$ds = \sqrt{\sigma_{d_{0,1}}^2 \sigma_{d_{0,2}}^2} \tag{A-5}$$

$$w_k = dm^4/ds \tag{A-6}$$

$$x_k = (d_{0,1}cos(\phi_1) - d_{0,2}cos(\phi_2))/dm \tag{A-7}$$

$$y_k = (d_{0,1}sin(\phi_1) - d_{0,2}sin(\phi_2))/dm \tag{A-8}$$

If the tracks intersect, we calculate (x_v,y_v) as:

$$x_v = \overline{x} = \sum w_k x_k / \sum w_k \tag{A-9}$$

$$y_v = \overline{y} = \sum w_k y_k / \sum w_k \tag{A-10}$$

$$\sigma_x^2 = \sigma_y^2 = (n_{trk} - 1)/\sum w_k \tag{A-11}$$

If the tracks do not intersect however, we proceed as follows:

$$w_k^x = sin^2(\phi_k)/\sigma_{d_{0,k}}^2 \tag{A-12}$$

$$w_k^y = cos^2(\phi_k)/\sigma_{d_{0,k}}^2 \tag{A-13}$$

$$d_k^b = d_k^0 + sin(\phi_k)x_{beamspot} - cos(\phi_k)y_{beamspot} \tag{A-14}$$

$$x_v = \overline{x} = x_{beamspot} - \sum (d_k^b sin(\phi_k) w_k^x) / \sum w_k^x \tag{A-15}$$

$$y_v = \overline{y} = y_{beamspot} - \sum (d_k^b sin(\phi_k) w_k^y) / \sum w_k^y \tag{A-16}$$

$$\sigma_x^2 = 9.0 / \sum w_k^x \tag{A-17}$$

$$\sigma_y^2 = 9.0 / \sum w_k^y \tag{A-18}$$

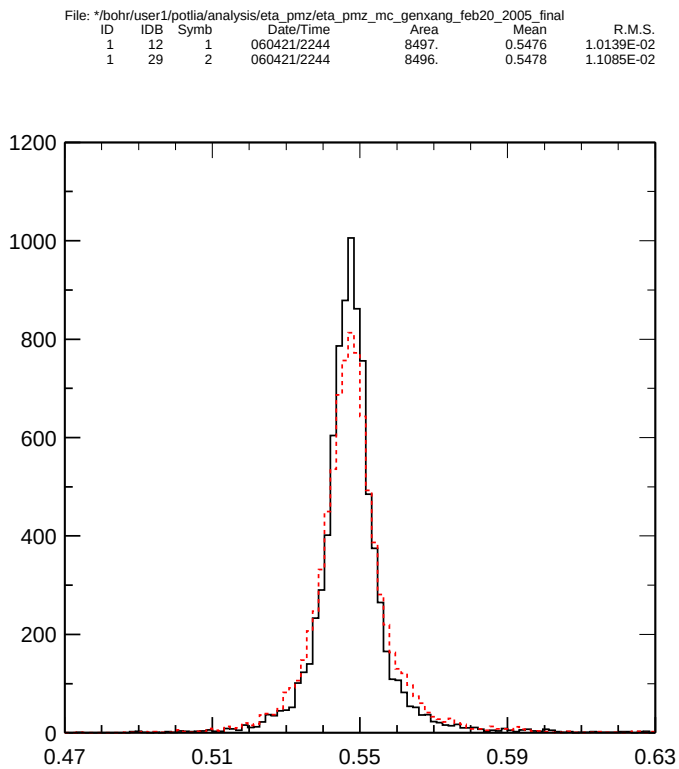

Figure 1. Reconstructed invariant mass distribution of $\pi^+\pi^-\pi^0$ candidate from signal Monte Carlo for the mode $\Upsilon(1S) \to \gamma\eta; \eta \to \pi^+\pi^-\pi^0$: After all cuts in place, solid black histogram represents the $\eta \to \pi^+\pi^-\pi^0$ candidate invariant mass distribution when π^0 candidate is re-fit from the event vertex. Overlay in dotted, red histogram is obtained using default π^0 candidates.

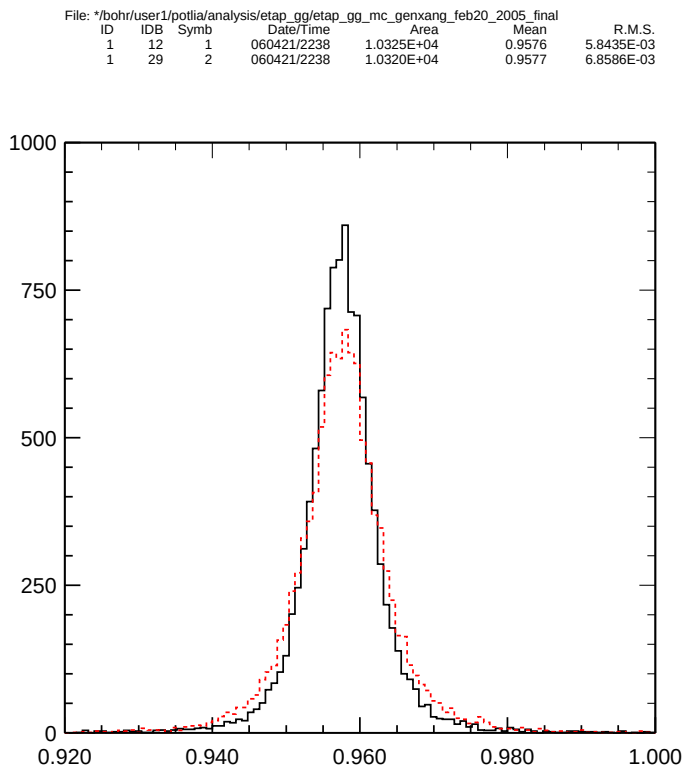

Figure 2. Reconstructed invariant mass distribution of $\eta\pi^+\pi^-$ candidate from signal Monte Carlo from signal Monte Carlo for the mode $\Upsilon(1S) \to \gamma\eta'; \eta \to \gamma\gamma$: After all cuts in place, solid, black histogram represents the $\eta'; \eta \to \gamma\gamma$ candidate invariant mass distribution when $\eta \to \gamma\gamma$ candidate is re-fit from the event vertex. Overlay in dotted, red histogram is obtained using default $\eta \to \gamma\gamma$ candidates.

REFERENCES

[1] S. B. Athar, P. Avery, L. Breva-Newell, R. Patel, V. Potlia, H. Stoeck *et al.* (CLEO Collaboration), Phys. Rev. D **73**, 032001 (2006); L. Breva-Newell, Ph.D. dissertation, University of Florida, (hep-ex/0412075).

[2] D. Griffiths, *Introduction to Elementary Particles* (John Wiley & Sons, New York, 1987).

[3] D. H. Perkins, *Introduction to High Energy Physics* (Addison-Wesley, Menlo Park, 1987).

[4] F. Halzen and A. D. Martin, *Quarks and Leptons: An Introductory Course in Modern Particle Physics* (John Wiley & Sons, New York, 1984).

[5] J. F. Donoghue, E. Golowich, B. R. Holstein, and T. Ericson, *Dynamics of the Standard Model* (Cambridge University Press, Cambridge, 1994).

[6] M. E. Peskin and D. V. Schroeder, *An Introduction to Quantum Field Theory* (Perseus Books, Reading, 1995).

[7] S. J. Richichi, H. Severini, P. Skubic, S. A. Dytman, V. Savinov, S. Chen *et al.* (CLEO Collaboration), Phys. Rev. Lett. **87**, 141801 (2001).

[8] A. Anastassov, J. E. Duboscq, K. K. Gan, T. Hart, K. Honscheid, H. Kagan *et al.* (CLEO Collaboration), Phys. Rev. Lett. **82**, 286 (1999).

[9] G. Masek, H. P. Paar, R. Mahapatra, R. A. Briere, G. P. Chen, T. Ferguson *et al.* (CLEO Collaboration), Phys. Rev. D **65**, 072002 (2002).

[10] J. G. Körner, J. H. Kühn, M. Krammer, and H. Schneider, Nucl. Phys. **B229**, 115 (1983).

[11] K. T. Chao, Nucl. Phys. **B335**, 101 (1990).

[12] G. W. Intemann, Phys. Rev. D **27** 2755 (1983).

[13] J. P. Ma, Phys. Rev. D **65** 097506 (2002).

[14] S. Eidelman, K. G. Hayes, K. A. Olive, M. Aguilar-Benitez, C. Amsler, D. Asner *et al.* (Particle Data Group Collaboration), Phys. Lett. B **592**, 1 (2004).

[15] T. Coan, Nucl. Instrum. Methods Phys. Res., Sect. A **453**, 49 (2000).

[16] Y. Kubota, J. K. Nelson, D. Perticone, R. Poling, S. Schrenk, M. S. Alam *et al.*, Nucl. Instrum. Methods Phys. Res., Sect. A **320**, 66 (1992).

[17] G. Viehhauser, Nucl. Instrum. Methods Phys. Res., Sect. A **462**, 146 (2001); D. Peterson, K. Berkelman, R. Briere, G. Chen, D. Cronin-Hennessy, S. Csorna *et al.*, Nucl. Instrum. Methods Phys. Res., Sect. A **478**, 142 (2002); A. Warburton, K. Arndt, C. Bebek, J. Cherwinka, D. Cinabro, J. Fast *et al.*, Nucl. Instrum. Methods Phys. Res., Sect. A **488**, 451 (2002); M. Artuso, R. Ayad, K. Bukin, A. Efimov, C. Boulahouache, E. Dambasuren *et al.*, Nucl. Instrum. Methods Phys. Res., Sect. A **502**, 91 (2003).

[18] I. Shipsey, J. Alexander, K. Arndt, A. Bean, C. Bebek, R. Boyd *et al.*, Nucl. Instrum. Methods Phys. Res., Sect. A **386**, 37 (1997).

[19] M. A. Selen, R. M. Hans, and M. J. Haney, IEEE Trans. Nucl. Sci. **48**, 562 (2001).

[20] R. A. Briere, G. P. Chen, T. Ferguson, G. Tatishvili, H. Vogel, M. E. Watkins *et al.* (CLEO Collaboration), Phys. Rev. D **70** 072001 (2004).

[21] QQ–The CLEO Event Generator, http://www.lns.cornell.edu/public/CLEO/soft/QQ (unpublished).

[22] F. Berends and R. Kleiss, Nucl. Phys. **B228**, 537 (1983).

[23] H. T. Nguyen, N. R. Prasad, C. L. Walker, and E. A. Walker, *A First Course in Fuzzy and Neural Control* (Chapman & Hall/CRC, 2003).

[24] CLEO Systemaric Study of Systematics program, https://www.lns.cornell.edu/restricted/CLEO/analysis/ac_help/systematics.html (unpublished).

[25] S. A. Dytman, J. A. Mueller, S. Nam, V. Savinov, G. S. Huang, D. H. Miller *et al.* (CLEO Collaboration), hep-ex/0307035.

[26] F. Liu and Y. Gao, CLEO internal note CBX **02-13** (2002) (unpublished).

[27] F. Liu, R. Stroynowski, and Y. Gao, CLEO internal note CBX **03-2** (2003) (unpublished).

[28] J. E. Duboscq, CLEO internal note CBX **05-30** (2005) (unpublished).

[29] T. K. Pedlar, CLEO internal note CBX **03-26** (2003) (unpublished).

[30] R. D. Cousins and V. L. Highland, Nucl. Instrum. Methods Phys. Res., Sect. A **320**, 331 (1992).

[31] P. Avery, CLEO internal note CBX **98-37** (1998) (unpublished).

BIOGRAPHICAL SKETCH

Vijay Singh Potlia was born in a small village in the western part of the northern state Haryana in India. After graduating from high school, he attended Kurukshtra University for 3 years, earning a Bachelor of Science (B.Sc.) degree. Later on he joined Jawaharlal Nehru University, New Delhi, India, and obtained his Master of Science (M.Sc.) degree. He was accepted to attend graduate school at the University of Florida in 1999.